Writing your PhD thesis in LaTeX2e

Using the CUED template

Krishna Kumar

Department of Engineering

University of Cambridge

This dissertation is submitted for the degree of

Doctor of Philosophy

King's College January 2017

I would like to dedicate this thesis to my loving parents …

Declaration

I hereby declare that except where specific reference is made to the work of others, the contents of this dissertation are original and have not been submitted in whole or in part for consideration for any other degree or qualification in this, or any other university. This dissertation is my own work and contains nothing which is the outcome of work done in collaboration with others, except as specified in the text and Acknowledgements. This dissertation contains fewer than 65,000 words including appendices, bibliography, footnotes, tables and equations and has fewer than 150 figures.

Krishna Kumar
January 2017

Acknowledgements

And I would like to acknowledge ...

Abstract

This is where you write your abstract ...

Table of contents

List of figures

List of tables

Nomenclature

Roman Symbols

tick Unit of time equal to 500 ns

Acronyms / Abbreviations

CRC Cosmic Ray Counter

FD Far Detector

MIP Minimally Ionising Particle

MPV Most Probable Value

PID Particle IDentification

PoCA Point of Closest Approach

ROI Region Of Interest

ADC Analogue to Digital Converter

SiPM Silicon Photo Multiplier

TPC Time Projection Chamber

Chapter 1

Introduction

1.1 XXXXX

1.2 XXXXXX

Chapter 2

Theory

2.1 Theory of neutrino physics

2.2 Nucleon decay in Grand Unifying Theories

2.3 Exisiting and future experiments

2.4 How Liquid Argone Time Projection Chambers work

Chapter 3

The Deep Underground Neutrino Experiment

3.1 DUNE location and beam line

3.2 The DUNE detectors and schedule

3.3 Physics opportunities of DUNE

3.3.1 Neutrino physics

3.3.2 Nucleon decay and supernovae neutrinos

Table 3.1 Nucleon decay limits in DUNE and Super-Kamiokande, in some favoured decay channels.

Total flux (cm^{-2} s^{-1})	Mean E_μ (GeV)	Mean slant depth (m w.e)	Mean θ (°)
5.66×10^{-9}	283	4532	26

Fig. 3.1 A schematic showing what the wrapped wire planes of the DUNE detector designs looked like in the 35 ton.

3.3.3 Background to nucleon decay

3.4 Path to building DUNE - The 35 ton prototype

3.5 The DUNE software

The software package used by DUNE is called LArSoft [1] [2] which is a simulation, reconstruction and analysis package for Liquid Argon Time Projection Chamber (LArTPC) that is being used by many experiments in the US neutrino program. LArSoft has been developed to be detector agnostic, meaning that much of the code is shared between experiments. To this end it is envisioned that it will be used as a platform for constant development in existing experiments and those still in the planning phases such as DUNE. LArSoft is built around the Fermilab-supported *analysis reconstruction framework* (*art*). External packages such as ROOT [3] and GEANT4 [4] are incorporated into LArSoft meaning that the user does not have to coordinate specific versions of the packages as the newest versions are automatically incorporated.

There are numerous mechanisms by which particles can be generated within the software with external packages. One such package is GENIE [5] which is used to study neutrino interactions and nucleon decays. Another package, Nuance [6], is a neutrino interaction generator specifically for Liquid Argon (LAr). Finally, CRY [7] and CORSIKA!!!citepCORSIKA are cosmic ray events generators which are used to simulate the expected event rates for surface detector locations in absence of a neutrino beam. Recently the MUon Simulations UNderground (MUSUN) [8] [9] generator which takes the output of MUon SImulation Code (MUSIC) [8] [10] [11] has also been incorporated, see Section 7.2 for further details. It is also possible to use an inbuilt single particle generation mode which is fully tunable as particle type, momenta, positions and directions can all be varied.

The co-ordinates and angles in LArSoft are defined as follows, and schematic representations of how this appears in the 35 ton are shown in Figure 3.3:

- x - The beam direction, with maximal x being where the beam enters the detector.

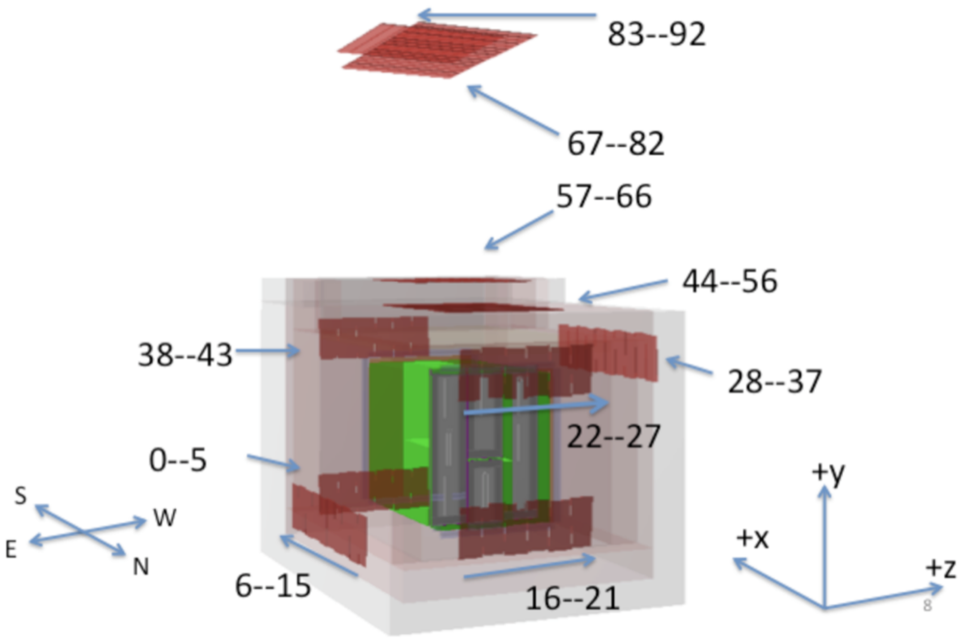

Fig. 3.2 A representation of the counter locations in the 35 ton, with the magnetic and LArSoft co-ordinate systems shown. The other detector components can be seen inside the cryostat, such that the counters on the North wall are behind the short drift volume. The East - West counters are numbered 6-15 and 28-37 respectively. The North Lower - South Upper counters are numbered 16-21 and 38 - 43 respectively. The North Upper - South Lower counters are numbered 22-27 and 0-5 respectively. The telescope triggers are numbered 44-92 and are split into four groups.

  - In the 35 ton prototype where there is no beam positive x is in the opposite direction to that which electrons drift in the large TPC, where $x = 0$ is the position of the APA frames in the long drift volume.
  - In the far detector geometry $x = 0$ is defined as the midpoint between the two rows of CPAs

- y - The vertical direction, with maximal y being the most highest point.
  - In the 35 ton $y = 0$ is halfway between the gap created by the two centre APAs which are mounted one above the other.
  - In the far detector $y = 0$ is defined as the midpoint between the two vertical layers of TPCs.

- z - Defined as such to have a right handed co-ordinate system.

  - In the 35 ton $z = 0$ is at the edge of the leftmost APA frame when looking down the long drift volume.
  - In the far detector $z = 0$ is defined at the edge of the leftmost APA frame when looking down the long drift volume.

- θ - The angle that a vector makes from the x axis in the xy plane.
- ϕ - The angle between the z axis and the vector.

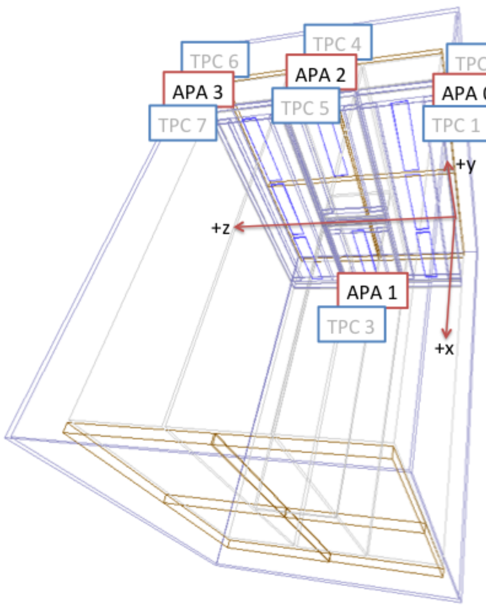

(a) The location of the origin of the 35 ton co-ordinate system in 3D.

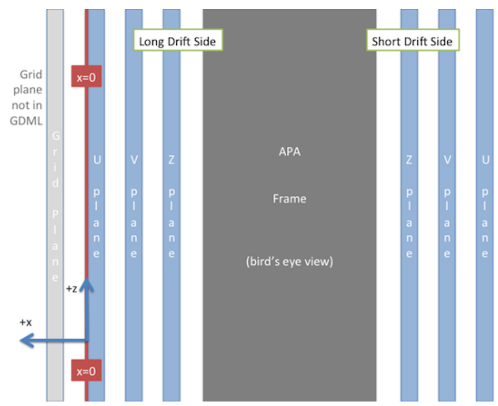

(b) The location of the origin of the 35 ton co-ordinate system in a 2D aerial view.

Fig. 3.3 The LArSoft co-ordinate system as it is represented in the 35 ton. Left shows the location of the origin relative to the TPC detector components. The four APAs, and eight TPCs are shown, where the even numbered TPCs are on the short drift side, ∼20 cm drift, and the odd numbered TPCs are on the long drift side, ∼250 cm drift. The CPAs are also shown as the objects with a brown outline. Right shows the location of the origin with respect to the APAs. The wire planes are shown, the U and V planes are induction wires, whilst the Z planes are collection wires.

The simulation of particles is usually split into five separate distinct processes to reflect the different stages in which development often progresses. The advantage of segmenting the computational process in this way is that improvements can easily applied to a file without rerunning the entire chain. This is especially important when large Monte Carlo or data samples are produced for general use within collaborations so that users are able to concentrate on improving a specific part of the computational process. When these all-purpose samples are produced the analysis performed provides users with any Monte Carlo truth information along with the reconstructed quantities for use in analyses performed outside LArSoft. The computational process is often broken down in the following way:

- Particle generator.
- Particle transport using GEANT4.
- Full detector simulation, including detector responses.
- Full event reconstruction.
- Analysis.

Later significant focus will be given to the reconstruction of TPC data, and so it is necessary to briefly illustrate the mechanisms by which TPC data is reconstructed in LArSoft. Much of the information presented below is summarised in [12] [2]. After the full detector simulation or data taking, detector effects such as the electronics response function and a pedestal offset have to removed. Once these effects are removed the signal is estimated using the optimal value of $signal/noise$ which would produce the measured signal. This process, called deconvolution, does not conserve pulse height and is not guaranteed to preserve the normalisation. The deconvoluted signals are all unipolar distributions which means that Gaussian distributions can then be fitted to them when trying to reconstruct hits. This is shown in Figure 3.4, and explained further below.

The deconvoluted signals are reconstructed into hits by identifying regions that are above a threshold value and then attempting to replicate the signal in these regions by introducing Gaussian distributions. For isolated hits this is typically achieved using only one Gaussian distribution, however for large energy depositions over a large period time where many particles are involved, multiple Gaussian distributions are often required. Large energy depositions are also possible when the direction of the particle aligns with a wire, this means that all of the deposited energy is collected on this single wire. Examples of reconstructed hits are shown in Figure 3.4. These figures are taken from separate CRY simulated events, and so do not correspond to a continuous simulated event. They have been selected only as a demonstration of the process of hit reconstruction. Figures 3.4a and 3.4b show multiple time-separated energy depositions on a collection and induction wire respectively. A more complex energy deposition on a collection plane wire is shown in Figure 3.4c where energy depositions from many particles at similar times have created a complicated energy deposition that requires many reconstructed hits to explain.

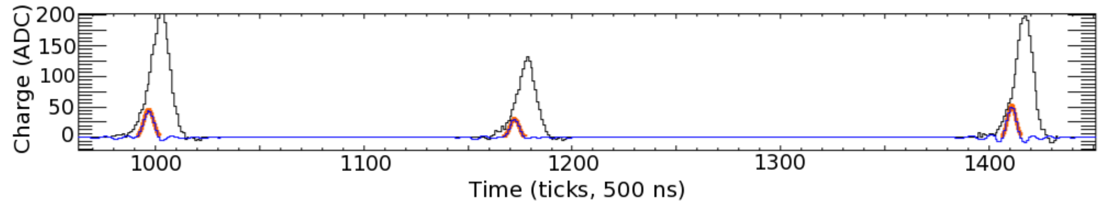

(a) Collection plane depositions.

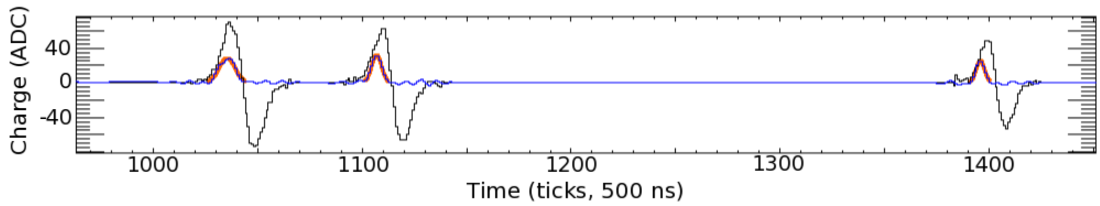

(b) Induction plane depositions.

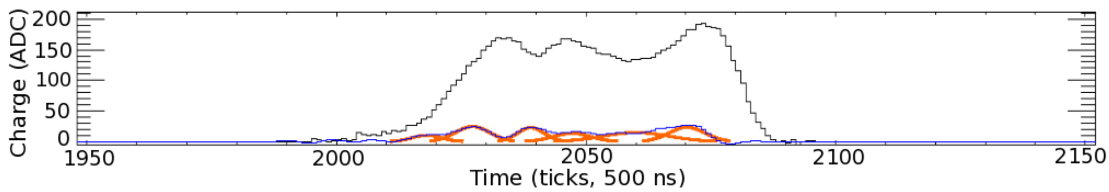

(c) A large collection plane deposition over a large period of time.

Fig. 3.4 The raw and deconvoluted signals with reconstructed hits on single wires for simulated energy depositions. The depositions, from particles generated by CRY, are not from a single event and have been selected for demonstration purposes only. The plots are shown with increasing charge (ADC) on the y axis, and increasing time (ticks, 500 ns) on the x axis. The black lines represent the raw signals, the blue lines represent the deconvoluted signals and the orange lines represent the reconstructed hits. Top shows depositions on a collection plane wire, it can be seen that the raw signal is unipolar. Middle shows depositions on an induction plane wire, it can be seen that the raw signal is bi-polar whilst the deconvoluted signal and reconstructed hits are unipolar. Bottom shows a complex deposition on a collection plane wire, where multiple reconstructed hits are required to reproduce the deconvoluted signal.

As noted in Section 3.2 and Section 3.4 the DUNE FD and the 35 ton both have wrapped wires on the induction planes. A result of this is that the location of the reconstructed hit on an induction wire is ambiguous as a single wire has many wire segments, as shown in Figure 3.1. An important feature of this ambiguity is that the TPC in which the hit occurred cannot be identified unless it is combined with another hit. These ambiguities do not extend to the collection plane wires as they are not wrapped and so consist of only a single wire segment in a single TPC. Hits are combined across the three planes by identifying wire segments on each plane which intersect and have hits at common times. In the traditional reconstruction process only hits that make these so-called ’triple points’ are considered disambiguated, with other hits being identified as noise hits causing them to be discarded.

The inclination of the wire planes has to be carefully chosen so as to minimise both the number of wires required and the number of times that wire triplets intersect. This is shown in Figure 3.5, where the wire inclinations used in the 35 ton detector, are compared to those in the DUNE FD reference design. The inclination of wires in the 35 ton was 45° ± 0.7° meaning that many wire triplets cross twice and some wire pairs cross three times. When wire triplets cross multiple times the triplet which has the smallest distance between the common intersection point and the two, two-wire intersection points, is chosen as the best intersection candidate. This is shown as the 'Good intersection' on the right panel in Figure 3.5. The different wire pitches are necessary so that one of the triple points can be evaluated to be a better candidate, as with a wire pitch of 45° it can be impossible to distinguish between different triple points. The inclination of wires in the FD was chosen to be 36° to remove the possibility of multiple intersection points, as given the geometry of the APAs multiple intersection points are impossible and so disambiguation is much simpler. The lower inclination results in more induction wires being required though, making it more expensive to instrument the detector. It is also important that all wires on a given APA are either read at the top or base of the APA, depending on whether the APA is at either the top or the base of the detector respectively. This is because there must be minimal space between TPCs in the DUNE FD to reduce the internal dead space, and so TPCs cannot be read out along the sides as this would require a non-negligible amount of space to accomodate the cabling.

Once the hits have been disambiguated they are combined to make clusters in each of the three planes, before the clusters are merged to make reconstructed tracks or showers. The clustering process is usually performed in wire-tick space on each plane separately, where all the hits from a single track or shower should be make a single cluster on each plane. It is possible to seed the start of clusters by using imaging techniques such as a Harris transform [13], or to identify straight lines by using Hough transforms [14]. As hits from a physical entity are unlikely to remain on a single channel or all come at identical times, clusters are often spread out over many channels for a range of times especially when performing clustering for showers.

Once clusters have been identified in each plane they can then be merged into 3-dimensional tracks and showers. The two most common tracking algorithms are PMTrack [15] and Pandora [16], and the most common showering algorithm is EMShower [17].

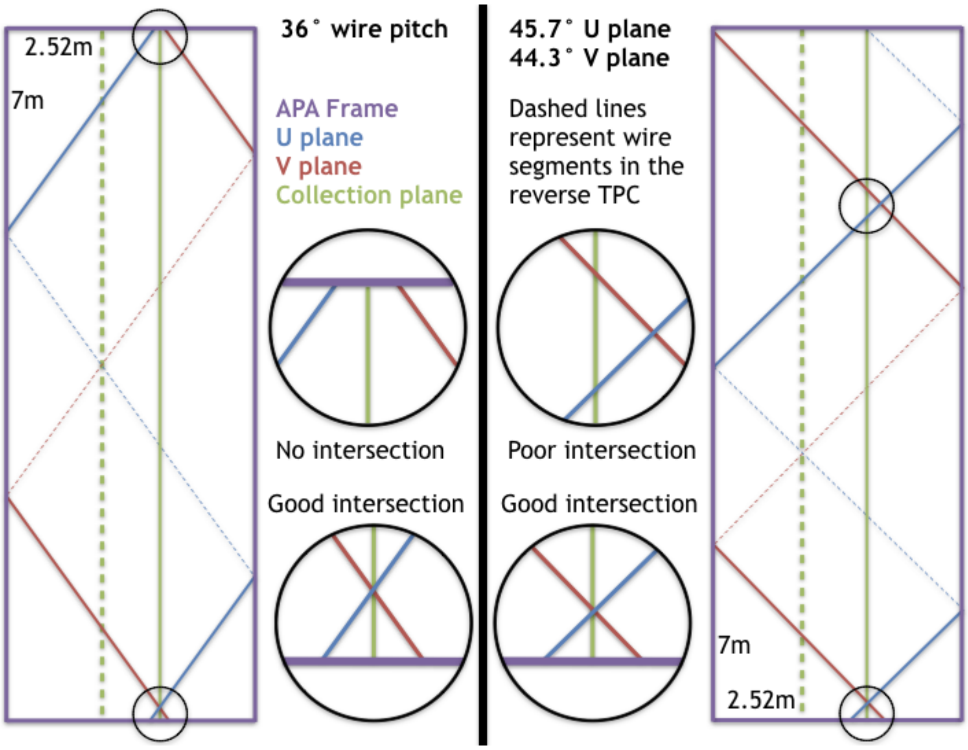

Fig. 3.5 The effect that different wire pitches have on the ability to perform disambiguation in APAs with the far detector geometry. The left panel shows a wire pitch of 36°, which is the reference design for the far detector, whilst the right panel shows wire pitches of 45° ± 0.7°, as was used in the 35 ton. The left panel shows that only one 'triple point' can be made with the three wires shown, and so disambiguation is relatively trivial. The right panel shows that two 'triple points' can be made with the three wires shown, the 'triple point' where the three wires have a common intersection point is labelled as a 'good intersection' and it is this intersection point which would be chosen for the disambiguated hit.

Once 3D objects have been reconstructed, the calorimetric quantities need to be determined, this is often done separately for each plane. Two models exist for calculating $\frac{dE}{dx}$ in LArSoft, Birks model [18] and a modified Box model [19] which uses a correction to the Box model [20] at low values of $\frac{dE}{dx}$. Normally the modified Box model is used as it holds for both large and small ionisation's, whereas Birks model experiences difficulties at large ionisation's and the traditional Box model struggles at low $\frac{dE}{dx}$. Both models incorporated in LArSoft, calculate the $\frac{dE}{dx}$ of a hit using the deposited charge (dQ) and the track pitch (dx) of the hit as well as the conversion of ADC value to number of electrons ($C_{GeV \to e^-}$), a correction due to electron lifetime ($C_{lifetime}$), the LAr density (ρ), the electric field (E_{field}) and the tunable electron recombination factors ($Recomb_X$). The series of equations used in Birks model are shown in Equation 3.1, whilst those used in the modified Box model are shown in

Equation 3.2.

$$\frac{dE}{dx} = \frac{dQdx}{\alpha - (\beta \times dQdx)} \tag{3.1a}$$

$$dQdx = \frac{dQ \times C_{lifetime}}{dx \times C_{ADC \to e^-}} \tag{3.1b}$$

$$\alpha = Recomb_A \times C_{GeV \to e^-} \times 10^{-3} \tag{3.1c}$$

$$\beta = \frac{Recomb_B}{\rho \times E_{field}} \tag{3.1d}$$

$$\frac{dE}{dx} = \frac{e^{\alpha} - Recomb_A}{\beta} \tag{3.2a}$$

$$\alpha = \frac{10^3 \times \beta}{C_{GeV \to e^-}} \times \frac{dQ}{dx} \tag{3.2b}$$

$$dQdx = \frac{dQ \times C_{lifetime}}{dx \times C_{ADC \to e^-}} \tag{3.2c}$$

$$\beta = \frac{Recomb_B}{\rho \times E_{field}} \tag{3.2d}$$

When performing calorimetry it is also important that the interaction time is known so that the x positions of hits can be corrected, as they will be reconstructed assuming an interaction time of 0 s. This assumption is made because when using beam events the beam trigger is placed at a time of $T = 0$. An unknown interaction time causes the hit and track positions to be calculated incorrectly, and will also skew the calorimetric corrections, as recombination is a drift dependant effect.

Chapter 4

The 35 ton camera system

4.1 The need for cameras in a Liquid Argon Time Projection Chamber

4.2 Design of the camera system

4.3 Tabletop tests

4.4 Safety reviews and installation

4.5 Performance in the 35 ton

Chapter 5

Simulations of the 35 ton prototype

5.1 Determination of interaction times

As outlined at the end of Section 3.5 it is important to know the interaction time of a track when performing calorimetric reconstruction. When performing simulations the simplest interaction time to assign to a reconstructed object is the Monte Carlo truth time of when the particle was created. The generation time can be used, as the time taken to travel the distances considered in simulations, less than 100 ns, is small when compared to the resolution of the detector (500 ns). When matching a reconstructed object with a GEANT4 particle the particle which contributed the most overall deposited charge to the whole track is chosen. This means that the energy deposited for each hit on the track is broken down into how much each particle contributed to the charge of the individual hit, with the energies summed over all hits. The ability to assign the true interaction times to 3D objects is vital when wanting to benchmark how well other algorithms to estimate interaction times perform or to determine the efficiency of the tracking algorithms as described in Section 5.3.

In the 35 ton detector, it was envisioned that there would be at least two ways in which interaction times could be assigned to tracks, one using the external cosmic ray counters and another using reconstructed scintillation light collected by the photon detectors. The cosmic ray counters were used extensively in the 35 ton data, as described in Section 6.4. However, in simulations the scintillation light was used as this would have been more powerful during continuous running. This is because, not all particles would pass through the counters but, one wold expect almost all of them to produce reconstructable scintillation light. The flashes of light are reconstructed using a pre-built library which models the expected number of photoelectrons to be measured on each photon detector given the 3D position of the source of the flash. Using the library it is then possible to reconstruct the location of a flash in three dimsenions, given the relative amounts of light that each photon detector collects. For example, less scintillation light will be collected for a flash that originated further away from the photon detectors. This library also takes into account the expected quantum efficiencies of each photon detector.

When trying to produce an association metric a sample of 10,000 isolated positive muons generated with CRY at $T = 0$ was used. Isolated particles were used as then there should only be one long track with which to match one reconstructed flash. The positive muons were generated outside of the detector with a constant y position, above the uppermost scintillation counters, and flat distributions in x and z. When this sample was simulated it was clear that the photon detector reconstruction using the pre-built libraries worked well as the reconstructed flash source normally lay very close to the track which caused it. It was found that a Point of Closest Approach (PoCA) calculation of the reconstructed track to the reconstructed flash centre, gave an effective metric by which the flash and track could be associated. Other metrics such as the distance between the flash and track centres, and the perpendicular distance between the flash centre and the line joining the start and end of track were investigated but found to provide less reliable metrics. The latter of these metrics is less effective because the reconstructed tracks are rarely straight lines, due to particles scattering as they travel through the LAr, and so the perpendicular distance at each hit must be calculated. A comparison of these metrics is shown in Figure 5.1.

Another metric by which flashes could be assigned to reconstructed tracks is by utilising the relationship between the number of measured photoelectrons in the simulation, and the distance from the APAs at which they were produced. When considering two flashes of scintillation light that are produced at different distances from the APAs, it would be expected that more photoelectrons would be collected when the photons were produced closer to the APAs. This relationship is shown in Figure 5.2 where it can be seen that there is an exponential decay in the number of photoelectrons which are measured with increasing drift distances. Utilising this relationship, means that the distance from the APAs can be predicted from the number of photoelectrons which are measured. This predicted distance from the APA planes can then be compared to the expected x position of a reconstructed track given the difference in flash time and hit times, this is shown in Figure 5.3. The difference in these two quantities can then be used as the second metric as it gives an indication of how well the properties of a flash match the reconstructed x position of the track. If the predicted and reconstructed x positions are identical then the track and flash are well matched, this

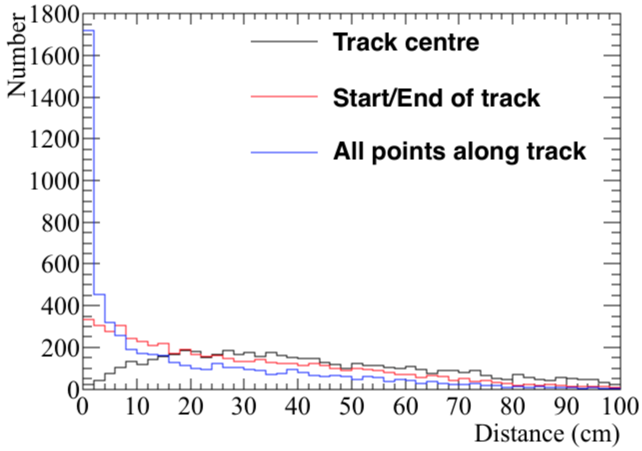

Fig. 5.1 The number of events as a function of the calculated distance between a reconstructed track and a reconstructed flash for various metrics. The distance between track centre and the flash centre is shown in black. The perpendicular distance between the flash centre and the line joining the start and end of the track is shown in red. The point of closest approach between the flash centre and all hits along the track is shown in red.

corresponds to the collection of points around the $y = x$ line in Figure 5.3.

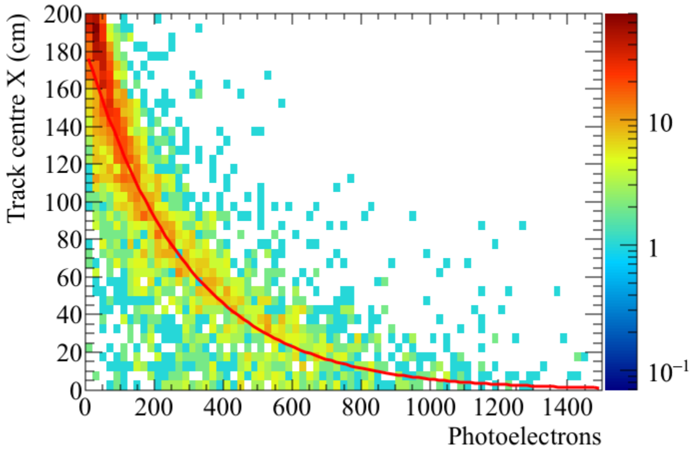

Fig. 5.2 The central x position of a reconstructed track versus the number of detected photoelectrons. The red line corresponds to a parameterisation of the distribution, so that the measured number of photonelectrons can be used to predict the central x position of the track, that the flash should be associated with.

Using these metrics it is possible to attempt to assign reconstructed flashes to reconstructed tracks. Only flashes which are within one drift window of a given track are considered, as flashes outside of this time window cannot have been caused by the reconstructed

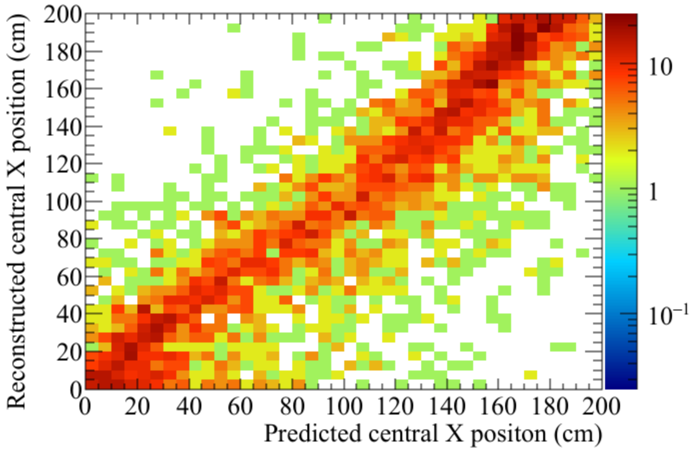

Fig. 5.3 A comparison of the x position predicted using the relationship in Fig 5.2 and the x position predicted by using the difference in flash and hit times.

track. Once flashes are assigned to tracks it is possible to determine how well the matching has performed by comparing the Monte Carlo truth interaction time with the photon detector interaction time. When doing this it is more useful to use a CRY sample which spans multiple drift windows, as then incoming particles will create scintillation flashes at random timings as opposed to all at $T = 0$ in the positive muon sample initially considered. The CRY sample over multiple windows contains many particles generated by CRY, and is not limited to only producing positive muons, meaning that it better represents the cosmic flux observed by the 35 ton detector. This comparison is shown in Figure 5.4, where there is a clear peak at a time difference of 0 ms in the Monte Carlo truth and photon detector times. When zooming in on this peak it can be seen that there is a systematic offset of 0.6 μs, this is due to an electronics offset applied in the simulation to the photon detector system.

From Figure 5.4 it can clearly be seen that the metric using the proximity of the flash centre to the track trajectory yields the best matches. This is likely caused by the large spread in the number of photoelectrons collected at fixed drift distances, as shown by Figure 5.2. The two metrics can be combined to give a prediction for the interaction time, though given the increased sensitivity from the proximity metric this should be given greater weighting. In physics data the metric using the number of collected photoelectrons is particularly sensitive to the absolute light level in the detector as a high residual light level would reduce the proportional change in the number of photoelectrons collected for increasing drift distances. This metric also relies a sample of tracks with known x positions upon which it can be calibrated which may be difficult to obtain.

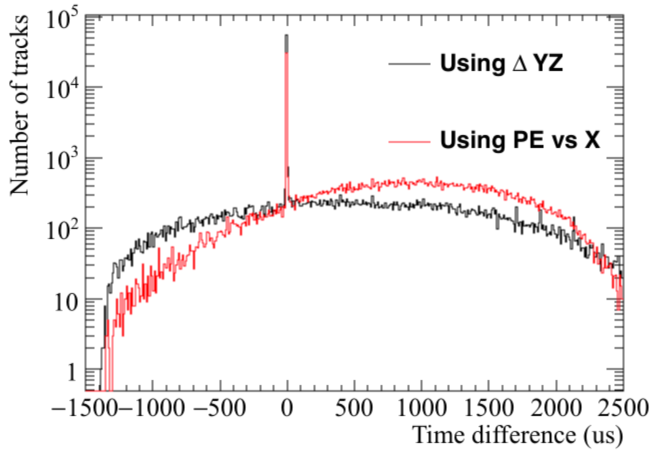

(a) The difference in interaction times.

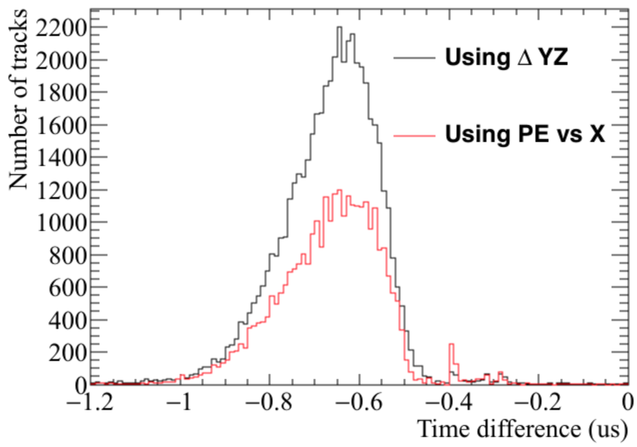

(b) Zoomed in at low time differences.

Fig. 5.4 The number of events as a function of the difference between Monte Carlo and photon detector times. The difference in interaction times over a large range of times is shown top. The peak at a time difference of 0 is expanded to show a sytematic offset of 0.6 μs, due to an electronics offset is shown bottom.

5.2 Calibrating calorimetric constants

Having the correct calorimetric responses is vital when trying to calculate $\frac{dE}{dx}$ as the measured change in charge has to be correctly converted to the change in energy. The parameter which has to be tuned in order to ensure that this is done correctly is the number of electrons that each ADC corresponds to. This was presented in Equations 3.1 and 3.2 as $C_{ADC\rightarrow e^-}$. Each plane will have a different response function, and so each plane has to be treated separately. These parameters have to be tuned in such a way as to make a known particle energy deposition have the correct $\frac{dE}{dx}$, the easiest deposition to tune against is the minimally ionising particle (MIP) peak, which in LAr should have a value of 1.8 MeV cm^{-1}. To do this the sample of 10,000 positive muons made to calibrate the photon detector track/flash assignment will be used as many of these particles will be MIPs.

To select the MIPs in the sample only tracks caused by through-going muons are used. The $\frac{dE}{dx}$ value for all hits in all tracks is then calculated, and the different planes are considered separately. A Gaussian distribution is then fitted around the peaks for each of the planes to discern the most probable value (MPV) of $\frac{dE}{dx}$ for that plane. If the MPVs are not equal to 1.8 MeV cm^{-1} then the ADC to electron parameters are scaled by the factor between the measured MPV and the MIP peak. As the relationship between $\frac{dE}{dx}$ and $C_{ADC\rightarrow e^-}$ is not linear an element of trial and error is required until the correct MPVs are measured. An example of the tuning being applied is shown in Figure 5.5. Tuning of the response functions is required whenever the electronics gains or signal shaping functions are changed.

5.3 Discerning reconstruction efficiencies

Knowledge of the strengths and weaknesses of different tracking algorithms is vital when using them for physics analyses. To this end it is useful to develop a metric by which they can be compared. In order to do this a series of conditions have to be applied to the reconstructed tracks from a large set of simulated particles which are reconstructed using different tracking algorithms. It is interesting to observe what the effect of event complexity has on the reconstruction algorithms and so efficiencies will be calculated for both of the CRY samples used in Section 5.1. The sample referred to as the positive muon sample contains single positive muons generated at $T = 0$, with a constant y position above the scintillation panels, and flat distributions in x and z. The sample reffered to as the CRY sample, contains multiple particles of multiple particle types, generated at times spanning multiple drift windows, and at an altitude above sea level of 0 m.

The criteria upon which to determine whether a particle is well reconstructed has to be carefully chosen as every definition will have limitations. For example, consider a particle that travels 100 cm in the active volume of the detector but is reconstructed as 2 separate tracks (tracks 1 and 2), with lengths 77 cm and 23 cm respectively. Firstly, should these tracks be merged, or left separate? If the reconstruction algorithms have found them to be separate tracks then it is likely that it would be difficult to ascertain that they are from the same particle in real data, and so in considerations here they are not merged. One metric of efficiency would be to consider a track well reconstructed if it has a length between 75% and

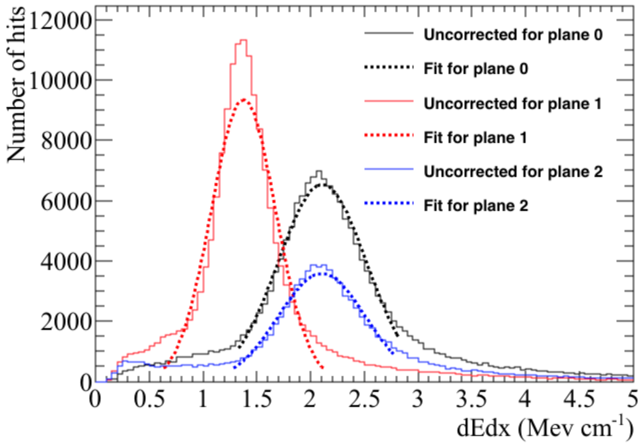

(a) Before tuning is performed.

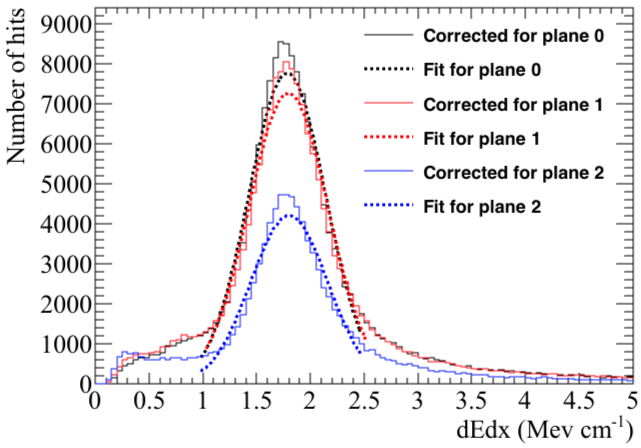

(b) After tuning is performed.

Fig. 5.5 The number of hits as a function the hit $\frac{dE}{dx}$, before and after a tuning is applied to the response functions for the conversion of ADC to number of electrons for each plane. The distribution of hit $\frac{dE}{dx}$ and the MPV of $\frac{dE}{dx}$ before tuning is shown top. The distribution of hit $\frac{dE}{dx}$ and the MPV of $\frac{dE}{dx}$ after tuning is shown bottom.

125% of the Monte Carlo truth length that the particle traversed in the detector, in which case track 1 would be considered well reconstructed. Another metric however would be to consider a track well reconstructed if the Monte Carlo truth distance the particle traversed in the detector is between 75% and 125% of the reconstructed length, in which case neither track would be considered well matched. Both metrics have used exactly the same tracks and a seemingly identical method of evaluating whether a track is well reconstructed or not, but have got the opposite results. As such it is wrong to say which consideration gives the correct result, but instead the result of each should be considered equally. It should also be noted that these are just two of a wide range of definitions one could use to quantify a well reconstructed track. In discussions here the former definition of efficiency will be used, such that a track is considered well reconstructed if:

- Reconstructed track length is more than or equal to 75% of the Monte Carlo track length.
- Reconstructed track length is less than or equal to 125% of the Monte Carlo track length.
- Only one reconstructed track can be matched per Monte Carlo particle.

When calculating efficiencies it is important to consider much more than just the ratio of reconstructed to true track length. To this end efficiencies with regards to many aspects of the tracks are calculated:

- Track length,
- Energy deposited in the active volume of the detector,
- The angle θ of the track, defined as the angle that a vector makes from the x axis in the xy plane,
- The angle ϕ of the track, defined as the angle between the z axis and the vector.

In all efficiency plots the Monte Carlo truth quantity, not the reconstructed quantity is shown so as to reflect how the variations of these quantities affect the reconstruction efficiencies. It is also useful to observe the effect on reconstruction of failed disambiguation and incorrect interaction time determination. To show this, two forms of reconstruction are ran on the particles. One reconstruction path uses no Monte Carlo information and so the interaction time is determined using the simulated photon detectors as described in Section 5.1. The second reconstruction path uses cheated disambiguation and interaction time determination. Cheated disambiguation means using the Monte Carlo truth information of the energy deposition to correctly assign which wire segment the energy was deposited on.

The calculation of reconstruction efficiencies also serves as an effective method upon which reconstruction algorithms can be further developed as it identifies aspects which do not work as expected. For example when the efficiencies for the CRY sample were initially calculated they were significantly lower than for the positive muon sample, but only when disambiguation was not cheated. It transpired that this was because the disambiguation was only selecting the largest collection of hits on each plane for each TPC. This is not a problem when only 1 particle is simulated and will reduce the number of noise hits but in a CRY sample of 16 ms there will almost certainly be multiple particles in each TPC. Removing the hits from all but one of these multiple particles will cause them to have no reconstructed track, and thus cause the efficiency to drop significantly. Upon making the disambiguation algorithm no longer have this restriction the reconstruction efficiencies of the positive muon and CRY samples were observed to become much more similar.

The reconstruction efficiencies given the current state of the most commonly used reconstruction algorithms are shown in Figures 5.6, 5.7, 5.8, 5.9 and 5.10. Efficiencies are shown for both the positive muon and CRY samples, where it can be seen that the efficiency tends to be lower for the CRY sample. It is thought that this is due to the more complex event structure in the CRY sample, as multiple primary particles will be present in the detector at any given time. The relatively slow drift velocity of LAr may mean that these tracks cross in wire-tick space. Tracks crossing in wire-tick space could cause reconstruction errors as the overlaps may be mistaken for interactions, which would cause the tracks to be split, resulting in the interaction time calculated from the photon detectors to be incorrect. This error, in the calculation of interaction time using the photon detectors, was seen in Figure 5.4. The reconstruction efficiencies for the CRY sample are more realistic as events will rarely be isolated in the detector due to the large flux of cosmic particles on the Earth's surface.

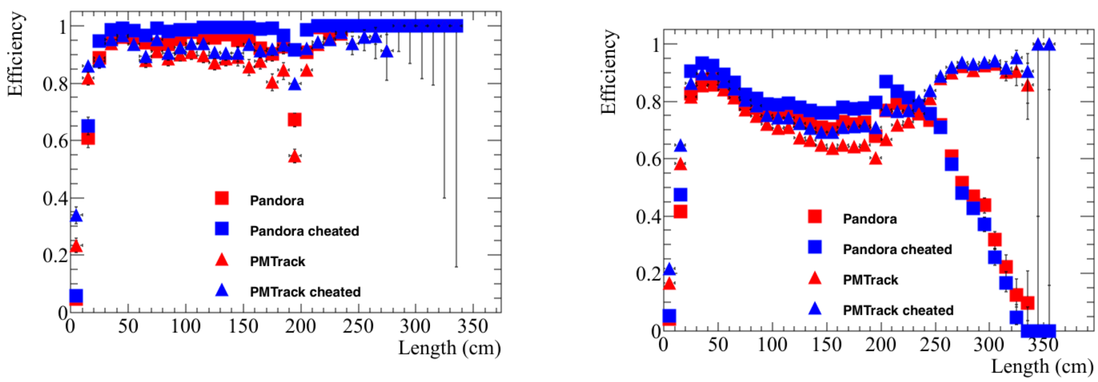

(a) Reconstruction efficiencies for an positive muon sample.

(b) Reconstruction efficiencies for a CRY sample.

Fig. 5.6 The reconstruction efficiencies for simulated events as a function of Monte Carlo truth track length. The efficiencies are shown for 'non-cheated' reconstruction (in red), and 'cheated' reconstruction (in blue), for both pandora (squares) and PMTrack (triangles).

A striking feature of Figure 5.6 is the rapid decrease in reconstructed efficiency for the CRY sample for track lengths above 250 cm when using Pandora. The cause of this is that

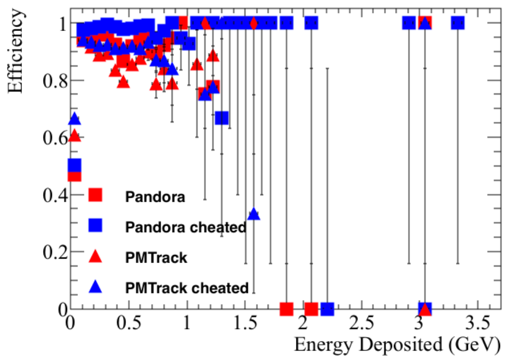

(a) Reconstruction efficiencies for an positive muon sample.

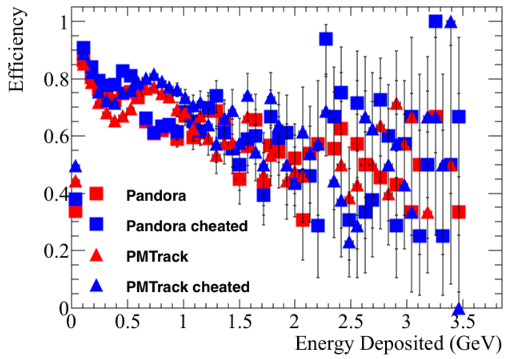

(b) Reconstruction efficiencies for a CRY sample.

Fig. 5.7 The reconstruction efficiencies for simulated events as a function of Monte Carlo truth deposited energy. The efficiencies are shown for 'non-cheated' reconstruction (in red), and 'cheated' reconstruction (in blue), for both pandora (squares) and PMTrack (triangles).

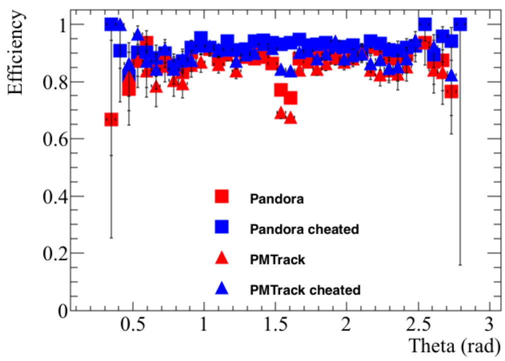

(a) Reconstruction efficiencies for an positive muon sample.

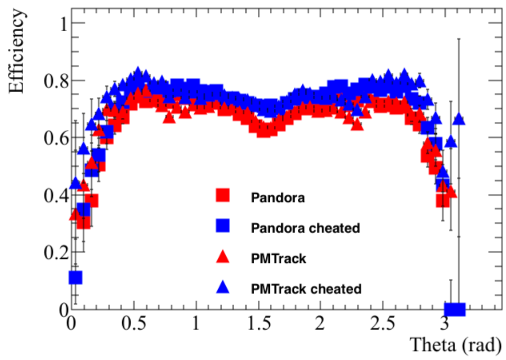

(b) Reconstruction efficiencies for a CRY sample.

Fig. 5.8 The reconstruction efficiencies for simulated events as a function of Monte Carlo truth track angle in theta. The efficiencies are shown for 'non-cheated' reconstruction (in red), and 'cheated' reconstruction (in blue), for both pandora (squares) and PMTrack (triangles).

tracks are reconstructed separately in the long and short drift volumes before being merged when they are found to be co-linear in the yz plane. This is not a problem in the positive muon sample as the x position of the hits calculated using Equation 5.1 will be correct. Where, x_{Hit} is the calculated x position of the hit, T_{Hit} is the measured time of the hit, and v_{Drift} is the electron drift velocity. An electron, in an electric field of 500 V cm^{-1}, in LAr, drifts at a speed of 0.160563 cm μs^{-1}.

$$x_{Hit} = T_{Hit} \times v_{Drift} \tag{5.1}$$

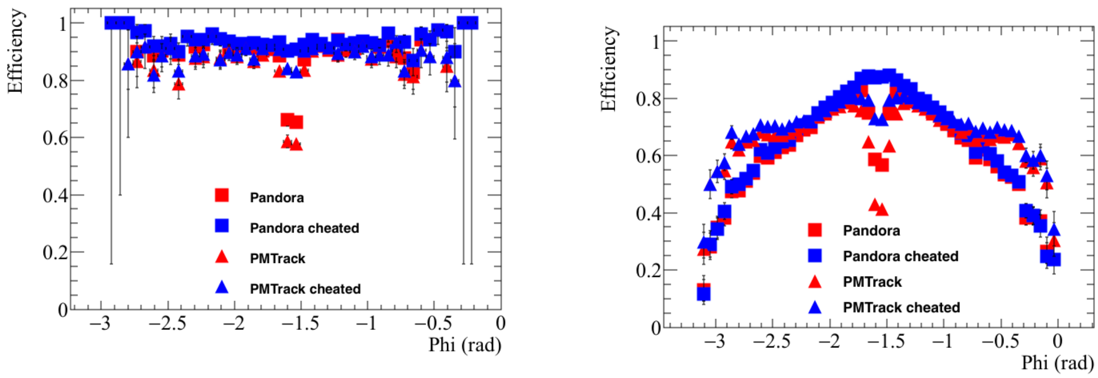

(a) Reconstruction efficiencies for an positive muon sample.

(b) Reconstruction efficiencies for a CRY sample.

Fig. 5.9 The reconstruction efficiencies for simulated events as a function of Monte Carlo truth track angle in phi. The efficiencies are shown for 'non-cheated' reconstruction (in red), and 'cheated' reconstruction (in blue), for both pandora (squares) and PMTrack (triangles).

However, when the same is done for hits in the CRY sample using particles with large interaction times, the x positions will have offsets proportional to the interaction time of the particle, unless the hit time is corrected by Equation 5.2. Where T_{Hit} is the corrected hit time, $T_{Measured}$ is the measured time of the hit, and $T_{Interaction}$ is the calculated interaction of the particle which caused the hit.

$$T_{Hit} = T_{Measured} - T_{Interaction} \tag{5.2}$$

This is due to particles being generated at large interaction times, as opposed to all at $T = 0$, as in the positive muons sample. For example, if a particle is generated at a time of $T = 12.5$ ms, then the offset in x position would be more than 20 m, using Equation 5.1. Obviously the hits could not have occured at those positions, as the drift distances are roughly 30 cm in the 'short' drift volume, and 250 cm in the 'long' drift volume. However, if tracks which are reconstructed separately in the 'short' and 'long' drift volumes, are merged before this x offset is corrected for, then the combined track length will have a discontinuity in x of more than 40 m! As the interaction time of the track is calculated using the output of the tracking algorithms it is not possible to prevent this by using the interaction time at present. It is however, possible to subtract this jump in x position from the track length quantity which is calculated when the stitched track is stored in the event. This will give the correct track length, though the user will still have to correct individual hit positions in later analyses, using the calculated interaction time. This is what is done by PMTrack, hence it not exhibiting this rapid decrease in reconstruction efficiency for long tracks. The interaction time can be found

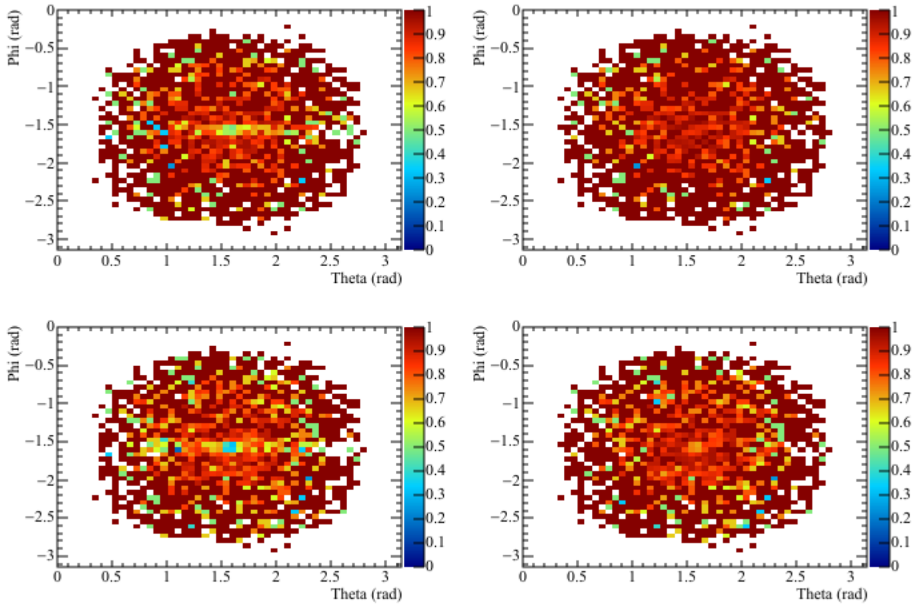

(a) Reconstruction efficiencies for an positive muon sample.

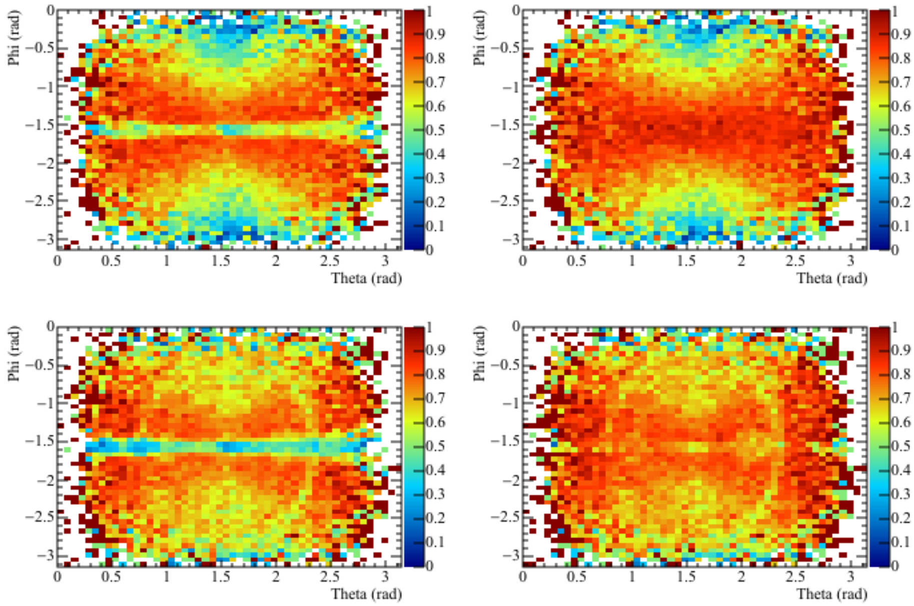

(b) Reconstruction efficiencies for a CRY sample.

Fig. 5.10 The reconstruction efficiencies for simulated events as a function of Monte Carlo truth track angle in theta and phi. The track angle in theta is shown on the *x* axis, and the track angle in phi is shown on the *y* axis. The efficiencies are shown for non-cheated reconstruction (plots on the left) and cheated reconstruction (plots on the right) for both Pandora (plots on the top) and PMTrack (plots on the bottom).

from, among other things, the Monte Carlo truth generation time, or the photon detectors.

It is clear from Figure 5.6 that particles with track lengths less than 30 cm are poorly reconstructed. The very low efficiency for particles with track lengths less than 10 cm can be partially attributed to, Monte Carlo truth particles with track lengths of less than 1 cm, in the active volume of the detector. These particles, which represent 30% of the particles with active volume track lengths of less than 10 cm, are too short to be reconstructed using the current reconstruction process. These particles will need to be reconstructed when looking for supernovae bursts, though special algorithms will be written to do this, as the traditional hit finding and clustering algorithms may discard them due to the isolated nature of the hits. Another issue is that the low energies of these particles may mean that the signals that they produce are below threshold and so will not even be reconstructed, or if hits are reconstructed, they may be too close to a more energetic track, and get absorbed into them. The reconstruction of tracks is affected by the number of wires which they cross, though this should not matter for particles with lengths of more than 5 cm in the active volume, as they will have crossed roughly 10 wires in each plane, which should produce enough unique hits for a cluster to be reliably constructed. This can be seen to be the case for PMTrack when considering the positive muon sample, as the efficiency for particle track lengths between 10 and 20 cm is roughly the same as that for track lengths between 20 and 30 cm, however when considering the CRY sample there is still a significant decrease in efficiency. This is attributed to secondary particles which are produced in hadronic interactions with the concrete surrounding the detector. Many of these particles will travel only very short distances in the active volume, though those that travel slightly larger distances are likely to cause energy depositions that will be confined to the detector edges. The tracking algorithms may struggle to accurately reconstruct these tracks, as signifcant portions of the track will be close to the detector edge, where the field is poorly modelled and hits may be more difficult to disambiguate.

The trend of increasing efficiency for longer track lengths from Figure 5.6 can also be seen in Figure 5.7 as the amount of deposited energy increases. This is because particles which deposit more energy will tend to have travelled further in the detector. The amount of energy that particles deposit is limited by the size of the detector, as particles with an energy of more than 1 GeV are energetic enough to be MIPS. This results in few particles depositing more than 1 GeV in the detector. The result of this is that the uncertainty in the reconstruction efficiency increases above 1 GeV. The larger range in the amount of energy deposited seen in Figure 5.7b, is due to the larger number of muons in the CRY that create large electromagnetic showers upon entering the LAr.

It is also interesting to note the pronounced decreases in reconstruction efficiencies for particular angles, shown in Figure 5.8 and Figure 5.9. The decrease in efficiency at $\phi = \frac{\pi}{2}$ can be attributed to the drop in efficiency for particles with track lengths between 190 cm and 200 cm. This is because the vertical height of the detector is approximately 195 cm, and near vertical tracks will hit few collection wires, meaning that determining the triple points needed by the disambiguation is very difficult. This is verified by the large increase in efficiency achieved by cheating the disambiguation, as seen in Figure 5.8a, where the reduction in reconstruction efficiency is seen to become much less pronounced. Similarly the decrease in efficiency at $\theta = \frac{\pi}{2}$ can be attributed to particles which are perpendicular to the collection wires resulting in few collection wires being hit.

The information from Figures 5.8 and 5.9 is combined in Figure 5.10, where the sharp drop in efficiency at $\phi = \frac{\pi}{2}$ for the 'non-cheated' CRY sample, is particularly visible. The effect of cheated disambiguation is clear in Figure 5.10b where the dip in efficiency as a function of θ at fixed $\phi = \frac{\pi}{2}$ is completely removed. The same is not true however, for the dip in efficiency as a function ϕ at fixed $\theta = \frac{\pi}{2}$, though the reduction in efficiency was not as severe as that seen for fixed values of $\phi = \frac{\pi}{2}$. The effect of 'cheated disambiguation' can still be seen though, as the reconstruction efficiency in Figure 5.10b can be seen to improve for values of ϕ. There are still however, noticeable decreases in the reconstruction efficiency for values of ϕ close to 0 or π, when using Pandora. The improvement in the performance of the reconstruction algorithms that comes from 'cheating' the reconstruction is part of the motivation for the wire pitches in the DUNE FD being 36° as opposed to the $45\pm0.7°$ used in the 35 ton. This is because, as discussed in Section 3.5, the shallower wire pitch makes disambiguation easier. Though disambiguation will be easier in the different geometry, further efforts to improve disambiguation are still required, as are continued efforts to reconstruct the shortest tracks.

5.4 Performing particle identification

Being able to perform reliable particle identification (PID) is a key requirement for the DUNE experiment, and so efforts have been made to establish a procedure by which this can be achieved. The predominant method of performing PID in LAr is to use the relationship between $\frac{dE}{dx}$ and the residual range of the track, defined as being the distance between a point on the track and the stopping point of the track. This relationship is observed to be dependent on particle mass and is quantified by the Bethe-Bloch equation [21] [22] which is shown in Figure 5.11 and presented in Equation 5.3.

$$-\frac{dE}{dx} = Kz^2\frac{Z}{A}\rho\frac{1}{\beta^2}\left[\frac{1}{2}\ln\frac{2m_ec^2\beta^2\gamma^2T_{max}}{I^2} - \beta^2 - \frac{\delta(\beta\gamma)}{2}\right] \tag{5.3}$$

The sharp increase in energy loss per unit length can be seen to occur at different momenta for different particle masses meaning that the peak value of $\frac{dE}{dx}$ can change significantly. One example of a large change in the peak value of $\frac{dE}{dx}$ can be seen by comparing muons and protons, whist muons and pions are very similar.

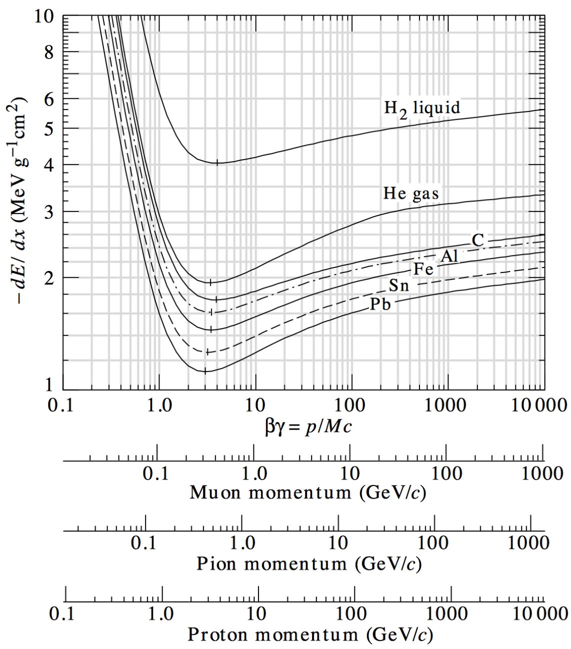

Fig. 5.11 The Bethe-Bloch equation describes energy loss per unit length as a function of energy in different mediums. The energy losses expected for different particle types is shown in different mediums. Liquid Argon with a density of 1.4 g cm^{-3} has a density slightly less than that of Carbon at 1.8 g cm^{-3} [23].

The particle mass dependence can be seen by plotting the $\frac{dE}{dx}$ against the residual range of the particle on a log-log plot, as shown in Figure 5.12a. A power law dependence is found to describe the relationship [19], as shown in Equation 5.4. The dependence on b is found to be weak, and so can be set to -0.42 for all particle masses. This means that the main discriminant used is the A parameter, which has a strong dependence on particle mass. The values for A and b calculated from Figure 5.12a are shown in Table 5.1. It is found that the error in-

Table 5.1 Stopping power parameterization for various particle types in LAr [19].

Particle	A MeV cm$^{-(1-b)}$	b
Pion	8	-0.37
Kaon	14	-0.41
Proton	17	-0.42
Deuteron	25	-0.43

troduced by fixing the b parameter is small compared to the error from ionisation fluctuations.

$$\frac{dE}{dx} = AR^b \tag{5.4}$$

$$A_i = (\frac{dE}{dx})_i \times R_i^{0.42} \tag{5.5}$$

Once the b parameter is set to be constant for all particle types it is possible to calculate a value for the A parameter for each hit on the track using Equation 5.5, where R_i is the residual range of the track at that point. The particle type discriminant, called PIDA, can then be calculated for a track by finding the average value of A_i for the track. As the particle mass dependant increase in $\frac{dE}{dx}$ only occurs near the end of the track, the PIDA variable can only be calculated for particles which stop in the detector as all other particles will have MIP-like $\frac{dE}{dx}$ distributions and so cannot be identified in this way. As shown by the plotted range of Figure 5.12a the average value of A is normally calculated for the last 30 cm of the track.

The PIDA method was tested in [19], where the PIDA values were calculated for Monte Carlo particles which stopped in the detector using truth information over the last 30 cm of the particle lengths. This is shown in Figure 5.12b, where a clear separation can be seen between the peaks for Muons, Pions, Kaons and Protons. Though the Muon and Pion peaks are relatively close together they can still be resolved in the plot due to little overlap. It is interesting to note how tight the PIDA distributions found in the paper are, which allows the different particles types to cleanly separated in the truth study. The author notes that an incorrect tuning of the recombination effects will cause the distributions to become broader, and an incorrect calibration of the detector will introduce a systematic shift in the expected values of PIDA.

From Figure 5.12 it can be seen that the most distinct PIDA distributions are that of muons and protons, these are also two of the most common particle types in cosmic rays. For

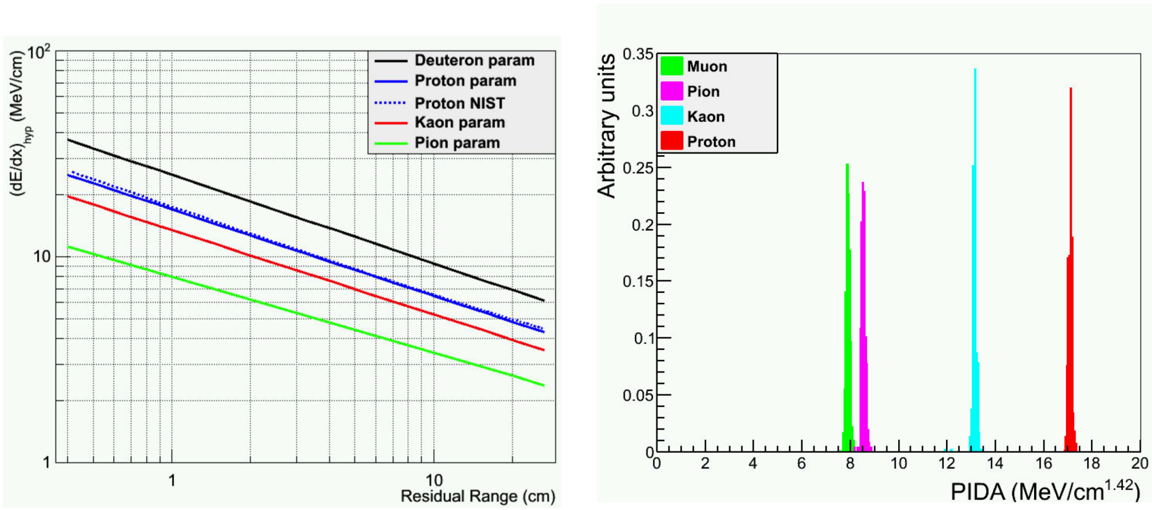

(a) Stopping power for different particle masses.

(b) Distribution of PIDA values for different particle masses.

Fig. 5.12 Defining the PIDA metric for particle identification and testing it on a Monte Carlo sample using truth information.

these reasons particle identification using the PIDA variable will be attempted on simulations of the 35 ton. As outlined in Sections 5.1 and 5.2 in order to do this the interaction times of particles have to be well known and the calibration constants must be tuned so as to ensure that the effects of recombination are properly accounted for. It is also useful to use the information found in Section 5.3 about the efficiency with which tracks are reconstructed. In this regard it is useful to produce additional figures showing the reconstruction efficiencies of protons in the CRY sample, these are shown in Figure 5.13.

Figure 5.13 shows that the average reconstruction efficiency for PMTrack is higher than that for Pandora when considering protons, as the efficiency for the former is roughly 10% higher for all angles as shown in Figure 5.13c, though it is much lower than the overall efficiency seen in Figure 5.8b. From Figure 5.13a it is evident that the efficiency for protons with track lengths of more than 10 cm is similar to that of the overall efficiency for the CRY sample, but the efficiency for the shortest tracks is significantly lower than that of the whole CRY sample. A review of the true path lengths of the simulated particles shows that 60% of the protons have path lengths of less than 1 cm and that none of these particles were reconstructed, it is this large number of very short particles which causes the overall reconstruction to be relatively low. When a minimum path length of 1 cm (10 cm) is required the reconstruction efficiency rises to 37% (58%), so when the shortest tracks are not counted the reconstruction performs reasonably well.

It is also useful to produce samples where the primary particle is a single muon or proton located in the active volume of the detector. This allows for a sample of isolated tracks to be made upon which the capabilities of the PIDA metric can be tested. It also allows the reconstruction efficiency to be found for particles in isolation. The properties of the generated particles are illustrated below in Table 5.2. The values of the simulated quantities were found by changing the given parameters by an amount taken from a random sampling of a Gaussian distribution of width equal to the error listed. These simulation parameters were chosen to produce samples which would contain both exiting and stopping particles whilst generating the particles in the LAr would ensure that there should always be a reconstructable track in the detector.

The reconstruction efficiencies when using the PMTrack reconstruction method are shown for the simulated particles in Figure 5.14. It should be noted that truth particles with track lengths of less than 1 cm have been excluded from these plots which is why the angular reconstruction efficiencies for protons in Figures 5.14c and 5.14d, are higher than those seen in Figures 5.13c and 5.13d. This was done as due to how the initial momenta and positions are sampled many of the primary simulated particles may travel very short distances that are contained in spaces between TPCs and including these particles would artificially reduce the efficiency presented. After discounting these very short particles the efficiencies generally follow similar patterns observed in the earlier efficiency plots, though there is a decrease in efficiencies for the longest track lengths which is not observed in other samples. This is attributed to the initial positions for the particles being within the detector volume, as this means that any particle travelling over 100 cm would have a very peculiar trajectory as the edge of the detector should never be more than 100 cm away from the starting position. The only exception to this is if a particle travelled along the x axis to the other end of the detector, which as discussed earlier is a very problematic orientation to reconstruct as all of the charge would be deposited over a large range of time on very few collection plane wires.

As the increase in $\frac{dE}{dx}$ is only visible when the particle stops in the detector it is necessary to remove exiting particles from the sample by applying a fiducial cut on the end point of the reconstructed track. It is important to only place this on the end point of the track, as one does not want to remove particles which enter the detector and then stop. When calorimetry is performed the end point of the track is determined using, among other metrics, the increase in $\frac{dE}{dx}$ and so the residual range of the track (a stored data member of the track

Table 5.2 The properties of initial particles simulated in the muon and proton samples.

	Muon properties	Proton properties
Initial position (cm)	(100 $\pm$ 50, 0 $\pm$ 30, 80 $\pm$ 20)	(100 $\pm$ 50, 0 $\pm$ 30, 80 $\pm$ 20)
Initial momentum (GeV)	0.3 $\pm$ 0.1	0.8 $\pm$ 0.5
Initial θ_{XZ} ($^\circ$)	0 $\pm$ 180	0 $\pm$ 180
Initial θ_{YZ} ($^\circ$)	-45 $\pm$ 45	-45 $\pm$ 45

object) should always refer to the distance to the end of the particles trajectory. For this study a fiducial cut of 5 cm is used, meaning that any track with hits within 5 cm of the edge of the detector volume is discarded and counted as an exiting particle. This should mean that very few tracks due to exiting particles are identified as stopping in the detector as it would require that a large section of the track would have to un-reconstructed. This will mean that some stopping particles are incorrectly assigned as exiting particles causing the identification efficiency to drop, but it is necessary to ensure that exiting particles are not included in the final distributions. A further cut that is applied is the requirement that there are a minimum of 5 continuous collection plane hits, this is to ensure that an adequate number of points are taken upon which to find an average value of PIDA for the track. Similar cuts are described in [19], and the resulting distributions of PIDA values for the single proton and muon samples are shown in Figure 5.15.

As can be seen from Figure 5.15 using truth information can make the distributions much cleaner, particularly when discounting particles for which the reconstruction algorithms do not track to their end point. A track is identified as having a correct end point if the reconstructed end point is within 2.5 cm of the true end point of the particle. It is reassuring to see that few tracks are reconstructed backwards, as if this were not the case then performing particle identification would be very difficult as it would indicate that the calorimetry and tracking algorithms are not performing well. Improvements can still be made though, as both plots in Figure 5.15 contain tracks which do not have the final energy depositions. This can seen as when tracks which do not match with the true end points of the particles are removed the low tails of the PIDA distributions are significantly reduced. It is observed that the PIDA distributions are cleaner when information from all three wire planes are used as opposed to only using the collection plane and so that is what is presented here. This shows how important it is to calibrate the electronics responses of all three wire planes and how additional wire planes can improve calorimetry as well as the accuracy of reconstruction algorithms.

The relationship between the $\frac{dE}{dx}$ and residual range of a track is shown in Figure 5.16 for both protons and muons. The much steeper increase in $\frac{dE}{dx}$ at low residual range for protons compared to muons is clearly visible when comparing Figures 5.16a and 5.16b. The contamination in the proton sample at low PIDA can be seen in Figure 5.16a where there is a clear sample of tracks for which the $\frac{dE}{dx}$ does not increase for low residual ranges. These plots are filled after tracks which do not correlate to the ends of the true trajectories are removed, and so the tail of low $\frac{dE}{dx}$ values is due to particles for which the simulated detector did not find increased energy depositions as the particle stopped. It is interesting to note that when a simple version of PIDA is calculated using the MC truth energy deposits, shown in Figure 5.17, these particles are also found to have low PIDA values. It is therefore possible that at least some of these protons do not in fact stop, but interact inelastically when they still have a significant amount of kinetic energy meaning that GEANT4 will create a new particle and the tracking algorithms are creating a new track after this interaction.

It is useful to summarise the information shown in Figure 5.15 in a table so that an efficiency of identifying stopping particles can be found. This is shown in Table 5.3 for protons, and in Table 5.4 for muons. The efficiency shown in these tables is defined as the number of tracks in the PIDA range divided by the total number of stopping particles, this is why the 'efficiency' is more than 100% for the number of reconstructed tracks in Table 5.4. The purity shown in these tables is defined as the percentage of tracks in the PIDA range which are associated with particles which actually stop in the detector. As many of the reconstructed tracks shown in Table 5.4 are not due to stopping particles the purity is low. The PIDA ranges referred to are 14-18 and 5-9 for the protons and muons respectively, as these ranges cover the peaks of the distributions shown in Figure 5.16 and are centered on the peaks in Figure 5.12b.

As can be seen in Table 5.3 the efficiency upon which protons can be identified does not change significantly as the sequential criteria are applied, but as shown in Figure 5.15a the low PIDA peak decreases significantly. The same cannot be said for the muon sample however, as when the criteria that the tracking end point matches the true end point is applied a significant section of the tail within the PIDA range is removed. The resulting distribution is more similar to the distribution shown in Figure 5.12b though, showing that it preserves the stopping tracks which are reconstructed best. The cut to remove tracks that do not have the correct end points reduces both sets of efficiencies, but if all the tracks were reconstructed with the correct end points then one can imagine that the number of tracks within the PIDA ranges would increase and the distributions would become more symmetrical as shown in

Table 5.3 A summary of the PIDA values calculated for the proton sample as sequential cuts are applied.

Applied cut	Proton sample			
	Tracks	In PIDA range	Efficiency	Purity
Total stopping particles	13295			
Reconstructed tracks	8761	3009	22.6%	98.7%
Survives 5 cm fiducial cut	7552	2894	21.8%	99.9%
Minimum of 10 collection plane hits	6186	2507	18.9%	99.9%
Correct track orientation	6022	2491	18.7%	99.9%
Correct tracking end point	4432	2288	17.2%	100%

Table 5.4 A summary of the PIDA values calculated for the proton sample as sequential cuts are applied.

Applied cut	Muon sample			
	Tracks	In PIDA range	Efficiency	Purity
Total stopping particles	6880			
Reconstructed tracks	9883	8907	129%	67.4%
Survives 5 cm fiducial cut	7126	6259	90.9%	90.2%
Minimum of 10 collection plane hits	6580	5876	85.4%	89.9%
Correct track orientation	6436	5767	83.8%	90.1%
Correct tracking end point	3676	3555	51.7%	100%

Figure 5.15b. Both tables also exhibit high purities which shows that the fiducial cut designed to removing exiting particles is effective, with only 2 exiting protons being mis-identified in the proton sample.

From Table 5.3 it can be seen that there are more stopping protons than primary protons as only 10,000 primary protons were generated. The effectiveness of the PIDA algorithm at identifying only primary protons is shown in Table 5.5. Comparing both tables it can be seen that the efficiency with which the primary protons can be identified is larger than the secondary protons as the efficiencies shown in Table 5.3 are lower than those in Table 5.5. It is thought that this is due to the low reconstruction efficiency for the very shortest tracks which many of the secondary protons have, as discussed in Section 5.3. A similar table is not produced for primary muons as there were no secondary muons produced in the muon sample, and so Table 5.4 is itself the efficiency with which the primary muons can be identified.

Table 5.5 A summary of the PIDA values calculated for the primary particles in the proton sample as sequential cuts are applied.

Applied cut	Proton sample			
	Tracks	In PIDA range	Efficiency	Purity
Total stopping particles	7798			
Reconstructed tracks	5920	1937	24.8%	98.9%
Survives 5 cm fiducial cut	5044	1878	24.1%	99.9%
Minimum of 10 collection plane hits	4485	1711	21.9%	99.9%
Correct track orientation	4363	1707	21.9%	99.9%
Correct tracking end point	3122	1565	20.1%	100%

Upon verifying that the PIDA metric can reliably determine particle type when they are simulated in isolation, the next step is to observe the accuracy upon which particles can be identified in a CRY sample. The sample used here differs from the CRY sample used earlier in that only events which contain a proton in the detector are reconstructed, this is done to reduce simulation time and storage space as this cut will still provide a substantial number of muons whilst ensuring that a large proton sample can be reconstructed. The process of calculating PIDA values for the tracks is identical in all samples, though as discussed in Section 5.3 the much more complicated event structure in the CRY sample affects the reconstruction efficiency and so will likely also affect the accuracy of the calorimetry. The calorimetry will be affected in two ways, firstly the reduced performance of the reconstruction algorithms will mean that some particles are not reconstructed at all, whilst those that are reconstructed may be more likely to have missing hits meaning that the end points may be less well reconstructed. This will cause the tail of low $\frac{dE}{dx}$ values seen in Figure 5.16a to be more pronounced. Secondly, as shown in Figure 5.4 though the photon detector time determination is very accurate for a large number of tracks it is also incorrect for a number of tracks, this will cause the recombination correction to be miscalculated which will in turn increase the calculated $\frac{dE}{dx}$ and hence PIDA values.

The PIDA values calculated for protons and muons in the CRY sample are shown in Figure 5.18. As can be seen from Figure 5.18b there is a tail of very high PIDA value muon tracks which contaminate the proton PIDA region of interest (ROI). This causes a serious problem when trying to identify protons from a cosmic sample as the number of muons present is significantly larger than the number of protons. The result of this will be a sample of tracks which will not be very pure, and so further cuts will have to be developed to enhance the purity of this sample whilst not reducing the efficiency upon which proton tracks are identified.

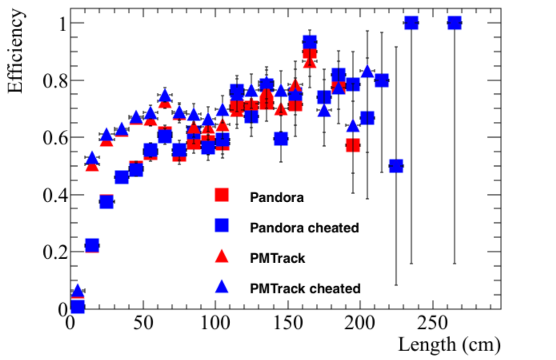

(a) The reconstruction efficiency as a function of Monte Carlo truth track length.

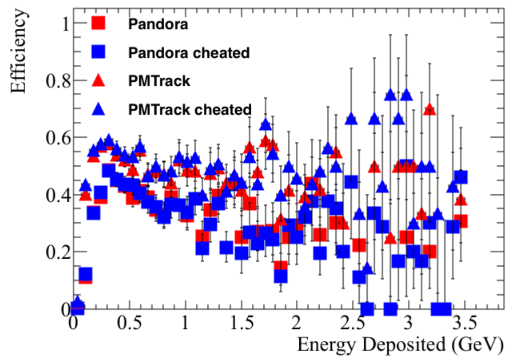

(b) The reconstruction efficiency as a function of Monte Carlo truth deposited energy.

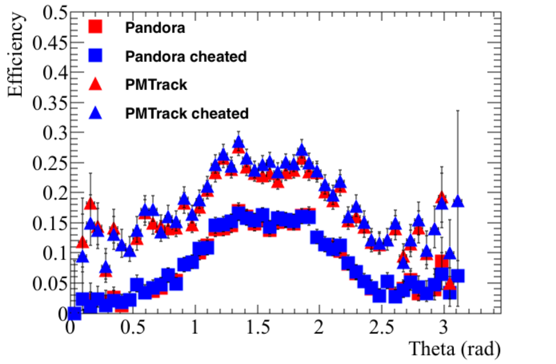

(c) The reconstruction efficiency as a function of Monte Carlo truth track angle in theta.

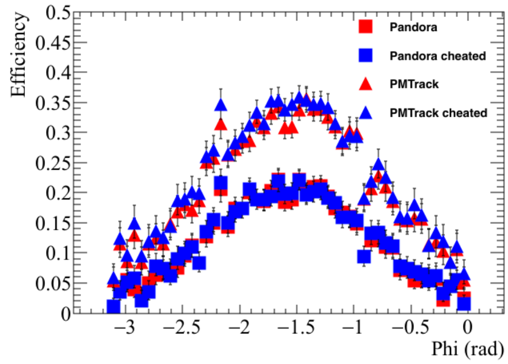

(d) The reconstruction efficiency as a function of Monte Carlo truth track angle in phi.

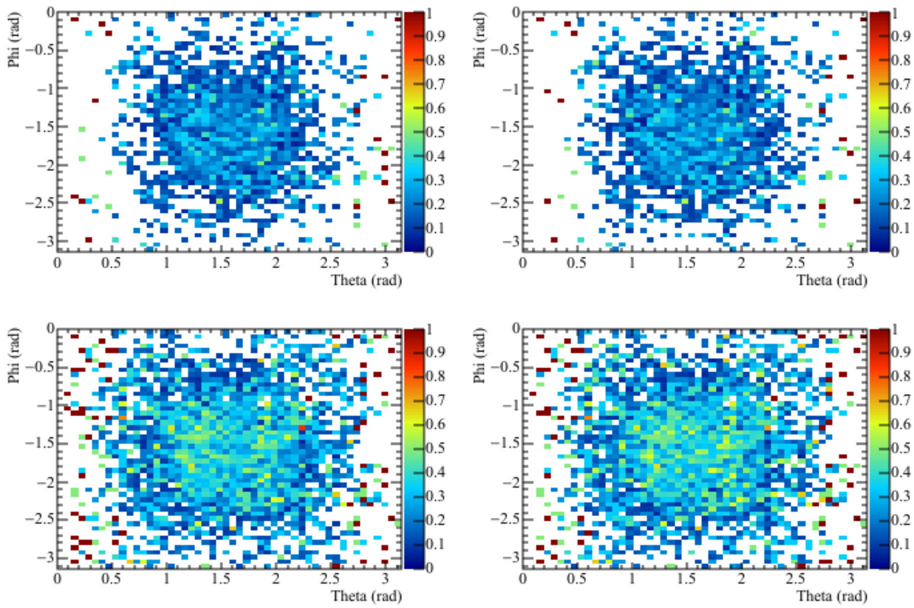

(e) The reconstruction efficiency as a function of Monte Carlo truth track angle in theta and phi.

Fig. 5.13 The reconstruction efficiencies for protons in a sample generated using CRY. The efficiencies are shown for 'non-cheated' reconstruction (in red), and 'cheated' reconstruction (in blue), for both pandora (squares) and PMTrack (triangles).

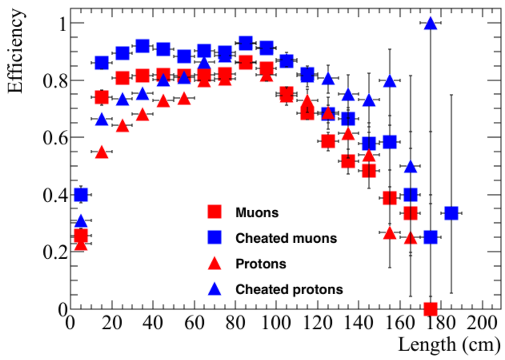

(a) The reconstruction efficiency as a function of Monte Carlo truth track length.

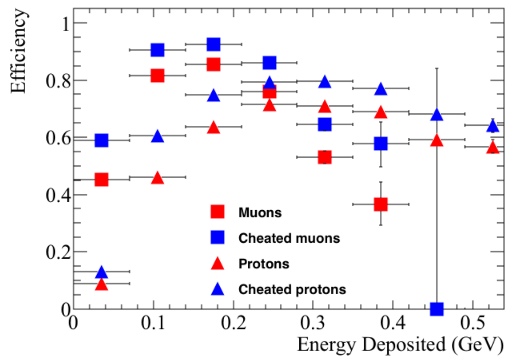

(b) The reconstruction efficiency as a function of Monte Carlo truth deposited energy.

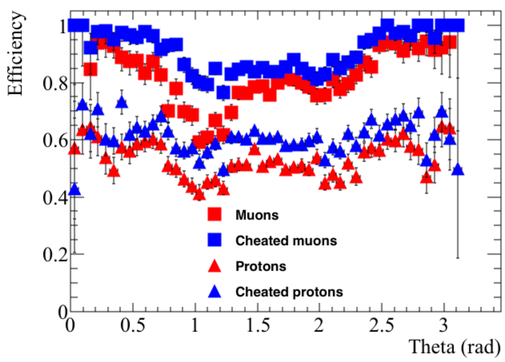

(c) The reconstruction efficiency as a function of Monte Carlo truth track angle in theta.

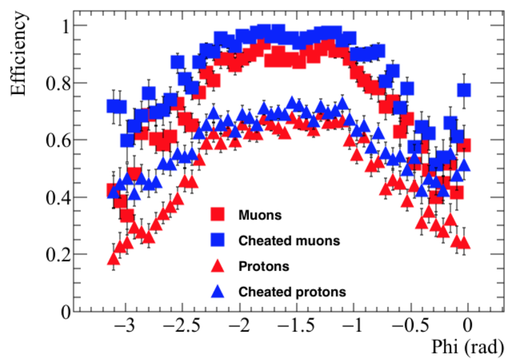

(d) The reconstruction efficiency as a function of Monte Carlo truth track angle in phi.

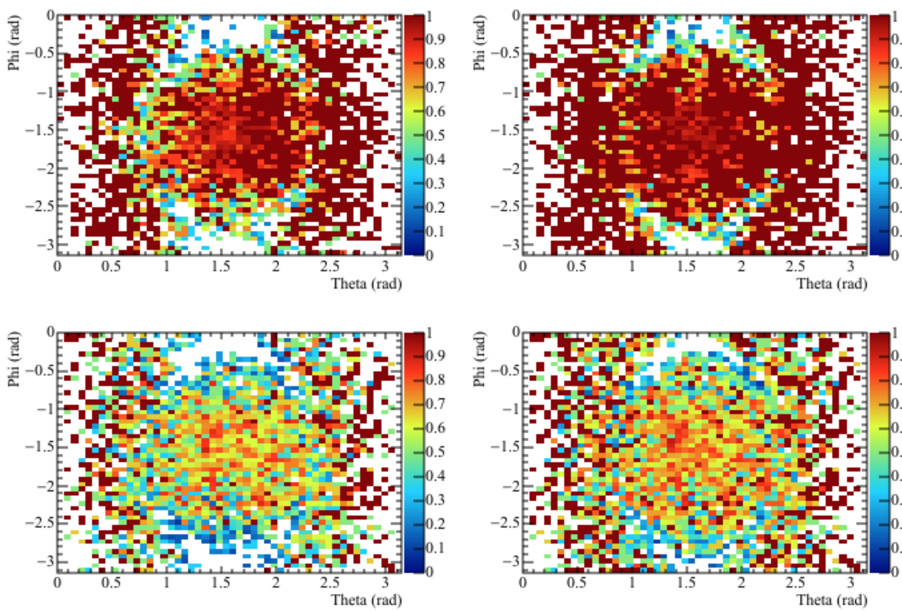

(e) The reconstruction efficiency as a function of Monte Carlo truth track angle in theta and phi.

Fig. 5.14 The reconstruction efficiencies for single muons and protons in the 35 ton. The efficiencies are shown for non-cheated reconstruction (red blocks) and cheated reconstruction (blue blocks) for both muons (square blocks) and protons (triangle blocks).

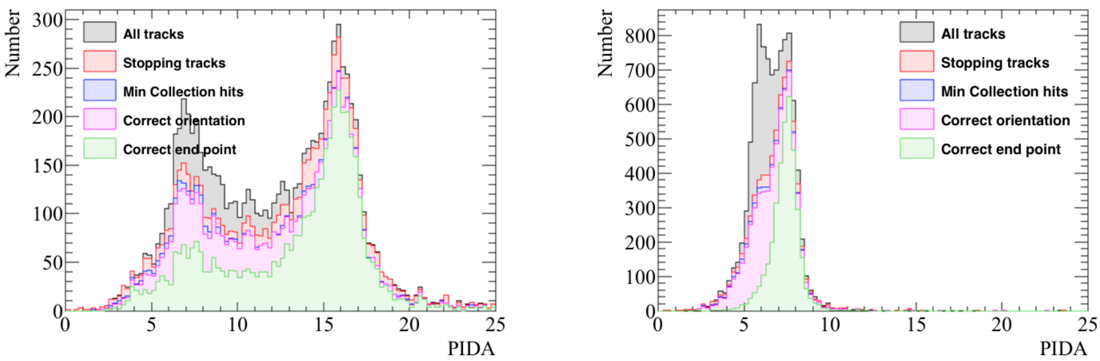

(a) The PIDA values calculated for the single proton sample.

(b) The PIDA values calculated for the single muon sample.

Fig. 5.15 The calculated PIDA values for single muons and protons in the 35 ton. A series of criteria designed to select only tracks due to stopping particles which have a required number of collection plane hits is applied. The tracks are then further refined using truth information such as the true end point of the particle.

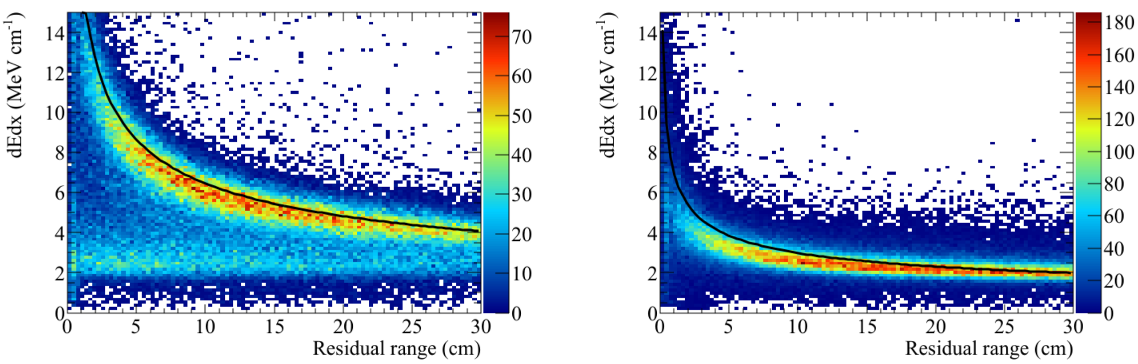

(a) The $\frac{dE}{dx}$ versus residual range plot for the single proton sample.

(b) The $\frac{dE}{dx}$ versus residual range plot for the single muon sample.

Fig. 5.16 The measured relationship between $\frac{dE}{dx}$ and residual range for single muons and protons in the 35 ton. The plots are made after applying all of the cuts outlined in Figure 5.15, meaning that the MIP peaks have been suppressed using truth information.

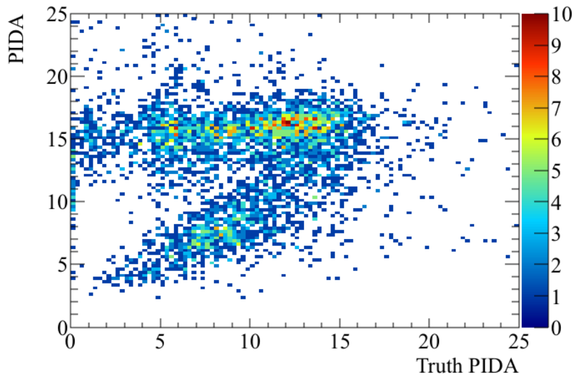

Fig. 5.17 A comparison between PIDA values calculated using truth and reconstructed information

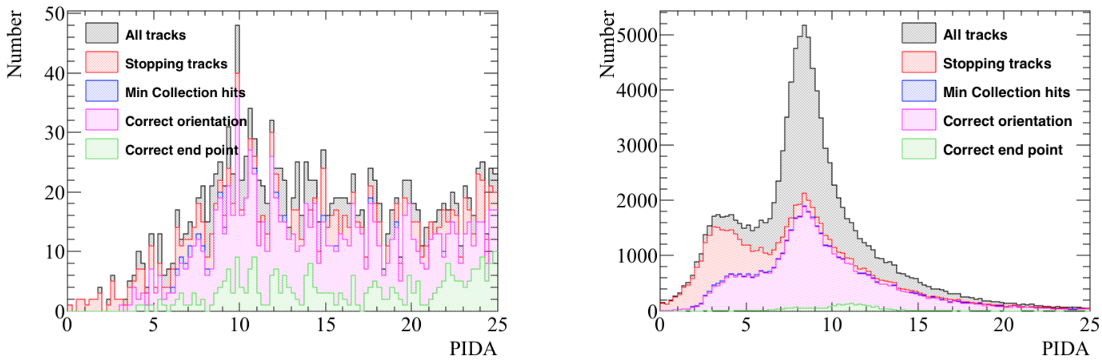

(a) The PIDA values calculated for protons. (b) The PIDA values calculated for muons.

Fig. 5.18 The calculated PIDA values for muons and protons in a CRY sample through the 35 ton. A series of criteria designed to select only tracks due to stopping particles which have a required number of collection plane hits is applied. The tracks are then further refined using truth information such as the true end point of the particle.

Chapter 6

The 35 ton data sample

The data taking period for the 35 ton prototype was from November 2015 until March 2016. This included an extensive commissioning period before the detector was filled with LAr and the electric field was turned on. During this time many of the features of the data discussed below were first noticed and attempts to rectify these were pursued. A long commissioning period was also required because many of the DAQ sub-systems were still under active development in November.

A total of 22 days worth of data was collected with the electric field set at 250 V cm^{-1}, the breakdown of when these periods occurred is shown in Figure 6.1. It is clear that the analysable data is interspersed with data where the electric field was not turned on, this is both due to extenuating circumstances such as a site wide power outage in early March and a dedicated two week noise hunting exercise in February. The physics data taking period ended at 3am on 19th March 2016 when a filtration pump broke causing an unrecoverable loss of purity as air was pumped into the detector. Following this studies to understand the electronics noise and to test the high voltage systems continued but it was deemed too costly to acquire any more physics data. During this time the electric field was raised to the nominal value of 500 V cm^{-1}, and some of the causes of the higher than expected noise levels were discerned.

6.1 Organisation of the data structure

As previously noted the 35 ton consisted of three detector sub-systems: RCEs collecting TPC data, SSPs collecting photon detector data, and CRCs tagging cosmic rays. The DAQ combined these three data streams into synchronous events in time and saved them as LArSoft

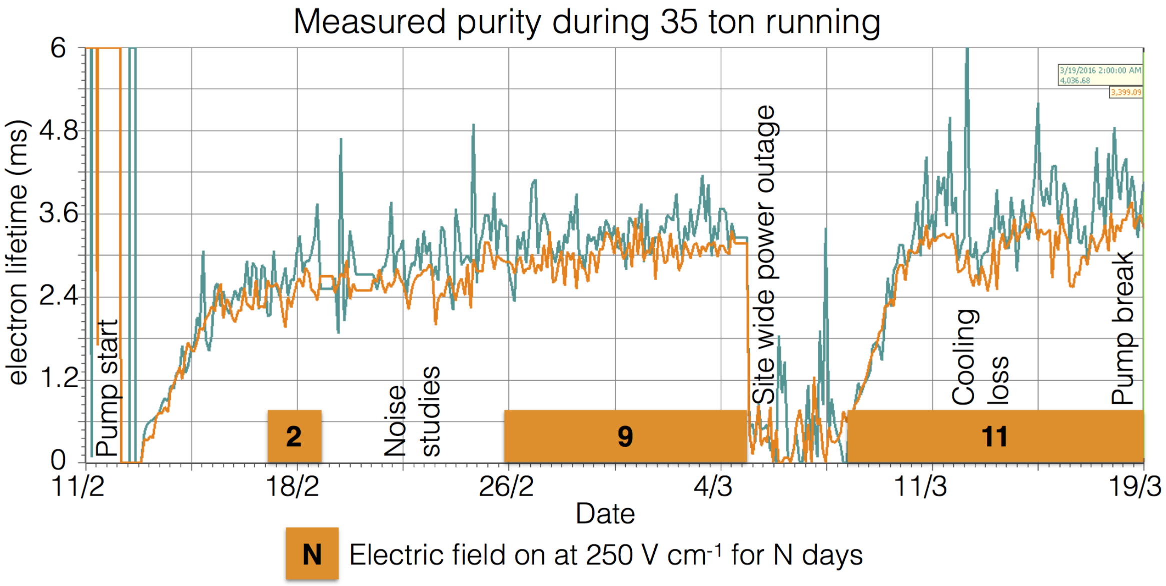

Fig. 6.1 Timeline showing the data collected during the 35 ton Phase II run once the purification pumps were turned on.

data objects. These data objects would later have to be converted to the offline data products which the reconstruction tools developed on simulation used, this is discussed in Section 6.2. This section describes the structure of the data objects in the raw form.

During operations the DAQ was configured to maximise data throughput and physics potential. This meant recording different lengths of times for each of the three sub-systems as the data volumes and length of physics information were significantly different. For example due to the emission of prompt light the physics information from the SSPs is of a much shorter length of time than from the RCEs where data has to be recorded whilst the electrons drift through the LAr. During the running period the recorded data was triggered by through-going muons which produced coincidences on the CRCs on opposites side of the cryostat. A coincidence is defined as two CRC modules recording a hit within 30??? ns. The system used to collect the CRC data was also responsible for generating the triggers and so this meant that the trigger rate could be suppressed to approximately 1 Hz by only producing triggers every N times a coincidence occurred, where N was a tuneable variable. A trigger rate of 1 Hz was used as the maximum speed at which data could be written to disk was approximately 60 MB s^{-1}, which is roughly equal to the size of each triggered event when the entire detector is read-out in the configuration discussed below. The rate at which events were recorded could have been increased if zero-suppression of the TPC data had been used, however the noise level meant that this was not feasible.

With an electric field of 250 V cm^{-1} and a drift of 2.25 m, the drift time for electrons at the long drift CPA was roughly 2.6 ms or 5200 ticks (where 1 tick is 500 ns). It was decided that in order for a track causing a counter coincidence to be separated from other tracks it was necessary to have roughly one drift window both before and after the drift window around the coincidence, meaning that data was recorded for 7.5 ms or 15,000 ticks around each coincidence. Only the prompt light from through-going particles was collected and so only 200 μs of SSP data was recorded for each event. The CRCs produced the least volume of data and so were able to be read out constantly.

As the run mode required accessing buffered data, it had to be discretised inside the components before being sent to the event builders in the DAQ. In the discussion of how this worked, focus will be given on the RCE data where some new terms need to be introduced. The smallest unit of data, called a nanoslice, is the data from one RCE for one tick, where each RCE controls 128 channels meaning that there were a total of 16 RCEs in the 35 ton. A microslice is then made by combining $1000\times N$ nanoslices such that it contains 0.5 ms (1,000 ticks) of data across all channels, where N is the number of RCEs that are recorded in the run. Microslices are then combined to make millislices the length of which was configurable. Once produced these millislices were sent by the DAQ to the event builders to be stored as time synchronous LArSoft data objects.

The time synchronous events produced by the DAQ did not, however, correspond to the physics events, this is because the DAQ was originally designed to produce a continuous data stream. This meant that the DAQ was configured to pad events with headers when a sub-system provided no physics information, such as nanoslices in the case of the RCEs. Removing these padded header objects was a remit of the online to offline converter discussed in Section 6.2. As the length of the millislices was configurable it was chosen to be 10 ms (20,000 ticks) in order to best attempt to fully contain physics events and reduce the need for the online to offline converter to stitch DAQ events together. The padding of millislices with headers between physics events introduced some peculiarities in the data recorded such as millislices containing two parts of non-continuous data as shown in Figure 6.2 where the second millislice has no information for the time between the end of physics event 2 and the start of physics event 3.

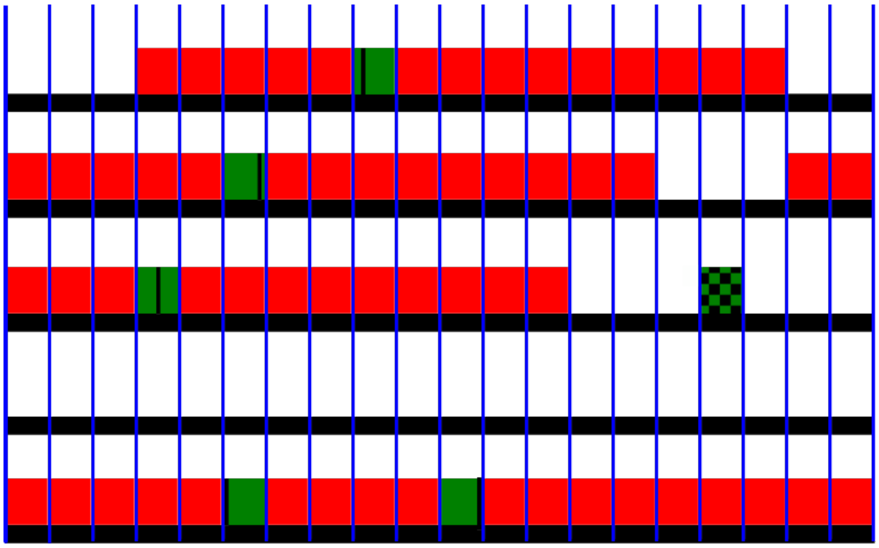

Fig. 6.2 A diagram of possible millislice structures for the TPC data recorded by the 35 ton. Each row represents a millislice, whilst each box represents a microslice. The vertical blue lines delineate each microslice, giving 20 microslices per millislice. Solid red and green boxes represent microslices with TPC data in them. A group of 15 continuous red and green boxes are the recorded “physics events”.Green boxes represent triggers which were used, with the black lines showing the time in the millislice at which the trigger occurred. Green and black patterned boxes represent coincidences of CRCs which were not issued as triggers due to their proximity to a previous coincidence.

During normal data taking the last N microslices are buffered in the RCEs so that if a trigger is issued the previous millislices can be accessed before they are deleted. As the data is buffered in the form of microslices, previous microslices may only be accessed in whole. This means that a whole number of microslices must be loaded before the trigger so, when a trigger is issued part way through a microslice, the previous X microslices are sent to the event builders. As a result during running there are always a minimum number of ticks both before (5,000 ticks) and after the trigger (9,000 ticks) but the exact numbers can change by up to 1,000 ticks for a given event depending on where in a microslice the trigger came. The result of this is that it is impossible to a priori know the number of ticks before/after a given counter coincidence. This is shown in Figure 6.2 where the black lines representing triggers, are seen to occur at different points within the microslices. For example, physics event 1 will have more data after the trigger than physics event 2 as the trigger occurs earlier in the triggered microslice.

6.2 Reformatting the data to the offline structure

Conversion of the data objects stored in the raw data to the data objects used in simulation required a suite of unpacking services to be written, the specifics of which are not discussed here. These all required a common interface through which to access the data and check that the timing of each component was consistent, and then to produce a final LArSoft file for downstream use. This interface had the added role of producing complete physics events, meaning that it had to be able to combine multiple millislices and extract only the data containing the continuous physics events.

The format that the data reformatter followed was that upon unpacking each of the sub-systems, the TPC ticks would be looped through to see if a user defined set of conditions could be satisfied at that time. These conditions were usually whether an East-West or North-South counter coincidence occurred at that time, or if this millislice contained TPC data whilst the previous one did not. The latter was the default configuration as this gave the option of preserving all of the data gathered, for reasons discussed at the end of Section 6.1. Other conditions were available, though rarely used, such as if the SSPs observed a large flash of flight, or if there was a large change in the average TPC ADC value. Once a set of conditions is satisfied a user defined number of pre-condition ticks are gathered. It is set to zero in the case of the previous millislice containing no TPC data as there is no previous data to load which would not have a gap in time, see Figure 6.2. In the case of using a counter coincidence to make an event, a value of 300 pre-condition ticks is normally used, with a maximum of 5000 ticks being able to reliably collected. Once the pre-conditions ticks are gathered a further N post-condition ticks are gathered, where N is defined by the user. Usually 15,000 ticks are gathered when the previous millislice is empty and 5,200 ticks are gathered when there is a coincidence, though a maximum of 9,000 ticks could be reliably gathered. Data from the other components is added to the event if its timestamp is within the timestamps of the first and last ticks in the event when no more TPC data is required or at the end of a millislice if stitching is required. All timestamps are corrected such that the event began at t=0 as the reconstruction assumes this and the timestamp of the start of the event is stored in the event record so that it can be accessed later if required.

At all points in this process it is important to integrate flexibility so that the user can choose the length of events, which sub-systems are in the events and what the conditions are for making events. It was also important for users to be able to run the service on already formatted events as the unpacking services were the major overhead in running the interface. It is also conceivable that users would want to reformat Monte Carlo events so as to centre them around their chosen conditions and so the use of the unpacking was determined by the interface depending on the format of the input file.

6.3 Observations on data quality and noise mitigation

Reformatting the online data to the offline format was an important step in maintaining data quality as subsequently there was no access to the raw data due to the framework of the 35 ton software. Some of the important checks which were performed are outlined in Figure 6.3. If any of these issues were present in a given physics event then it is discarded as the integrity of the data cannot be guaranteed. It was decided that these events would be discarded as non-synchronous events would lead to hits in the detector being at incorrect times and padding empty events with pedestals could mean that tracks seem to disappear and later reappear as they travel through the detector.

Another example of inconsistent events is when the sub-systems are not synchronised with each other. This is normally caused by one of the sub-systems missing a clock increment from the master timing unit due to the data trigger being issued close to an increment from the master unit. This misalignment causes an incorrect time sample being read out and so the data from each sub-system within a millislice is not consistent meaning that it will fail the timestamp check and so won't be added to the event record. To avoid incomplete events these physics events are also discarded when observed.

The electronic noise in the 35 ton was higher than anticipated, with the RMS of the RCE ADC being approximately 30 counts compared to an expected thermal noise of around 2.5 ADC counts. Many sources contributed to this elevated noise, some of which are explained below.

Though not directly affecting the noise issues "stuck ADC codes" were a feature of the data which had to removed. "Stuck ADC codes" were caused by bit level corruption where lowest 6 bits in the ADC became frozen to either `0x0` or `0x3f`. This was observed during the first stages of commissioning and an algorithm to remove them was developed and tested on Monte Carlo [24]. In simulations it was observed that the signal could be recovered with minimal losses, as shown in Figure 6.4 where the blue lines (after removal) are seen to closely match the black lines (before adding stuck codes).

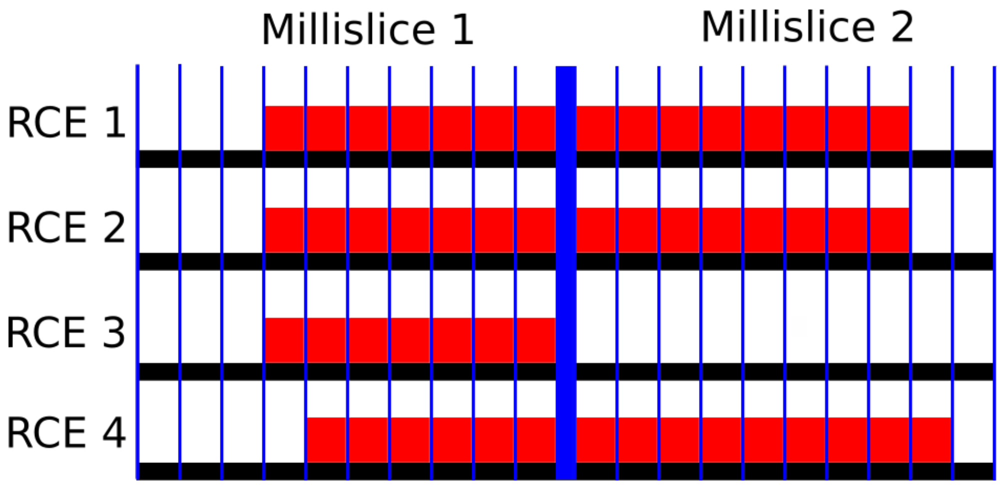

Fig. 6.3 A diagram of TPC microslices within millislices in the 35 ton data stream. Two millislices are shown, each containing 10 microslices. One physics event straddling the millislice boundaries is shown and 4 RCEs representing each row are read out. The vertical blue lines delineate each microslice (0.5 ms, 1,000 ticks), with the thick blue line showing the millislice boundary. Solid red boxes represent micro slices with TPC data in them. It can be seen that RCEs 1 and 2 contain data for the same interval, whilst the data from RCE 3 in millislice 2 has been "Dropped," and the data from RCE 4 is shifted by 1 microslice from RCEs 1 and 2 and is thus "Inconsistent." As a result of these issues this physics event would be discarded as data integrity cannot be guaranteed.

A significant portion of the noise was correlated between groups of 32 channels, where the ADCs would coherently oscillate. To remove these coherent shifts, ADC baselines were calculated for these groups of 32 channels at each tick and then subtracted from the measured ADC values. This was found to be an effective method of removing coherent noise in MicroBooNE [25]. The effect of removing coherent noise is shown in Figure 6.5, where the signal peak becomes much easier to discern after noise removal and a coherent noise peak around tick 6030 is removed. An issue with removing coherent noise in this way is that events which are parallel to the APAs will produce signals at common times across adjacent wires and these signals may be removed along with the coherent noise causing a reduction in the hit reconstruction efficiency. The only way to prevent this is to "protect" potential signal regions from the coherent noise removal, as is done in MicroBooNE [25].

When a Fast Fourier Transform (FFT) [26] is performed on the coherent noise subtracted waveforms, it can be seen that signals occur with specific frequencies. Some of these frequencies are caused by real energy depositions, whilst others are due to the electronics noise. It is possible to remove the noise frequencies by applying Wiener filters [27]. Frequency spectra are taken for each of the three planes and a clear signal is both preserved and suppressed. The

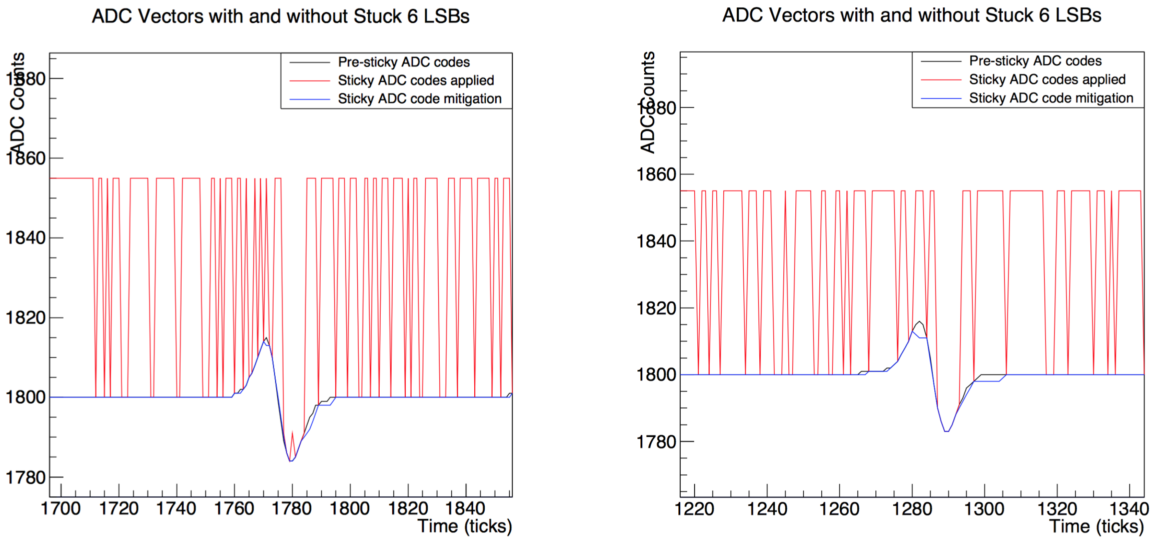

Fig. 6.4 Two Monte Carlo spectra showing the effect of the introduction and removal of stuck bits on a simulated signal. The black line shows the simulated signal on a wire, which is then modified by adding the effects of “stuck ADC codes,” shown by the red line. The “stuck ADC codes” are then removed, and the resulting signal is given by the blue line. It can be seen that the signal loss is minimal after the “stuck ADC codes” are removed. The figures were taken from [24].

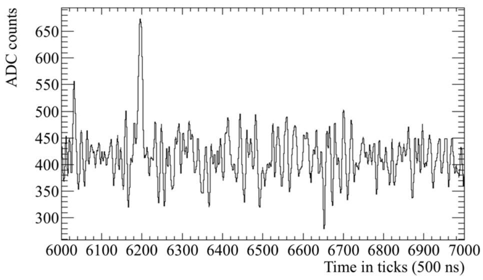

(a) Before coherent noise removal

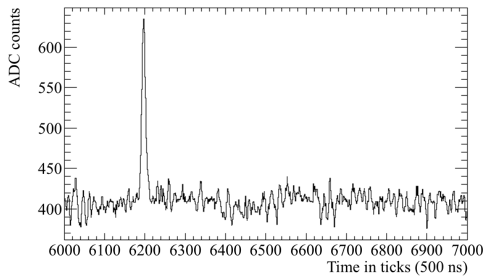

(b) After coherent noise removal

Fig. 6.5 The effect of coherent noise removal on a 35 ton signal event.

raw signal spectra are then divided by the signal suppressed spectra to produce *signal/noise* frequency spaces. The signal regions to be conserved, can then be found by fitting a combination of sigmoid functions to the frequency spaces around regions of high *signal/noise*. A demonstration of how this was applied, is shown in Figure 6.6. It is also possible to remove specific frequencies which are not removed by the filters, this was necessary for a 54 KHz noise component introduced by the fluorescent lights in the detector hall. After the run ended it was found that some of the high frequency noise components were introduced by a short on a warm power cable, the techniques used to find this cable will be used when commissioning future detectors [28].

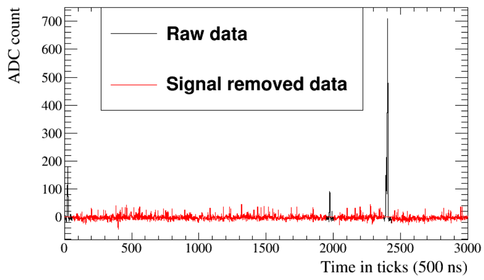

(a) A raw and signal subtracted waveform for a collection plane wire.

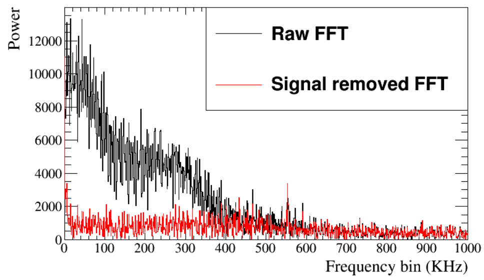

(b) The FFT of the raw and signal subtracted waveform for a collection plane wire.

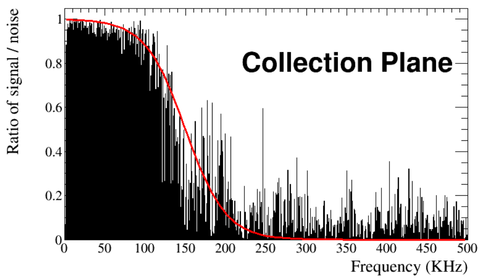

(c) The *signal*/*noise* ratio for a collection plane wire, the red line shows the fraction of frequency power which passes the filter.

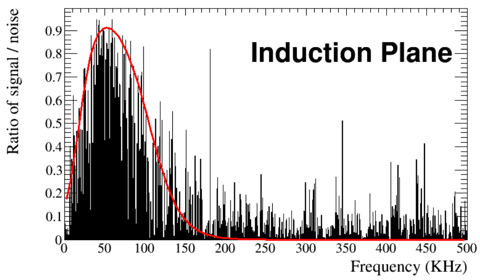

(d) The *signal*/*noise* ratio for an induction plane wire, the red line shows the fraction of frequency power which passes the filter.

Fig. 6.6 The application of Wiener filters to the 35 ton data.

An example of the effect of the noise mitigation steps is shown in Figure 6.7, where the left side shows the raw data and the right side shows the data after the stuck code unsticker, coherent noise removal and Wiener filter algorithms have been applied.

Transitions to a higher noise state associated with strong signals at high frequencies, between 400 and 650 KHz, were observed after cool down. The transitions would occur approximately every 2 hours and were occasionally observed to happen shortly after a saturation event across the whole detector [28]. Once the state was induced the only way to stop it was to power cycle the low voltage supplies. It was found that power cycling APA3 could both stop and induce the higher noise state, importantly this was the only APA with electronics located at the base of the TPC. The data taken during the elevated noise state was unrecoverable as the electronics noise was too large, and so upon the observation of a transition the low voltage supplies were power cycled. It was observed that the transitions occurred much less frequently when APA3 was not powered and so it was not used for

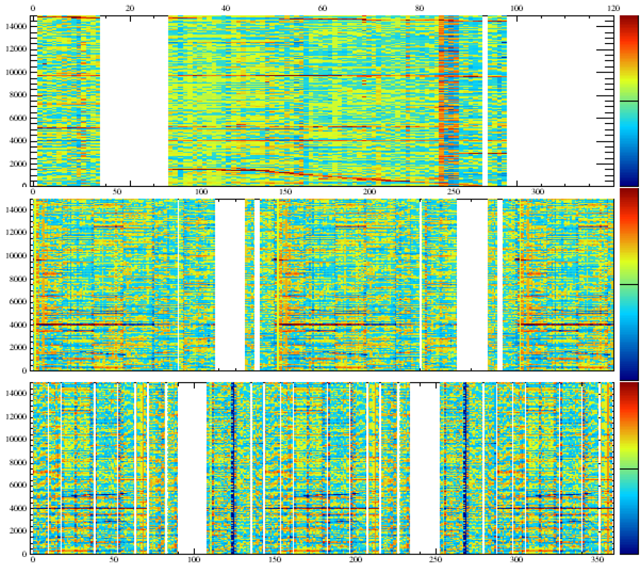

(a) Raw signal before noise removal

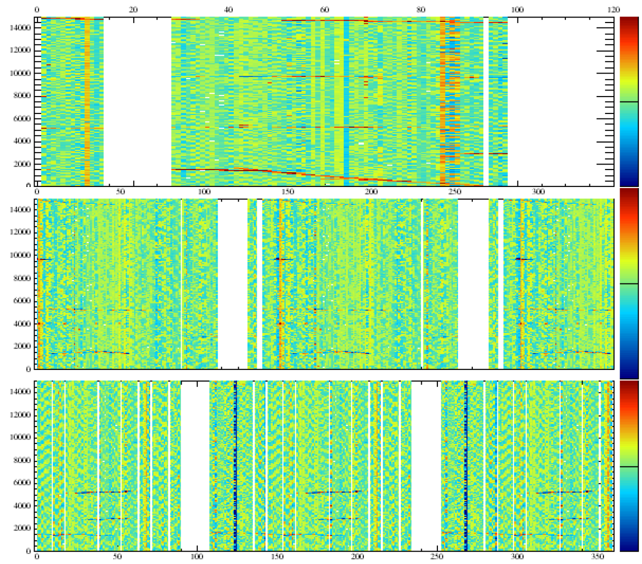

(b) Signal after noise removal

Fig. 6.7 Event displays showing the effect of the noise removal algorithms on data in the 35 ton. The event displays show the signals in the collection, U and V planes respectively. The plots show wire number, time in ticks and charge in ADC counts on the x, y and z axes respectively. The effect of the noise removal algorithms can clearly be seen, as large changes in charge due to the noise are no longer present after they have been applied. The application of the noise removal algorithms does however also remove real signals, as depositions across many channels at the same time which were present before their application can no longer be seen after they are applied.

significant portions of the data taking period. Despite efforts to study the transitions during warm testing they were unable to be induced and have not been observed in other experiments such as MicroBooNE despite using the same low voltage supplies. It is thought that the cause of the transitions is a feedback loop in the low voltage cable which was much longer in the 35 ton than in MicroBooNE, this would explain why APA3 was more susceptible as the cable is routed past its electronics [29].

6.4 Performance of reconstruction algorithms

Following the noise removal outlined above hit and track finding was still more difficult than in simulations due to the still elevated noise level. In order for a sensible number of hits to be reconstructed the hit finding threshold had to be substantially increased in data as compared to Monte Carlo, this meant that many of the low energy hits would not be reconstructed.

A potential solution to not reconstructing the low energy hits is to use the counter positions to select only hits which could have caused coincidences. When determining whether a reconstructed hit could have caused the counter coincidence a two-dimensional window around the counter edges in the yz plane is constructed and timing information is used to extend this to three dimensions. The x position of the hit can be calculated using the hit time and electron drift velocity using Equation 5.1.

Determining whether collection plane hits are within the counter window is trivial as they have a constant z position and either cover the full detector height (tall APAs) or roughly half of the detector height (short APAs). The wrapping of the induction planes, however, means that each wire segment has to be considered individually and that multiple segments of a given wire could lie within the counter shadow. The 3-dimensional volume that is enclosed by connecting the edges of the counters which were hit to cause the counter coincidence, is called the "counter shadow," and the wires which lie within the 2-dimensional projection of this volume onto the yz plane are considered here. Choosing between these potential wire segments is done by iterating through the following steps. If at any point only one segment satisfies the condition then this segment is chosen:

- Does the wire segment intersect any collection plane wires which record hits?
  - This is because when there is a signal on an induction plane there should also be signals on the collection wires.
- Are there adjacent wires which have hits at a similar time?

- This is because one would expect a track to deposit energy on multiple adjacent wire segments.

- Which hit lies closest to the line defined by unique collection plane hits in the xz plane?
  - This is follows identical logic to the first criterion, but selects the hit which best matches the collection plane hits and attempts to remove the effect of noisy collection plane wires by only using wires which have one hit within the counter shadow. This would also hopefully improve the quality of the fit as there will not be numerous outlying hits.
  - This can be changed to consider the line defined by previously selected hits in the given TPC and plane where the hit choices are.

Following a re-optimisation of the clustering algorithms it was observed that the standard reconstruction could achieve track reconstruction to a similar efficiency as the counter shadowing and so the standard reconstruction has been used in the discussions to follow [30]. There has since been an effort to improve the counter shadowing hit disambiguation to remove the outlying collection plane hits using the MLESAC method [31] whereby points which are far away from a best fit are ignored. These studies are still on-going [32].

A symptom of the elevated noise state is that signals are often dropped on one of the induction planes, this means that the tracking algorithms often have to combine clusters in only two of the three planes. Reconstruction using two planes was shown to be effective by the ArgoNeuT collaboration [33] so the loss of signal in one of the three planes is not prohibitive to track reconstruction. Another consequence of the elevated noise level is that even when the counters are used to seed hit finding, the hit finding threshold is too high to reconstruct the very lowest hits. This causes the plot of dQ/dx for muons, shown in Figure 6.8, to look flat due to a cutoff at 100 ADC cm^{-1} below which no hits are found. The inability to reconstruct the lowest energy hits means that calorimetry is all but impossible on the 35 ton dataset even though the tracking algorithms perform relatively well. The inability to perform reliable calorimetry en masse means that the only particles which can be assuredly identified are the muons which triggered the counter coincidences, making the analysis proposed in Section 5.4 extremely difficult, if not impossible.

The muons in the triggered sample will all traverse the detector but their orientations can be carefully selected by the user, for example one could easily select a sample of muons which cross the APAs at increasing angles, or are parallel to the wire planes at increasing drift distances by matching through-going muons with counter coincidences. The process

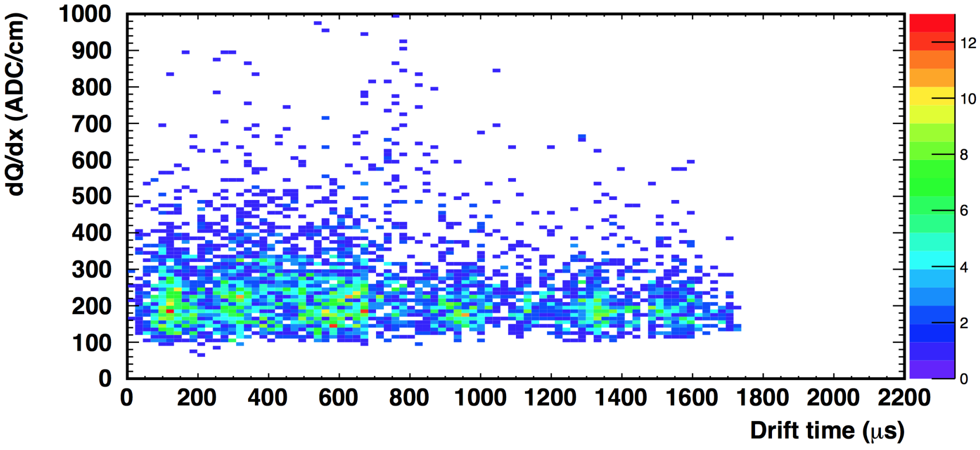

Fig. 6.8 The dQ/dx values for a sample of muon collection plane hits, note the cutoff at 100 ADC cm^{-1} due to the hit finding threshold. Figure taken from[34].

by which this is done is identical for both North-South and East-West coincidences, though more focus will be given to the later and so it will be presented in that regard. The same matching technique would also have been applied to vertical muons had the telescope triggered been utilised. For a reference as to the location of the counter positions around the cryostat see Figure 3.2, and for a representation of only the East-West counters see Figure 6.9.

It is possible to construct a line in the yz plane joining the centres of the two counters which were hit when a coincidence occurred, shown by the dashed line in Figure 6.9. This can then be compared with the trajectory of a track in the yz plane and a dot product of the two vectors calculated. A reconstructed track is assigned to a given counter coincidence if the dot product of the track and the coincidence is more than 0.98 and the hit times are consistent with the x positions of the counters. The results of the dot product calculation are shown in Figure 6.10. Matching only tracks which are well aligned with a counter coincidence should produce a pure sample of tracks, as parallel muons are unlikely to be highly correlated in time and any tracks reconstructed from the noise will have random directions. This is shown in data where if multiple tracks pass the dot product cut they are co-linear and are not randomly orientated, as shown in Figure 6.11.

By matching tracks in this way it is possible to evaluate the reconstruction efficiencies for these muons at increasing drift distances and track angles. If multiple tracks are aligned with the coincidence and are within the expected time region then their track lengths are summed when calculating reconstruction efficiencies as it is expected that the track was split by a region of the detector either being turned off or too noisy to reliably reconstruct a

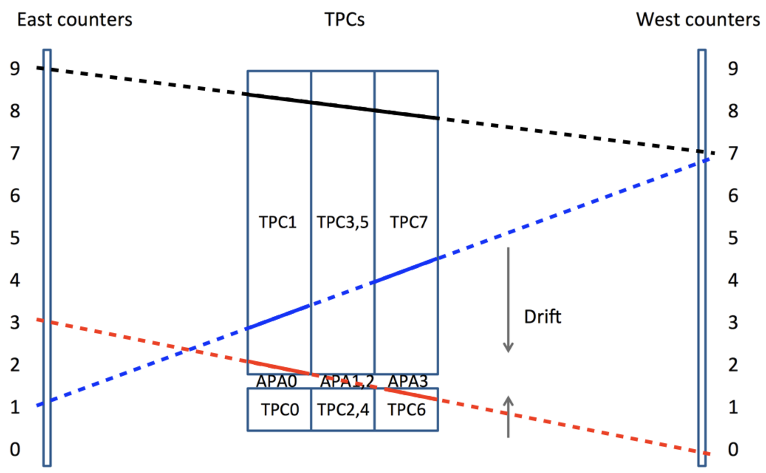

Fig. 6.9 The numbering scheme for the East - West counters in the 35 ton. The counters have been numbered from 0 to 10 depending on their position from the end of the short drift volume. This is different to the LArSoft numbering scheme shown in Figure 3.2 where they go from 6-15 and 28-37 for the East and West counters respectively. Three muons which would have caused coincidence triggers are shown as dashed lines, and the reconstructed tracks they produced are shown as solid lines. The red track would be an APA crossing event, and produced tracks in TPCs 1 and 6. The black muon was fully reconstructed as one continuous track, however the blue particle was not reconstructed in the middle TPCs and so was reconstructed as two separate tracks.

track. If these tracks have a combined track length of more than 50 cm then the coincidence is identified as having been successfully reconstructed. This threshold is much lower than the true track length which should be reconstructed, >150 cm, but few particles are fully reconstructed in the data and so a compromise is made to achieve a large enough sample of tracks upon which analyses can be performed. A reconstructed track that is 50 cm long is likely to have a large number of hits on collection plane wires that are not noisy, and it is these hits which are required when calculating purity or measuring the effect of diffusion as discussed in Section 6.5. A track with length more than 50 cm is also likely to have been stitched between TPCs due to the geometry of the 35 ton and track trajectories. The demonstration of stitching tracks between TPCs was a design goal of the 35 ton, and so identifying tracks where this was achieved satisfies that goal.

An important concept that must be introduced before these reconstruction efficiencies can be described is that of a "counter difference." The "counter difference" of a coincidence and it's associated tracks is defined as the absolute difference between the counter numbers

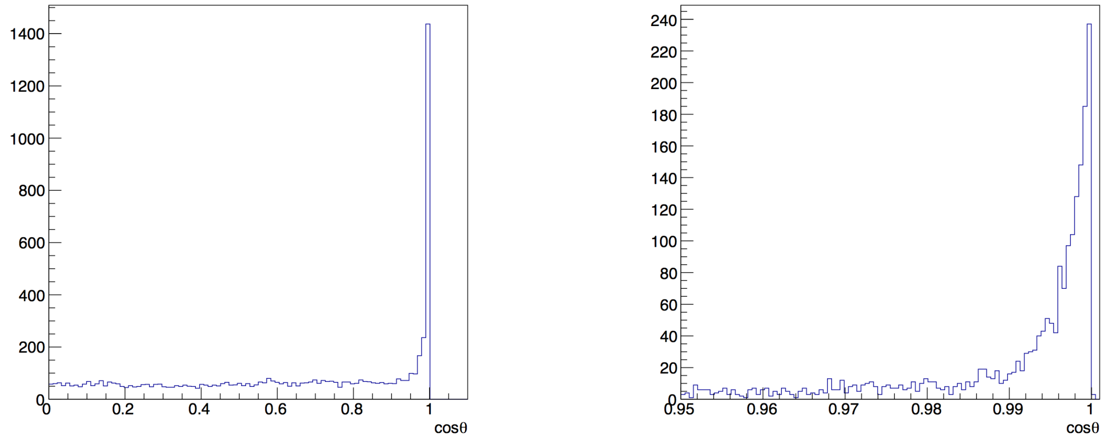

(a) All dot product values.

(b) Dot product values close to 1.

Fig. 6.10 The dot product of the track and vector joining the centres of the coincidence counters in the yz plane. A threshold value of 0.98 is required for a track to be considered to be due to the counter coincidence. It can be seen that many tracks are well aligned with counter coincidences, having dot products of more than 0.99.

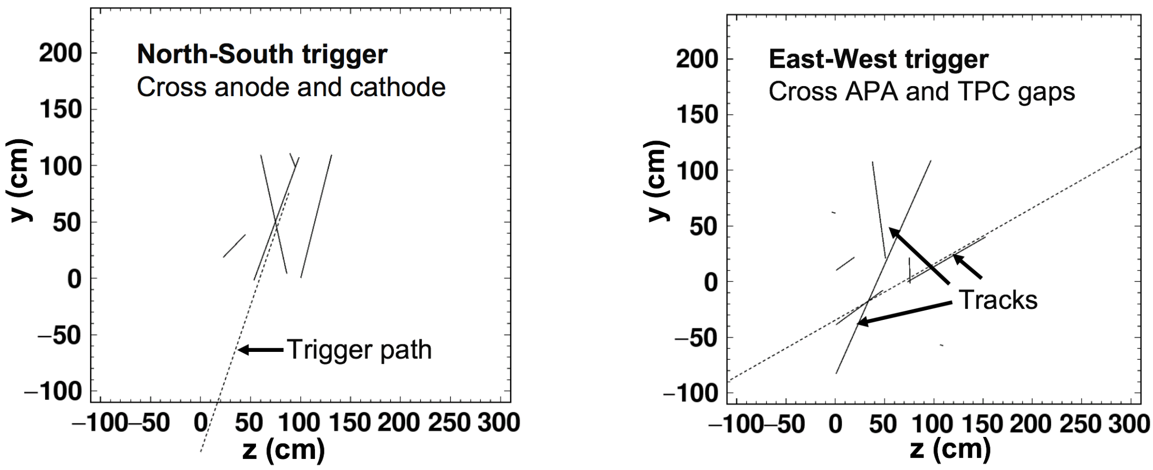

(a) A North-South counter coincidence.

(b) An East-West counter coincidence.

Fig. 6.11 The alignment of reconstructed tracks with the vectors joining the centres of the coincidence counters. The dashed lines show the vectors joining the centres of counters hit in the coincidence, whilst the solid lines show the reconstructed tracks. Figures taken from [30].

of the East and West counters that were hit, as shown in Figure 6.10. As such, the “counter differences” of the coincidences shown in Figure 6.10 are 2, 3 and 6 for the black, red and blue coincidences respectively. Given the orientation of the counters, the rarest counter difference will be 9, as only particles which hit counters (E_0 and W_9) and (E_9 and W_0) will

Table 6.1 The angles relative to the APAs corresponding to given counter differences. Though the East and West counters have a width in the y (vertical) direction, this is much less than their extent in the z direction. The depth of the counters, their extent in x is negligible compared to the separation of the East-West counters. The counters have identical widths in both the y and z directions. The angles are calculated using the difference in the centres of the counters in the z direction divided by the separation of the East and West counters in z.

Absolute counter difference	Approximate angle (°)
0	0 ± 2.1
1	4.2 ± 2.1
2	8.4 ± 2.0
3	12.5 ± 2.0
4	16.5 ± 2.0
5	20.3 ± 1.9
6	23.9 ± 1.8
7	27.3 ± 1.7
8	30.7 ± 1.6
9	33.5 ± 1.5

have a counter difference of 9. In contrast to this, the most common value for the counter difference is 1, as there are many possible combinations of East and West counters being hit to give this counter difference. In the discussions below "counter difference" is occasionally referred to as "delta counter" or "Δ counter." The approximate angles which tracks with given counter differences have relative to the APA frames is shown in Table 6.1.

Figure 6.12 shows a range of reconstruction efficiency plots for combinations of different counter differences and different drift distances. As the counter coincidences with large counter differences will have large variations in drift positions, the drift distance plotted here is the average x position of the counter centres that were hit. For example, if the two counters that produced the coincidence are at 10 cm and 230 cm respectively, then the drift distance plotted would be 120 cm. This distance is called the "coincidence centre" in the following discussion. It should be noted that only coincidences which would produce tracks that are contained within the long drift volume are considered here, hence there being no negative x positions.

From Figure 6.12a it is evident that the reconstruction efficiency for tracks with shallow angles relative to the APAs is extremely poor, with the efficiency for tracks aligned with counter differences of 0 or 1 never rising above 10%. This is due to the coherent noise removal where hits which are correlated in time will be removed as they will be perceived as being noise as opposed to real signals. As the difference in counter number increases the efficiency is seen to increase, though the rate of this increase is seen to depend on the "coincidence centre". The effect of increasing "coincidence centre" can be seen more clearly in Figure 6.12b where the efficiency for each counter difference as a function of "coincidence centre" is plotted. Here it can be seen that the reconstruction efficiency decreases for coincidences that are centred further away from the APAs. This is due to the fact that when an energy deposition has further to drift, it will induce a smaller pulse on the wires meaning that it is more likely to be below the hit threshold. Figure 6.12c combines Figures 6.12a and 6.12b to show how the reconstruction efficiency for increasing "coincidence centre" changes with increasing counter difference. It can be seen that tracks with counter differences of between 3 and 5 where the "coincidence centre" is between 60 cm and 140 cm away from the APAs are the best reconstructed coincidences. Finally, Figure 6.12d shows how the frequency of coincidences of a given counter difference occurs compared to how many events contain reconstructed tracks which are aligned with the coincidence. It can be seen that as stated earlier, the most common counter difference is 1, with the least common being a counter difference of 9. However, given the low reconstruction efficiency seen for the lowest counter differences few tracks are reconstructed. This means that when considering the reconstructed tracks, most are due to coincidences with counter differences of either 3, 4 or 5.

6.5 Measuring interaction times using electron diffusion

As electrons drift from the interaction point to the wire planes they become spread out in both time and space, this effect is known as diffusion and is an important property of electron transport in LAr which must be well understood. The mechanism by which diffusion occurs in LAr was first discussed by Atrazhev-Timoshkin [35], and has since been developed to consist of a complete set of measurements for electric fields between 100 and 2000 V cm^{-1} [36]. The diffusion of electrons is rarely isotropic and so the component that is transverse to the drift field and the component that is parallel to the drift field are normally measured separately. Diffusion parallel to the drift field is called longitudinal diffusion and is generally smaller than the component of diffusion that is transverse to the drift field. Figure 6.13 shows how diffusion can smear the electrons collected on a set of wires when the electrons are initially highly correlated in time and space.

Longitudinal diffusion has the effect of spreading the drifting electrons out in time causing signals to become wider in time and smaller in height as the total charge is conserved.

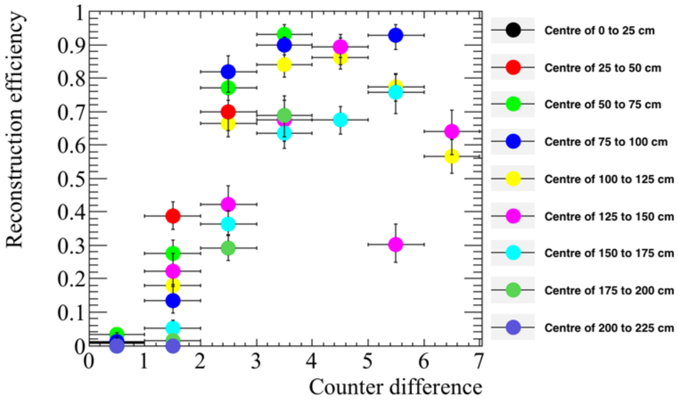

(a) The reconstruction efficiency as a function of counter difference for different coincidence centres.

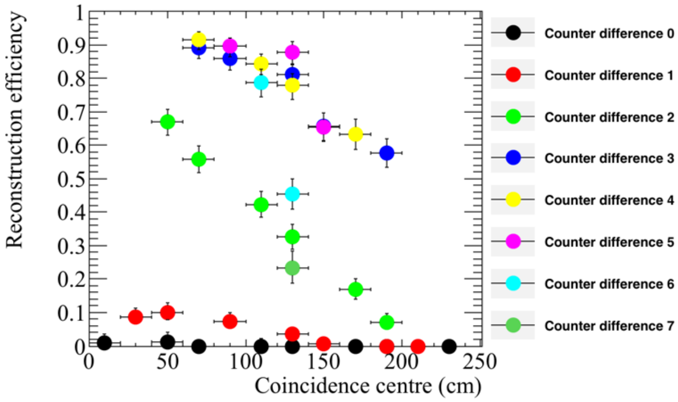

(b) The reconstruction efficiency as a function of coincidence centres for different counter differences.

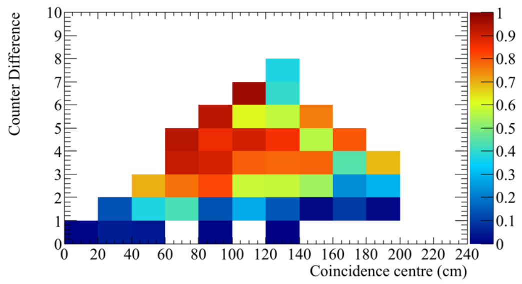

(c) How the reconstruction efficiency changes for increasing coincidence centres and counter differences.

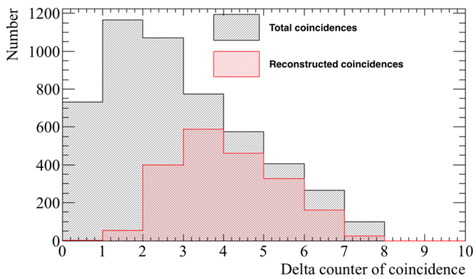

(d) The number of events for each counter difference that were recorded in the data and the number of those which were successfully reconstructed.

Fig. 6.12 The reconstruction efficiencies for coincidences that trigger an East-West coincidence in the 35 ton data over a 2 day running period.

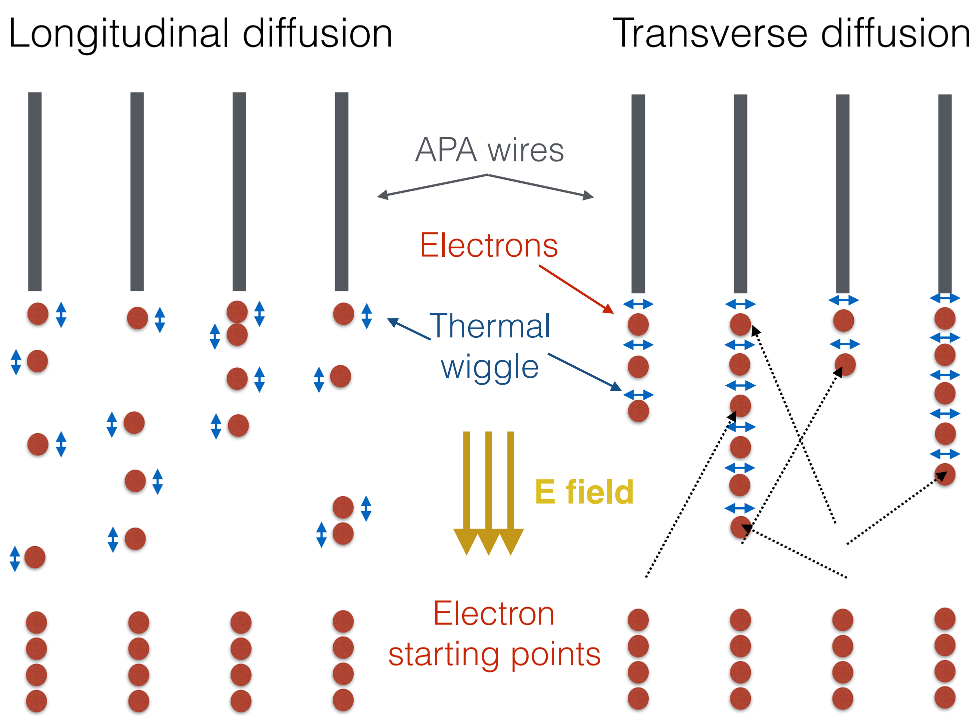

Fig. 6.13 A schematic showing the longitudinal diffusion (left) and transverse diffusion (right) of electrons. In both cases four electrons are initially shown below four wires, and are allowed to diffuse in either the drift direction or perpendicular to the drift direction in the longitudinal and transverse cases respectively. It can be seen that the effect of the diffusion is to make the electrons spread out in time in the case of longitudinal diffusion and to spread out in space in the case of transverse diffusion. Figure taken from [37].

The increasing hit width can be measured for increasing drift times (distances) provided the hits do not fall below a hit finding threshold. Transverse diffusion causes drifting electrons to spread out in space, changing the amount of charge deposited on a wire and reducing the charge resolution of the detector. Transverse diffusion is measured by discerning how the width of the hit charge distribution changes for increasing drift distances [36].

Through-going particles make ideal tracks to study diffusion as they are minimally ionising and so have roughly constant energy depositions along their tracks. The tracks they produce can also cover a wide range of drift distances if they are not parallel to the APAs. The drift distances of hits within a track can be determined by matching the track with a counter coincidence as discussed at the end of Section 6.4 and then correcting the x co-ordinates of the hits using the result of Equation 5.2 in Equation 5.1.

Traditionally the only way to determine an interaction time for a track is to match it to either an external calibration source such as whether it aligns with an external counter coincidence, or to match it to a flash of scintillation light as in Section 5.1. These techniques are particularly crucial for neutrino detectors on the Earths surface such as MicroBooNE where each neutrino interaction usually has a background of at least one cosmic muon. The reconstructed tracks from this muon background has to be distinguished from those due to the neutrino interaction in order correctly assign a scintillation flash to the reconstructed tracks. An example of an event that has many scintillation flashes and cosmic muons which need to be correctly associated, is shown in Figure 6.14. However, it may be possible that the change in hit width due to diffusion as a particle travels through the detector, could be used to determine the interaction time; though this has not been attempted before. To study whether this is possible, the effects of diffusion would have to be measured for a sample of tracks with known interaction times and orientations.

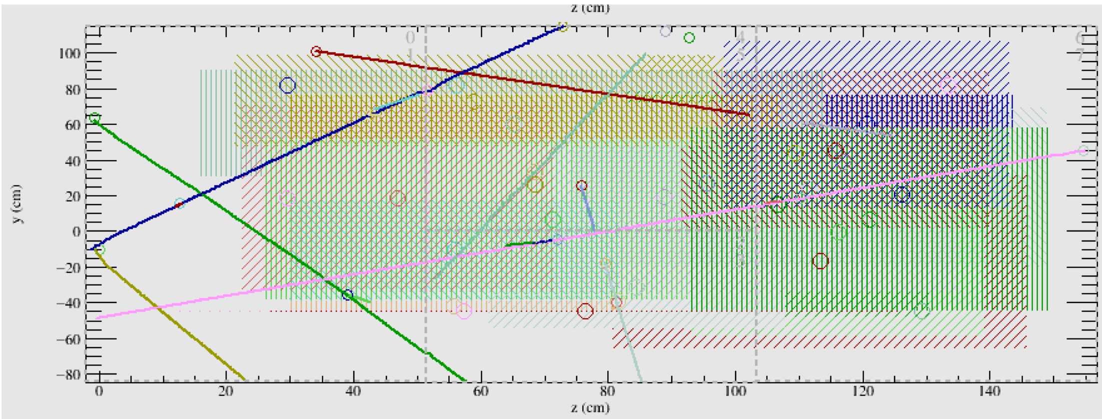

Fig. 6.14 A simulated event display showing multiple tracks and flashes to be assigned to each other in the 35 ton. The coloured lines represent reconstructed tracks, whilst the coloured dashed boxes represent flashes.

The 35 ton dataset is ideal for testing this hypothesis as the counters are able to provide a sample of tracks with known angles and interaction times which can be used to tune interaction time determination metrics. These metrics can then be applied to another sample of tracks where the interaction time is known but not used so that the accuracy of the calculated interaction times can be found. As longitudinal diffusion is the dominant effect that increases the hit width, transverse diffusion will not be directly considered further. However, as noted in Section 6.4, the noise level in the 35 ton data causes reconstruction issues and so it is also useful to compare the method against a low noise detector. Monte Carlo can provide this sample, and this comparison is shown in Section 6.5.2. It is also useful to observe the effects that different detector conditions such as, the electric field, the electron lifetime, noise level and rate of diffusion have on the method. This is shown in Section 6.5.3. First though, the method is performed on the 35 ton dataset.

6.5.1 Determining interaction times in 35 ton data

When calculating the determination metrics, only hits on wires which are not noisy want to be considered. This is because wires with a high level of correlated noise observe hits with a wider RMS. This is shown in Figure 6.15, where, when a baseline noise of 10 ADC counts is added to a simulated hit with a peak value of 50 ADC counts and an RMS of 10 ticks, the width increases by over 10%. Hits with delta rays also need to be removed as the deposited energy will be larger and over a longer period of time than hits from the main track, this will make the RMS of the individual hit wider and also increase the width of the charge distribution for the track. To remove these hits only hits which satisfy the following cuts are used:

- No hit on the same wire within 50 ticks of the hit in question - removes delta rays.
- No more than 10 hits on the same wire in the whole 15,000 tick data sample - removes clearly noisy wires.

These cuts will clearly become much more restrictive as the noise level in the detector increases, but they are essential in order to collect a dataset which is not overpowered by noise. Only collection plane hits are used, as the charge resolution is better and the signals are unipolar as opposed to bipolar meaning that a Gaussian function can be easily fitted to the signals. Additionally the $signal/noise$ ratio on the collection planes was much higher than on the induction planes for the 35 ton dataset and so the hits could be much more reliably reconstructed.

Diffusion is a track angle dependent property and so track angle ranges have to be considered independently. To minimise the number of figures presented, only graphs made for tracks which have a counter difference of 4 are shown, though the procedure is identical for tracks of all counter differences. Tracks with a counter difference of 4 were chosen as they were one of the angles for which tracks were well recosntructed in the data, see Figure 6.12. The tracks are considered en masse, and so the hits for every track are separated into 10 cm regions of increasing drift distance from the APAs. The following quantities are calculated for each 10 cm drift region:

- The hit *RMS* - the most direct way to measure transverse diffusion.

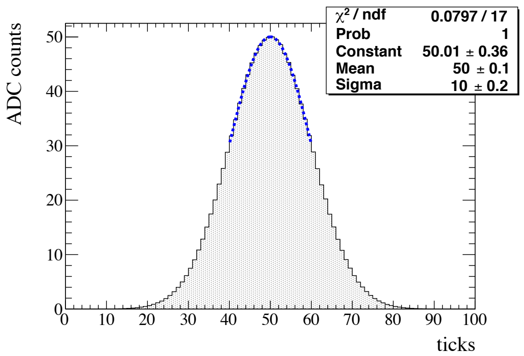

(a) A simulated signal.

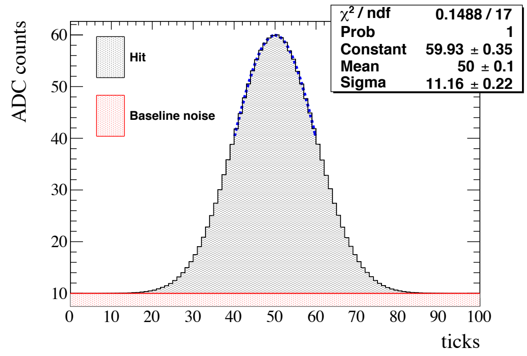

(b) A simulated signal with a constant noise baseline added.

Fig. 6.15 A simulated signal with a width of 10 ticks and an amplitude of 50 ADC counts, both before and after a constant noise baseline, of 10 ADC counts, is added. In reality the noise would fluctuate with time. When a Gaussian function is fitted to each signal, it is seen to be more than 10% larger for the signal where the noise baseline is added. This shows that noise can cause the measured width of a hit to increase. Figure taken from [37].

- The hit $RMS/Charge$ - an attempt to incorporate the effect of impurities in the LAr for relatively low purity data which will have a drift distance dependence.
  - The charge of a hit is calculated by integrating the ADCs of the reconstructed hit over time.

Fitting Gaussian functions around the peaks of the distributions will yield the most probable values for the drift regions, as is shown in Figure 6.16.

The drift distance effect of diffusion can then be observed by fitting these most probable values as drift distance increases. This drift distance dependence is shown in Figure 6.17 for tracks that are associated with a coincidence which had a counter difference of 4. The angular dependence can then be shown by observing how the most probable fit value at a drift distance of 0 cm changes for increasing angles, this is shown in Figure 6.18. A drift distance dependence can clearly be seen in the data as the most probable hit RMS is seen to increase for hits which originate further from the APAs. It also clear that there is an angular dependence on the hit width as the most probable hit widths next to the APAs is seen to rise for tracks associated with coincidences with large counter differences. These dependencies show that, when considering a large sample, diffusion can be separated into distance and angular dependant dependencies, however whether this can be observed for individual tracks has not yet been considered.

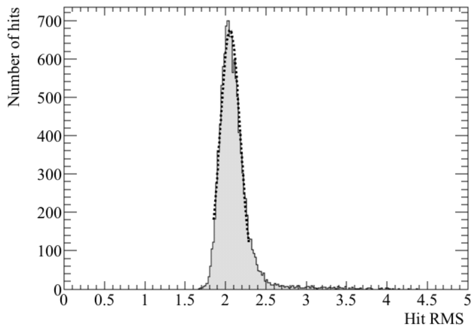

(a) The most probable hit *RMS* value for hits between $x = 20$ cm and $x = 30$ cm.

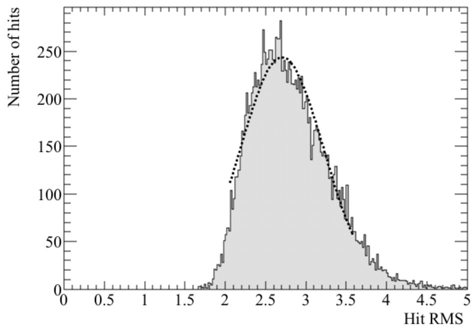

(b) The most probable hit *RMS* value for hits between $x = 140$ cm and $x = 150$ cm.

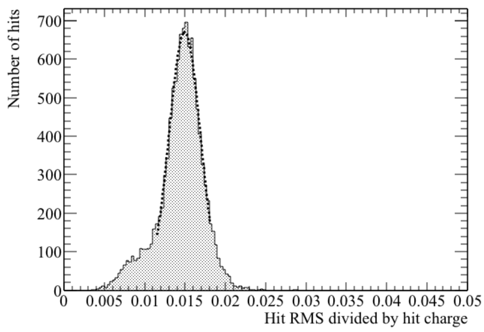

(c) The most probable hit $RMS/Charge$ value for hits between $x = 20$ cm and $x = 30$ cm.

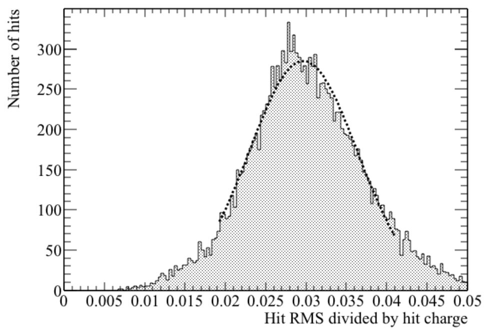

(d) The most probable hit $RMS/Charge$ value for hits between $x = 140$ cm and $x = 150$ cm.

Fig. 6.16 Distribtuions of the most probable values of *RMS* of the hits (top) and $RMS/Charge$ of the hits (bottom), for points between 20 and 30 cm from the APAs (left) and points between 140 and 150 cm from the APAs (right), for tracks associated with a coincidences that have counter differences of 4.

To consider single tracks, the best line fits for the counter differences for a large sample of tracks, such as in Figure 6.17, need to be used to predict the position you would expect a hit to originate from given a value for its hit *RMS* and the angle of the track to which it belongs. The predicted positions can then be compared to the known position from the counter coincidence to determine the accuracy of the prediction. As the distributions shown in Figure 6.16 are roughly symmetric around the most probable value one would naively expect that if a track has a sufficient number of hits then the distribution of RMS values for those hits would match that found over a large sample. If this were to be the case then the difference in reconstructed and predicted hit times should be peaked around the track interaction time.

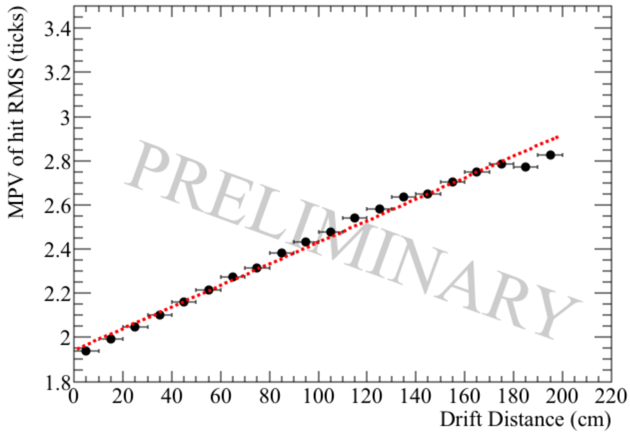

Fig. 6.17 The most probable values of hit *RMS* as a function of drift distance, for tracks associated with a coincidence that had a counter difference of 4.

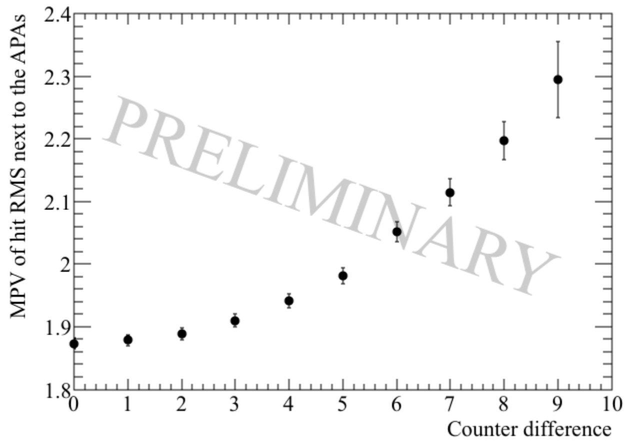

Fig. 6.18 The most probable values of hit *RMS* within 10 cm of the APAs, as a function of the counter difference of the coincidence, that the track was associated with.

An intrinsic assumption in this method is that the track has a large number of collection plane hits that do not contain delta rays and are on wires which would not be identified as noisy. The tracks being considered will have crossed all z values in the detector meaning that a total of 336 collection hits could potentially be reconstructed. Given the reconstruction problems in the 35 ton detector, very few tracks will have hits on all of these collection wires. However, requiring at least 100 collection plane hits is not unreasonable and would correspond to a reconstructed track length of at least 50 cm. The difference between the predicted and reconstructed hit time for each hit is shown in Figure 6.19 for both the hit *RMS* and hit *RMS*/*Charge* metrics.

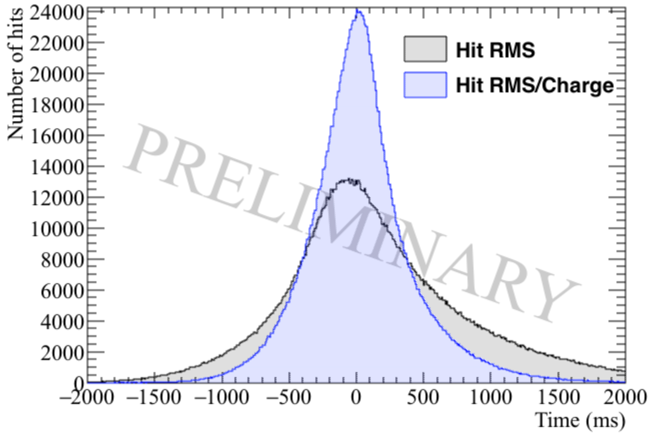

Fig. 6.19 The difference between the predicted and reconstructed hit times in the 35 ton dataset. The differences in time when the hit *RMS* metric is used are shown in black, whilst the differences in time when the hit *RMS*/*Charge* metric is used are shown in blue.

It can be seen from Figure 6.19, that in the 35 ton dataset both distributions are centred around a time difference of 0 μs which is encouraging as it shows that the method has potential. The width of the distribution for the *RMS*/*Charge* metric is smaller, and the peak larger, so it is expected that this will provide the more robust metric. This is because these features show that the hit times which are predicted, are more likely to be close to the reconstructed hit times. The peaks are centred around a time difference of 0 as the hit times had previously had the measured interaction time, from the counter coincidence, subtracted from them. This was done so as to avoid the uncertainty which would arise from allowing the coincidences to remain at random times between ticks 5000 and 6000, see the discussion concerning Figure 6.2 for an explanation as to why this occurs.

When evaluating interaction times the average difference in reconstructed and predicted hit times across every hit on the track must be considered. This is shown in Figures 6.20 and 6.21, where, as expected from Figure 6.19, the *RMS*/*Charge* metric provides a better estimation of the interaction time. The reason for this is that by utilising the charge information due to losses from impurities this metric gains an extra handle on the drift distance and hence the reconstructed time of the hits. The losses due to impurities are difficult to measure in high-purity LAr environments as the decrease in collected charge with increasing drift distances is small [38]. The effect of increasing LAr purity is shown in Section 6.5.3. Using the change in hit charge in the 35 ton may have a drawback though, because, as shown in

Figure 6.8, there is a threshold effect for hits with large drift times. However, as the same threshold effect is present in all 35 ton data samples the limitation it introduces is mainly in the efficiency with which ’good’ collection plane hits will be reconstructed and so this information can be confidently used.

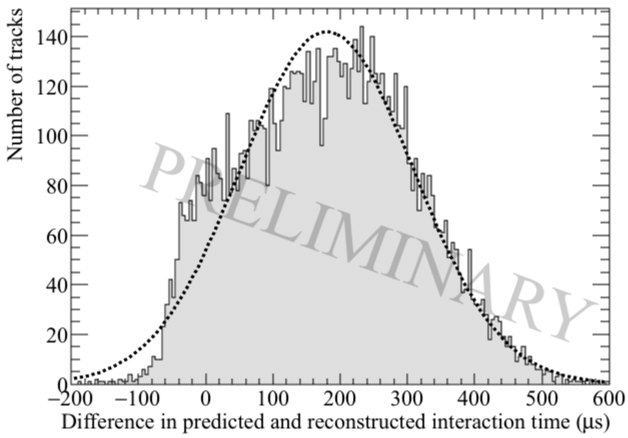

(a) The average difference in interaction times using the hit *RMS* metric.

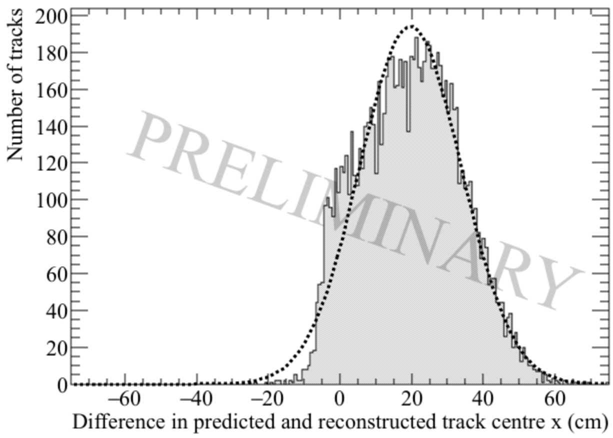

(b) The average difference in the central *x* position of a track using the hit *RMS* metric.

Fig. 6.20 The accuracy of the hit *RMS* method in the 35 ton dataset.

Figure 6.20 shows that using the effects of diffusion, and the hit *RMS*, the interaction time and central *x* position of a track can be reliably predicted in the 35 ton dataset. The accuracy in determing the interaction time is found to be 298 μs, where the distrbitution has a FWHM of 267 μs. When this is converted into the difference in central *x* position of the track the accuracy is found to be 32.2 cm with a FWHM of 28.8 cm.

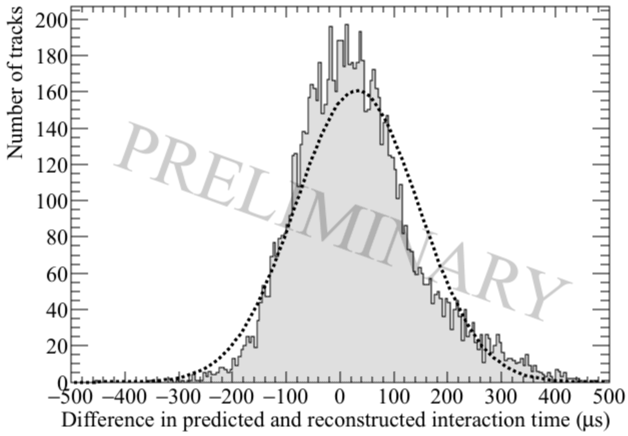

(a) The average difference in interaction times using the hit *RMS/Charge* metric.

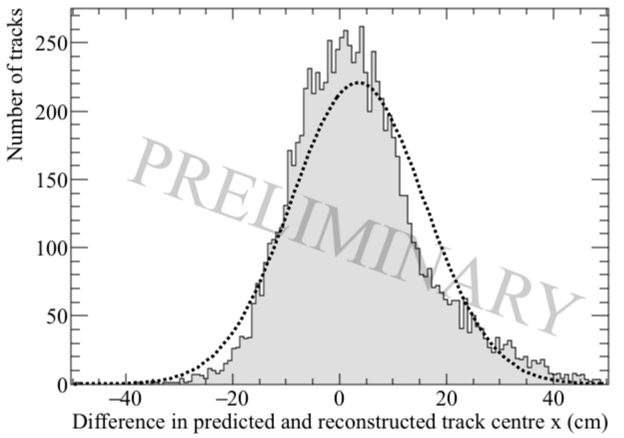

(b) The average difference in the central *x* position of a track using the hit *RMS/Charge* metric.

Fig. 6.21 The accuracy of the hit *RMS/Charge* method in the 35 ton dataset.

Figure 6.21 shows that using the effects of diffusion, and the hit *RMS/Charge*, the interaction time and central *x* position of a track can be reliably predicted in the 35 ton dataset. The accuracy in determing the interaction time is found to be 55.3 μs, where the distrbitution has a FWHM of 212 μs. When this is converted into the difference in central *x* position of the track the accuracy is found to be 6.88 cm with a FWHM of 23.1 cm.

The resolutions found are quite impressive as given that the total drift time for electrons through the whole 35 ton detector volume of 250 cm is roughly 5200 ticks, it means that tracks can be distinguished throughout the detector volume. As discussed earlier, the issues with noise in the 35 ton dataset affect the accuracy with which tracking and calorimetry can be performed, and so it is reasonable to expect that the effectiveness of the interaction time determination was also affected. Therefore, it is purdent to repeat the study on a Monte Carlo dataset where the detector noise is much lower. This is presented in Section 6.5.2.

6.5.2 Determining interaction times in a low-noise detector using Monte Carlo, and differences with data

When determining interaction times in Monte Carlo simulations, exactly the same criteria are applied to the hits, as δ-rays would still change the measured hit width and will be present in any sample. In a low noise detector it is expected that few wires would be removed due to being noisy but for consistency there is no danger in applying this cut. Imposing a minimum number of collection plane hits is again important to ensure that the distribution of predicted hit times is centred on the interaction time. In addition to the same criteria being imposed on which wires are used, the same metrics are calculated. In all plots shown below the Monte Carlo dataset has been normalised to the size of the 35 ton dataset.

Figure 6.22 shows both the hit *RMS* and hit $RMS/Charge$ distributions for hits that are 100 cm away from the APAs and are from tracks assoicated with a coincidence that has a counter difference of 4. It can be seen that the distributions from the Monte Carlo simulation are tighter than those from the 35 ton data and are also peaked at a lower values of hit *RMS*. This is likely due to the fact that the coherent noise baseline seen in data can increase the width of hits as shown in Figure 6.15 and a higher noise state will affect how well individual hits can be reconstructed. In addition, the most probable values of hit *RMS* at increasing drift distance are shown in Figure 6.23 where the Monte Carlo simulation is again shown with the values from the data. The most probable value of hit *RMS* at a drift distance of 0 cm for a range of counter differences is also shown in Figure 6.24. As was seen when considering the distributions at specific distances and counter differences, the most probable values of hit *RMS* in the Monte Carlo simulation is systematically lower than in the data due to the elevated noise level seen in the data. Another difference between the Monte Carlo and the data is that the gradient of the most probable values of hit *RMS* in data is roughly half of that in the Monte Carlo, this could be due to an overestimation of longitudinal diffusion in the

Monte Carlo.

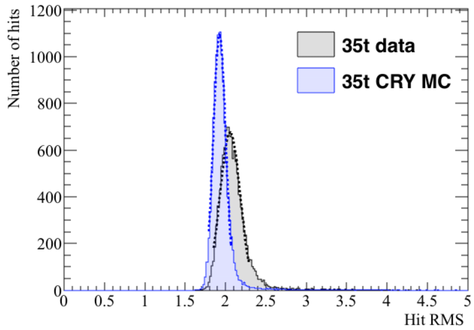

(a) The most probable hit *RMS* values for hits between $x = 20$ cm and $x = 30$ cm.

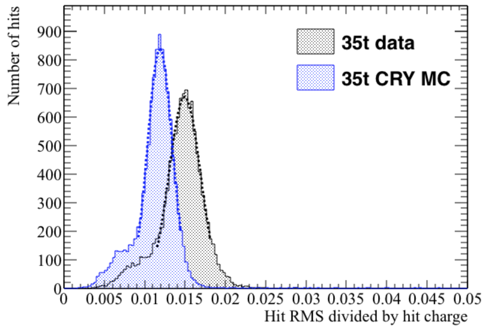

(b) The most probably hit $RMS/Charge$ values for hits between $x = 20$ cm and $x = 30$ cm.

Fig. 6.22 The most probable values of the hit *RMS* and hit $RMS/Charge$ distributions for hits between $x = 20$ cm and $x = 30$ cm, for tracks with a counter difference of 4. The distributions from the 35 ton dataset are shown in black, whilst the distributions from the Monte Carlo simulation are shown in blue.

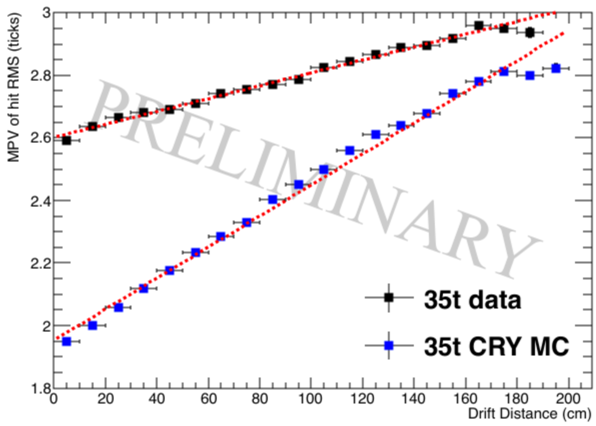

Fig. 6.23 The most probable values of hit *RMS* as a function of drift distance, for tracks associated with a coincidence that had a counter difference of 4. The distributions from the 35 ton dataset are shown in black, whilst the distribution for the Monte Carlo simulation is shown in blue.

Upon calculating the fit metrics in the low-noise Monte Carlo dataset it is then possible to use these to predict track interaction times, this is shown in Figures 6.25 and 6.25. Figure 6.25 compares how reliably the interaction time and central x position of a track can be predicted,

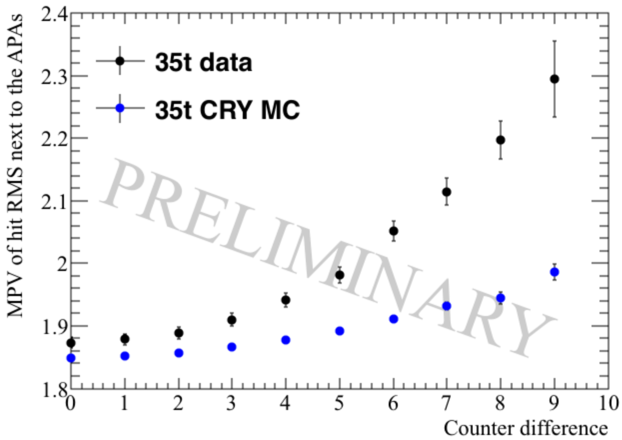

Fig. 6.24 The most probable values of hit *RMS* within 10 cm of the APAs, as a function of the counter difference of the coincidence, that the track was associated with. The distributions from the 35 ton dataset are shown in black, whilst the distribution for the Monte Carlo simulation is shown in blue.

using the effect that diffusion has on the hit *RMS*, in the 35 ton dataset and a low-noise Monte Carlo sample. The accuracy in determing the interaction time in Monte Carlo (data) is found to be 168 (298) μs, where the distrbitution has a FWHM of 127 (267) μs. When this is converted into the difference in central x position of the track the accuracy is found to be 19.4 (32.2) cm with a FWHM of 14.0 (28.8) cm. Figure 6.25 compares how reliably the interaction time and central x position of a track can be predicted, using the effect that diffusion has on the hit $RMS/Charge$, in the 35 ton dataset and a low-noise Monte Carlo sample. The accuracy in determing the interaction time in Monte Carlo (data) is found to be -40.9 (55.3) μs, where the distrbitution has a FWHM of 110 (212) μs. When this is converted into the difference in central x position of the track the accuracy is found to be -3.5 (6.88) cm with a FWHM of 12.1 (23.1) cm.

The hit $RMS/Charge$ metric appears to be able to more accurately predict interaction times, as was seen in when considering the 35 ton dataset. This is again due to the ability to incorporate information about loses due to impurities which increase with drift distance. Also, as expected from the previous figures and the lower noise state in the Monte Carlo it is seen that the interaction times predicted in the Monte Carlo more closely match the true interaction times than in the data. An important feature to observe is that, as well as more accurately predicting the interaction times, the widths of the distributions in Monte Carlo are less than half of that in the data. This means that the resolution with which tracks can be distinguished in the Monte Carlo sample is much better than in the 35 ton dataset, again this

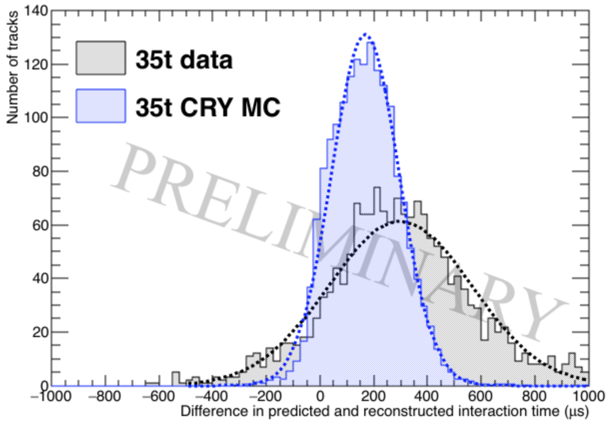

(a) The average difference in interaction times using the hit *RMS* metric.

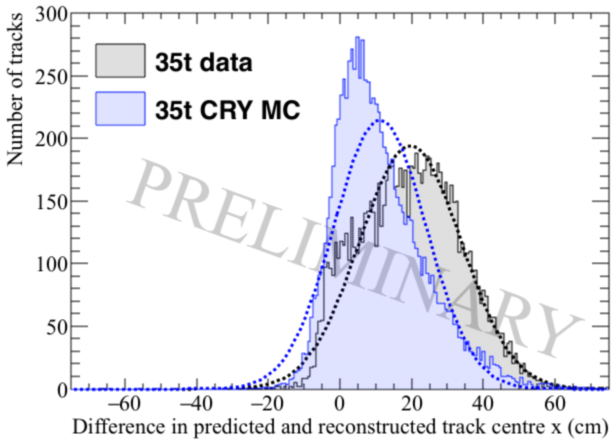

(b) The average difference in the central x position of a track using the hit *RMS* metric.

Fig. 6.25 The accuracy of the hit *RMS* method in the 35 ton dataset and a Monte Carlo simulation. The distributions from the 35 ton dataset are shown in black, whilst the distribution for the Monte Carlo simulation is shown in blue

is attributed to the lower noise level in the Monte Carlo.

The calculation of interaction times is clearly much better in the low-noise Monte Carlo than in the 35 ton dataset, however, the distributions are still not centred around 0 implying that there is a systematic error in the method which has not been removed when considering a low-noise environment. Looking at Figure 6.22 the impact of δ-rays can still be seen where the hit *RMS* plot still has quite a significant tail above the most probable value. This will cause the predicted interaction times to be skewed towards larger times as the hits

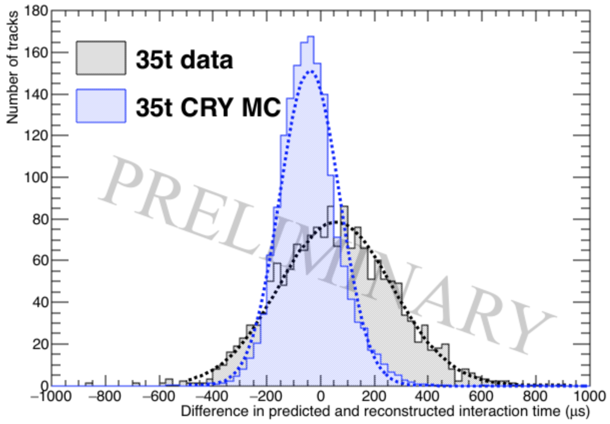

(a) The average difference in interaction times using the hit *RMS/Charge* metric.

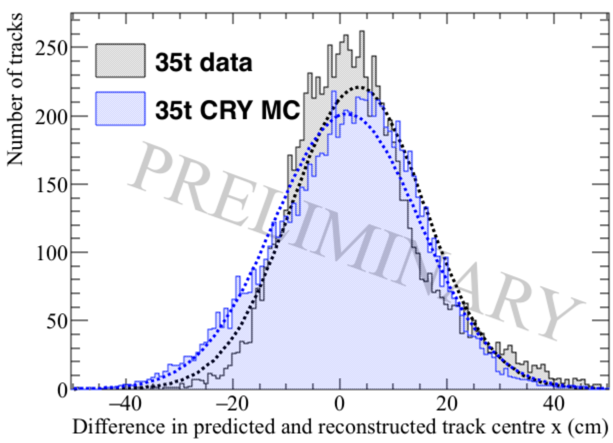

(b) The average difference in the central x position of a track using the hit *RMS/Charge* metric.

Fig. 6.26 The accuracy of the hit *RMS/Charge* method in the 35 ton dataset and a Monte Carlo simulation. The distributions from the 35 ton dataset are shown in black, whilst the distribution for the Monte Carlo simulation is shown in blue

containing δ-rays will be wider and so appear to come at later times than they actually do. Hits containing undistinguishable δ-rays are difficult to remove without looking for slight dips in the raw signals caused by the δ-ray beginning to separate from the main track. This would be almost impossible in the 35 ton dataset given the oscillatory nature of the noise. Δ-rays can also offer an explanation for the *RMS/Charge* plot underestimating interaction time as hits containing δ-rays would deposit more charge and this increased charge would likely be larger than the increased width, causing the *RMS/Charge* to decrease. This is seen in Figure 6.22 where both the data and Monte Carlo samples have tails at small values of hit *RMS*/*Charge*, this decrease in hit *RMS*/*Charge* would lead to an underestimation of the interaction time. The 35 ton dataset as a whole overestimates the interaction time though, and this is due to the tail at large values of hit *RMS*/*Charge* seen in the 35 ton dataset. It is thought that the collection of hits with large values of hit *RMS*/*Charge* is correlated with the noise level in the detector, as it is not seen in the lower noise Monte Carlo sample.

6.5.3 Discerning the impact of changing detector properties using Monte Carlo samples

The difficulty of the reconstruction and analysis of the 35 ton data is due to the elevated noise level. We are now going to verify this statement with a study whereby the noise level in a Monte Carlo sample is changed from the low-noise state used in the previous section, to a level more similar to that which is seen in the 35 ton dataset. If the claim that the noise level made reconstruction difficult is correct, then the the accuracy with which the interaction time can be determined, should be seen to anti-correlate with the noise level of the simualted detector. This study and the ones which follow have all been performed using the same muons, so as to ensure that the only difference between the different samples are the detector conditions, and only one detector condition is varied at a time. As such, there is one sample that is consistent to all samples, which is where the RMS of the noise is 2.5 ADCs, the electron lifetime is 3 ms, the electric field is 500 V cm^{-1} and the coefficient of longitudinal diffusion is 6.2×10^{9}. When presenting the studies with changing detector conditions, the analagous figures presented in the previous section are repeated so as to show how the critical aspects of the methodology are affected.

Figures 6.29 and 6.30 show the accuracy to which the interaction time and central x position of a track can be determined using the effect that diffusion has on the hit *RMS* and hit *RMS*/*Charge* as the changing electronics noise level respectively. Figures 6.29 and 6.30 both show that the integrity of the fits decrease with increasing noise levels, but they show this in very different ways which is very interesting. As discussed in Section 6.3, the 35 ton data had significant amounts of coherent noise which was not expected and so had been previously simulated. As this level of coherent noise is not expected in future detectors, coherent noise has not been simulated in these increased noise level samples. Instead, the electronics noise, or 'thermal noise,' has been varied. The lowest noise level was the design noise level for the 35 ton and is what is used in the 'baseline' sample in the plots to follow. This level of thermal noise is very minimal, and so only noise levels which are more than this have been simualted as the *signal*/*noise* ratio which one gets with such a low ADC RMS is large, and so a decrease in this noise level is unlikely to make a significant difference in the accuracy of the method. However, as can be seen in the 35 ton data and the following plots, increasing the noise level has serious consequences.

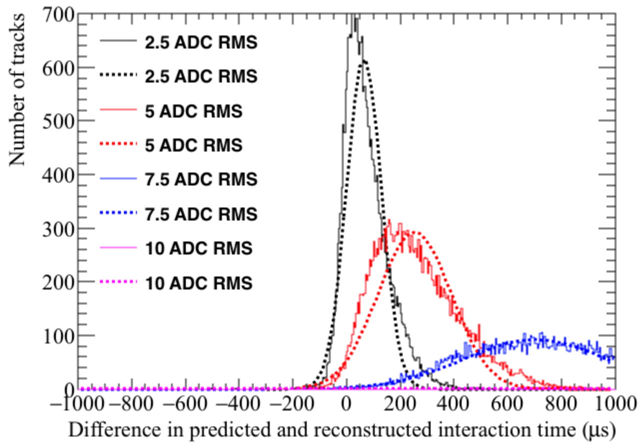

(a) The average difference in interaction times using the hit *RMS* metric.

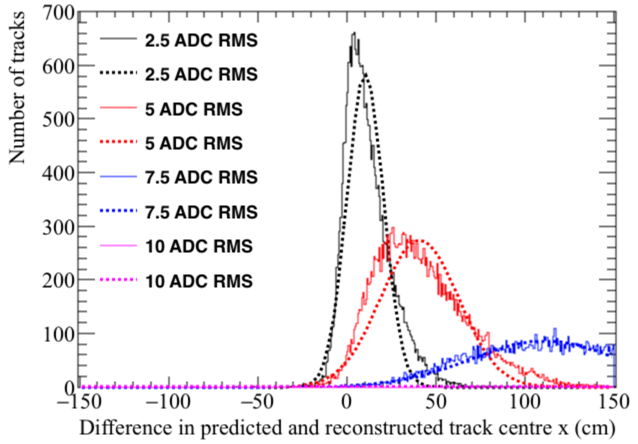

(b) The average difference in the central x position of a track using the hit *RMS* metric.

Fig. 6.27 The accuracy of the hit *RMS* method, for different electronic noise levels.

A key factor that has to be considered here when comparing the following plots to those that are from data, is that, no noise mitigation algorithms have been applied to the increased noise samples. Instead, the threshold that the hit finder uses has been increased to the level that was neccessary for a reasonable number of hits to be reconstructed. Here, a reasonable

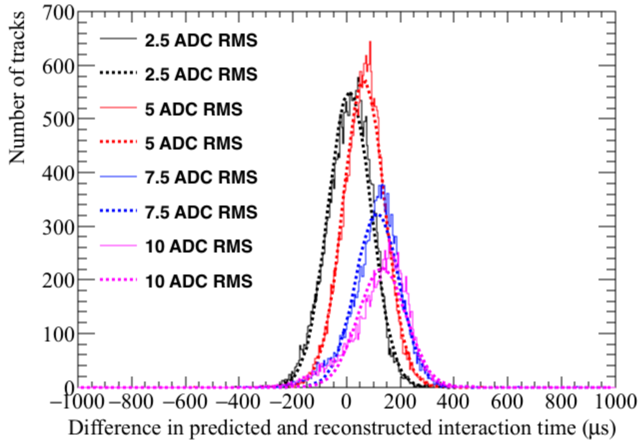

(a) The average difference in interaction times using the hit *RMS*/*Charge* metric.

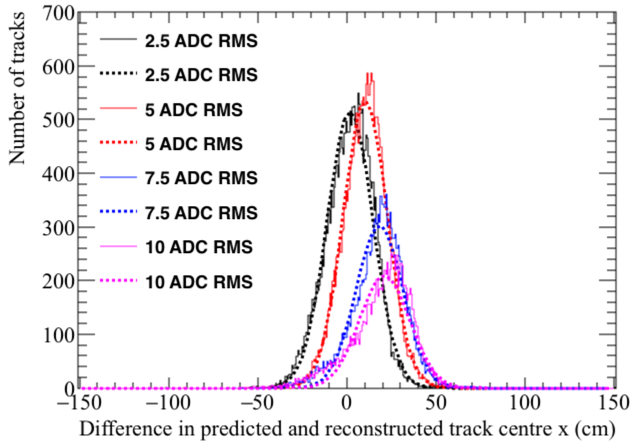

(b) The average difference in the central x position of a track using the hit *RMS*/*Charge* metric.

Fig. 6.28 The accuracy of the hit *RMS*/*Charge* method, for different electronic noise levels.

number of hits simply means, not reconstructing such a large number of noise pulses that they outwiegh the number of true signals from tracks. The hit threshold which was required was determined by looking at the deconvoluted signal and choosing a threshold which was above the majority of the noise signals. The hit threshold used for each level are summarised below:

- Noise level of 2.5 ADC RMS - hit threshold of 6 ADC
- Noise level of 5 ADC RMS - hit threshold of 10 ADC
- Noise level of 7.5 ADC RMS - hit threshold of 15 ADC

- Noise level of 10 ADC RMS - hit threshold of 20 ADC

This means that the main effect of increasing the noise level is to remove the low charge hits, as the will fall below threshold as it increases due to the noise level.

Firstly, considering Figure 6.29, it can be seen that the accuracy to which interaction times can be determined rapidly decreases as the noise level increases. In the case of the highest noise level considered here, the fits used to make the prediction metrics do not converge for counter differences of 1, 2, 3 and 4 as the MPV of hit *RMS* is not seen to increase for increasing drift distances. For evidence of this, see the Figures in Appendix A. Though this is the extreme case, it can be seen that the validity of the hit *RMS* for increasing drift distances becomes less predictable as the noise is increased. The result of this is a less accurate prediction metric, which leads to the large offsets and widths of the distributions that are shown in Figure 6.29.

The most striking feature of Figure 6.30 is the decrease in statistics seen for the increasing noise levels. This shows the effect that increasing the noise level and hence hit threshold has as fewer tracks in total are reconstructed, and those that do are less likely to meet the criteria about the number of collection hits required to make predictions. It is however interesting to note that the centre of the distributions moves closer to the true interaction time as the noise increases. Supposing that two groups of hits from the same point have the same hit *RMS*, but one group deposits significantly more charge than the other, then removing the hits with the lower charge will cause the number of hits in the hit *RMS* plot to decrease, but the shape of the distribution will be unchaged. However, removing the hits with lower charge will siginificantly change the $RMS/Charge$ distribution, as the tail which they cause will no longer be there. The result of this is that more of the hits used to make predictions are within the peak of the distribution, and so the prediction should become more accurate. The reduction in hit and track reconstruction which this entails is not justified when performing whole-scale reconstruction, however, only using hits with a minimum charge could prove beneficial when making predictions.

Figures 6.29 and 6.30 show the accuracy to which the interaction time and central x position of a track can be determined using the effect that diffusion has on the hit *RMS* and hit $RMS/Charge$ for changing electron lifetimes respectively. Figure 6.29 shows that with an electron lifetime of 1 ms, the hit *RMS* metric is very inaccurate, this is likely due to hits which are a large distance away from the APAs being very difficult to reconstruct due to the extremely poor lifetime. For this reason, the accuracy to which the hit *RMS* metric predicts the interaction time improves as the electron lifetime increases, though this increase in small between the 3 ms, 5 ms and 8 ms samples. Figure 6.30 shows the opposite effect, the accuracy to which the interaction time can be determined decreases with increasing electron lifetime for the hit *RMS*/*Charge* metric. This is because the decrease in hit charge is much greater when the electron lifetime is lower. This dependence is the corner stone of this metric, which is why it performs so well for low electron lifetimes, and so the decrease in its accuracy is an unavoidable consequence of increasing electron lifetime.

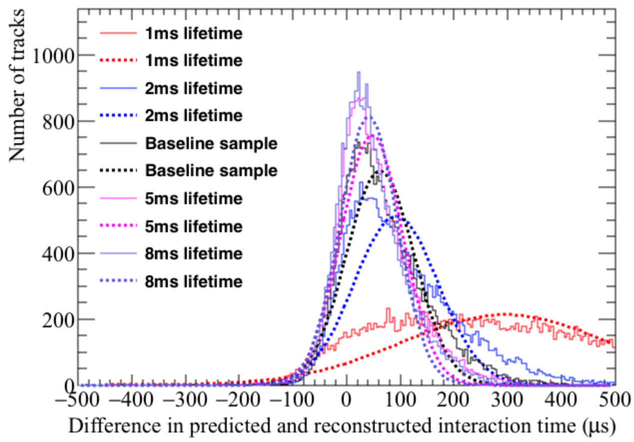

(a) The average difference in interaction times using the hit *RMS* metric.

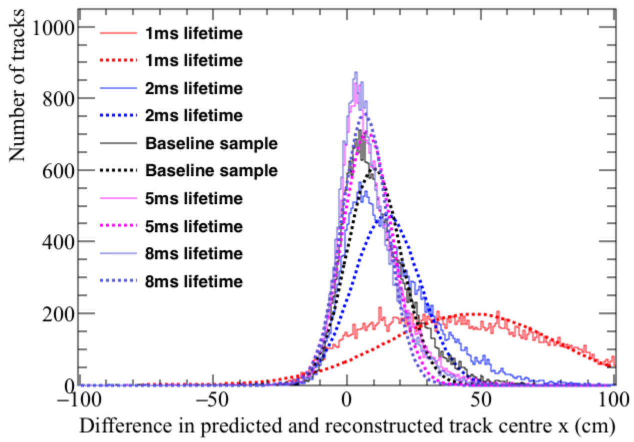

(b) The average difference in the central x position of a track using the hit *RMS* metric.

Fig. 6.29 The accuracy of the hit *RMS* method, for changing values of the electron lifetime.

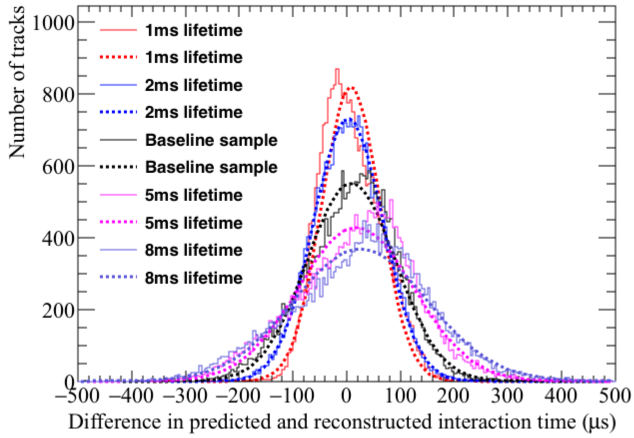

(a) The average difference in interaction times using the hit *RMS*/*Charge* metric.

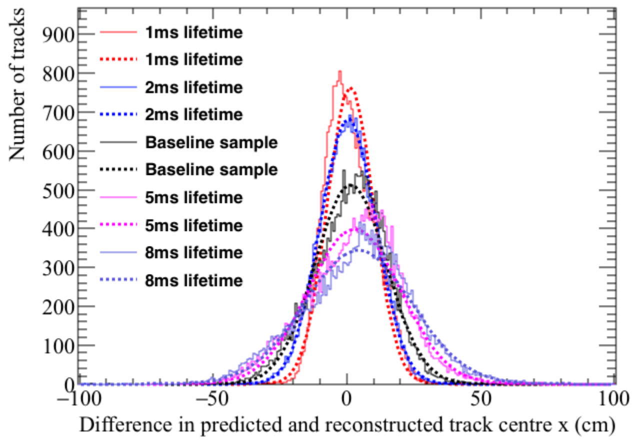

(b) The average difference in the central x position of a track using the hit *RMS*/*Charge* metric.

Fig. 6.30 The accuracy of the hit *RMS*/*Charge* method, for changing values of the electron lifetime.

Figures 6.31 and 6.32 show the accuracy to which the interaction time and central x position of a track can be determined using the effect that diffusion has on the hit *RMS* and hit *RMS*/*Charge* for changing electric field values respectively. Figures 6.31a and **??** show that the accuracy to which the interaction time can be determined is relatively unaffected by the electric field for both the hit *RMS* and hit *RMS*/*Charge* methods. However, when these interaction times are used to predict the central x position the larger drift velocity in the higher electric field samples causes the accuracy to decrease. This decrease in accuracy is because within the same time period electrons will have drifted further in a higher drift field, meaning that the same error in time will produce a larger x offset when compared a lower electric field. The increased field also causes the distributions of the difference in predicted and reconstructed central x position to become wider, particularly in Figure 6.32b, again this is due to the increase drift velocity as the widths of Figure 6.32a are consistent.

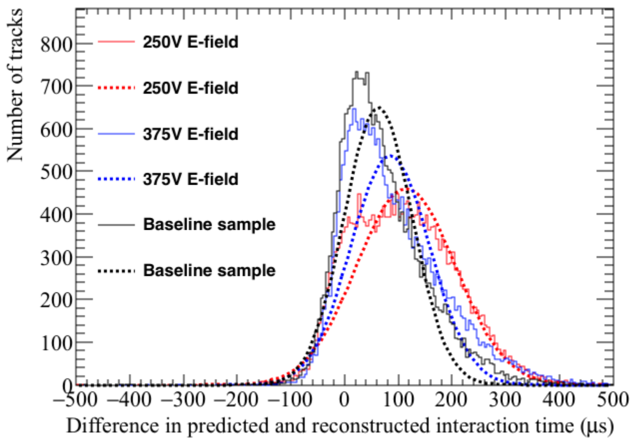

(a) The average difference in interaction times using the hit *RMS* metric.

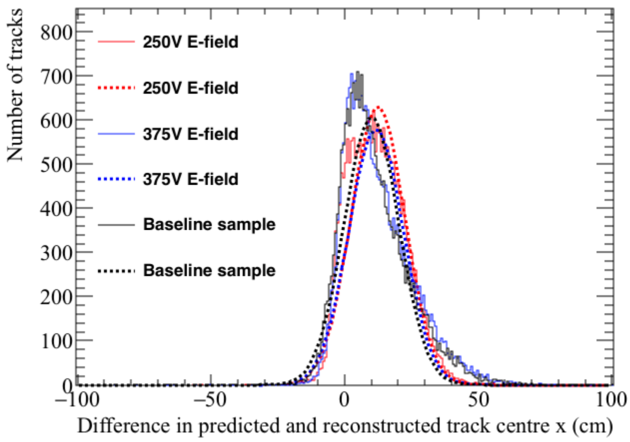

(b) The average difference in the central x position of a track using the hit *RMS* metric.

Fig. 6.31 The accuracy of the hit *RMS* method, for changing values of the electric field.

Figures 6.33 and 6.34 show the accuracy to which the interaction time and central x position of a track can be determined using the effect that diffusion has on the hit *RMS* and hit $RMS/Charge$ for changing values of the longitudinal diffusion constant respectively. As would be expected, both figures show that the accuracy to which the interaction time and

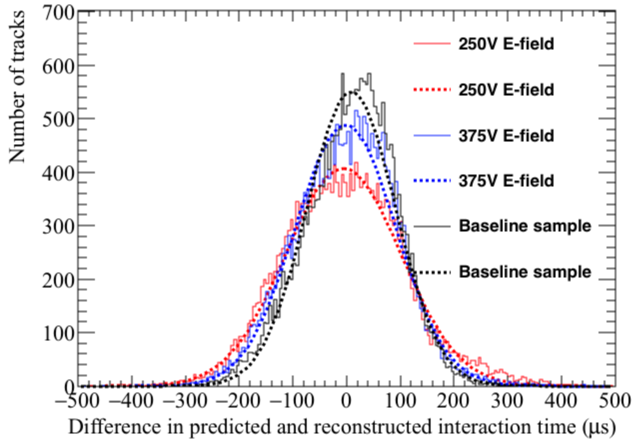

(a) The average difference in interaction times using the hit *RMS*/*Charge* metric.

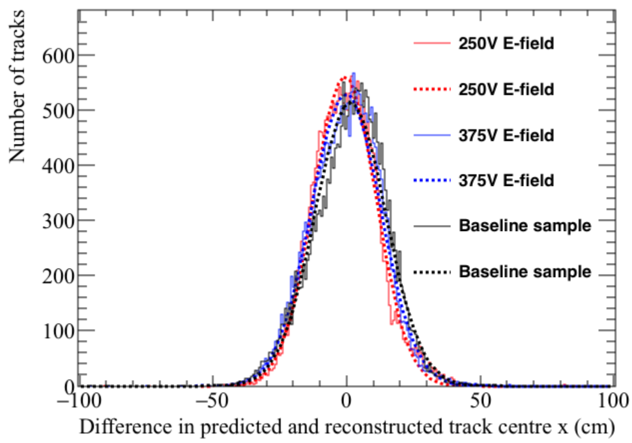

(b) The average difference in the central x position of a track using the hit *RMS*/*Charge* metric.

Fig. 6.32 The accuracy of the hit *RMS*/*Charge* method, for changing values of the electric field.

central x position can be predicted are highly dependant on the longitudinal diffusion constant. It is interesting to note that the extremely poor resolution when there is no longitudinal seen in Figure 6.33 is not present in Figure 6.34. It is thought that this is due to charge attentuation which will still occur due to the finite electron lifetime.

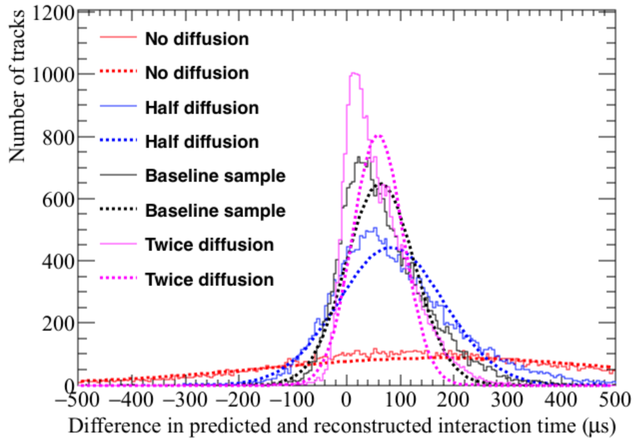

(a) The average difference in interaction times using the hit *RMS* metric.

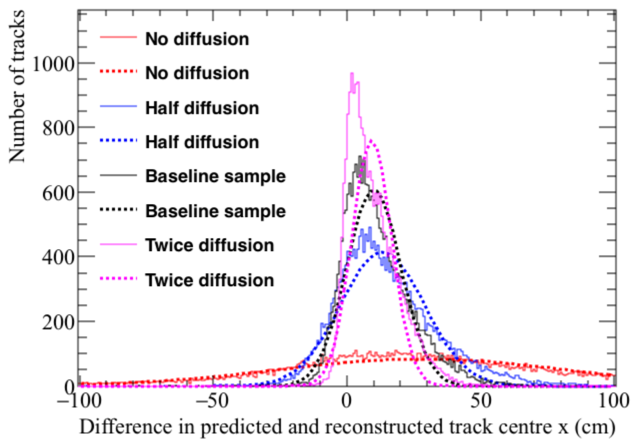

(b) The average difference in the central x position of a track using the hit *RMS* metric.

Fig. 6.33 The accuracy of the hit *RMS* method, for changing values of the constant of longitudinal diffusion.

6.5.4 The limitations of and future improvements to the method of interaction time determination using diffusion

The comparison of the 35 ton data and Monte Carlo samples, as well as the Monte Carlo samples with differeing detector conditions, show that there is potential in the ability to determine interaction times using the effects of diffusion. However, there are still some issues which need to be overcome. These will be discussed briefly below.

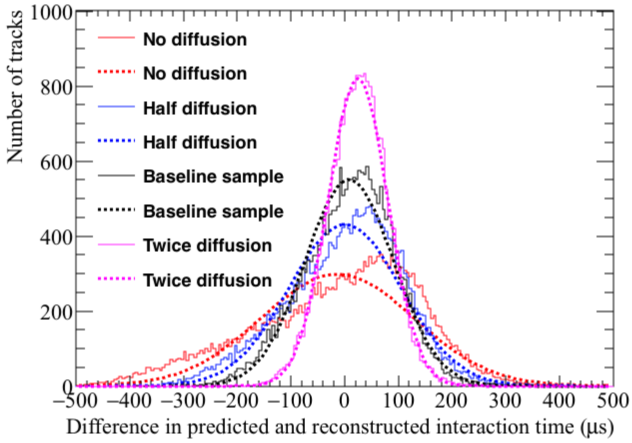

(a) The average difference in interaction times using the hit $RMS/Charge$ metric.

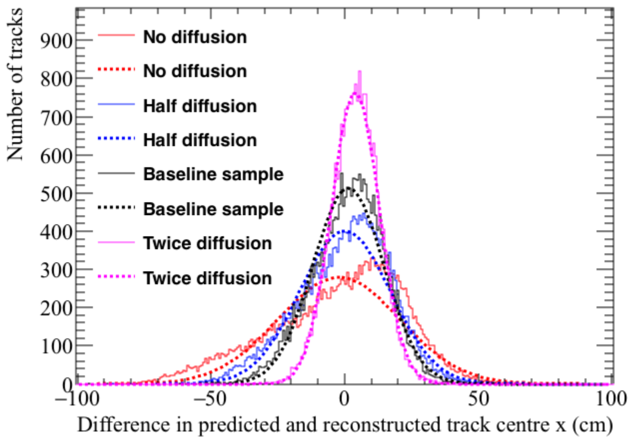

(b) The average difference in the central x position of a track using the hit $RMS/Charge$ metric.

Fig. 6.34 The accuracy of the hit $RMS/Charge$ method, for changing values of the constant of longitudinal diffusion.

All of the figures shown that had the difference in predicted and reconstructed interaction times were not centered around 0 μs and also had large FWHMs. It is thought that this is due to interpreting distributions which are not Gaussian as Gaussian functions, such as Figure 6.22. This means that when the MPVs are calculated using only the values around the peaks, there are large tails at both high and low values which are not counted. As the hits which make up these tails are still used to predict the interaction times they will introduce the observed offsets as the times which they would predict will be far from that which the MPV would predict. The result of this is that the assumption made earlier, that over a large number of hits the average predicted interaction time will be correct, could no longer hold. A potential solution to remedy this, is to refine the selection of hits that are used to predict the interaction time to exclude the extreme values of these tails. However, to do this accurately would require some knowledge of the hit location, as the MPV of hit *RMS* can change significantly over the drift length of the detector. This is shown in Figure 6.23, where the MPV of hit *RMS* in Monte Carlo changes from roughly 1.9 ticks near the APAs to roughly 2.8 ticks 200 cm away from the APAs. Looking at Figure 6.22a, this range encompasses the entire distrbibution of Monte Carlo hit *RMS* values, including the tail of hit *RMS* above 2.3 ticks which we would like to remove. Another solution to improving the accuracy of the predicted interaction time could be to weight the predicted interaction times from each hit in some way which better represents the distribution of hit *RMS* and hit $RMS/Charge$ seen in Figure 6.22.

An important improvement to the method would be to expand it to include the induction plane wires, as this will greatly increase both the number of wires which can be used, and the range of track angles whose interaction times can be predicted. The angular range of the method would increase as, when using only collection plane wires it is impossible to reconstruct enough hits for nearly vertical muons as very few wires would be hit, this was discussed in Section 5.3. This was not attempted here as the electronics noise in the 35 ton data was too large to able to reliably reconstruct all hits on the induction planes without reconstructing many noise hits, and so the hit threshold was very high.

Chapter 7

Simulations of the DUNE Far Detector

Previous work presented has been done concerning the 35 ton prototype, however it is also important to simulate the DUNE Far Detector (FD). Simulations in the FD have concentrated on cosmogenic background to neutrino oscillations, in Section 7.1, and the muon background to nucleon decay, in Section 7.3. The simulations shown in Section 7.1 are discussed in!!!! citepMartinsThesis!!!!, and were performed for the Long Baseline Neutrino Experiment (LBNE) which along with the Long Baseline Neutrino Oscillation (LBNO) experiment formed the basis for DUNE and so are included here for completeness. The other work presented was performed for the DUNE collaboration in conjunction with work done by Vitaly Kudryavtsev and Matthew Robinson, both of the University of Sheffield, and was performed with the aim of producing muon-induced background limits to nucleon decay.

7.1 Simulations of the LBNE surface detector

7.2 The use of MUSUN in LArSoft

The primary muons in the following discussions are all generated using MUSIC [8] [10] [11] and MUSUN [8] [9], and so a brief overview of them is required. MUSIC first propagates muons through a medium defined by the user for given initial energies, positions and direction cosines. A range of energies between 10^2 and 10^7 GeV are considered and their energy distributions are stored at depths of between 100 and 15,000 m w.e. Energy losses due to four processes are considered; ionisation, bremsstrahlung, electron-positron pair production and muon-nucleus inelastic scattering. The output of MUSIC is then used by MUSUN to generate a muon energy spectrum and angular distribution for a given detector location given details about the local surface profile.

The location of the DUNE detector near the Ross shaft at SURF has global coordinates of: latitude = $44^{\circ}|20'45.21''$ N and longitude $103^{\circ}45'16.13''$ West. The rock composition is assumed to be $< Z >$ = 12.09 and $< A >$ = 24.17, and the density is assumed to be 2.70 g cm-3 [39]. The flux calculated by MUSIC/MUSUN of 5.18×10^{-9} cm^{-2} s^{-1} sr^{-1} is well matched to the flux measured by the active veto system of the Davis' experiment which was $(5.38 \pm 0.07) \times 10^{-9}$ cm^{-2} s^{-1} sr^{-1} [40]. Given small differences in these values and another measurement by the Majorana demonstrator, the systematic uncertainty in calculating the muon flux is estimated to be 20% [41].

The surface profile around the proposed detector location is shown in Figure 7.1a, where the proposed location is in the centre of the map. Each quadrant on the map has been divided into 4 angles of 22° to help guide the eye when comparing to Figure 7.1b, where the distribution of azimuth angles is plotted. The vertical lines in Figure 7.1b show the division of the quadrants when the angle is calculated from East. When moving from East to North it is possible to discern how the peaks and troughs on the surface profile correspond to troughs and peaks in the distribution of azimuthal angle.

Given these parameters the muon flux when assuming a spherical detector geometry without simulating a detector cavern is given by Table 7.1.

Table 7.1 Muon flux parameters as calculated with MUSIC/MUSUN.

Total flux (cm^{-2} s^{-1})	Mean E_{μ} (GeV)	Mean slant depth (m w.e)	Mean θ (°)
5.66×10^{-9}	283	4532	26

The muons simulated for DUNE are sampled on a the surface of a box surrounding the detector hall that also encompassed 7 m of rock above the cavern, and 5 m of rock on all other sides. This is to ensure that there is sufficient rock to induce cascades both above and around the detector hall, as it is mainly the secondaries produced in these interactions that enter the detector which are of concern to nucleon decay searches. This will be discussed in Section 7.3. The size of the box the muons are sampled from is $74.43 \times 29.54 \times 30.18$ m^3, compared to the simulated cryostat that has dimensions of $61.62 \times 14.94 \times 13.58$ m^3, where these dimensions are (length $\times$ width $\times$ height). The muons are sampled randomly according to their energy spectrum for a given zenith and azimuthal angle, using the angular

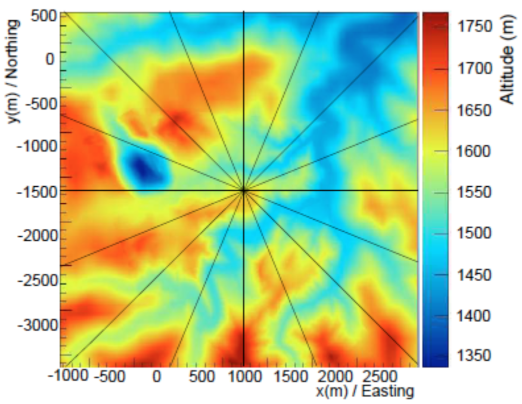

(a) The surface profile of the DUNE far detector site at SURF.

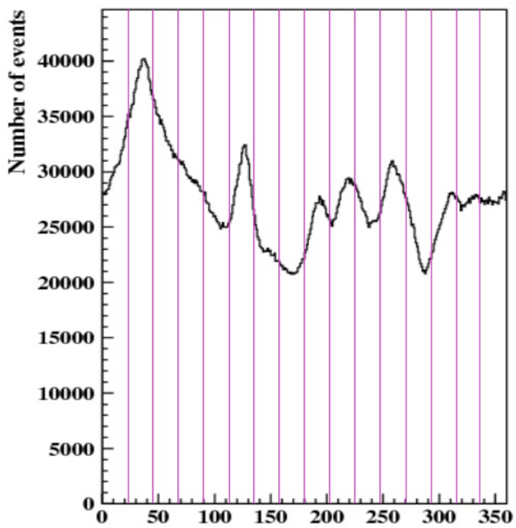

(b) The distribution of azimuthal angles of muons at the DUNE far detector site at SURF.

Fig. 7.1 The correlation between the surface profile and distribution of azimuthal angles at the DUNE far detector site. The quadrants have been divided into four angles of equal size. The azimuthal angle, calculated as the angle from East (pointing to the right in Fig. 7.1a), and increasing counterclockwise, is seen to follow the contours of the surface profile.

distribution obtained with MUSIC.

Before this could be done however, MUSUN had to be incorporated into the DUNE software framework as it has previously been maintained in FORTRAN as an external package. This involved building on the work done by the LZ collaboration in porting the code to C++ !!!!!citepKareem. The process by which this was done was to first reproduce the distributions produced by the LZ collaboration using the DUNE software framework. Once the distributions could be reproduced for the Davis shaft at SURF, the muon distributions produced by the original FORTRAN code for the DUNE detector location were reproduced. The distributions produced by the DUNE software framework are shown in Figure 7.2, these are seen to be consistent with the same distributions shown in [42]. The initial positions of 10,000 muons generated in LArSoft around the DUNE 10 kt module that is simulated is shown in Figure 7.3. The initial positions of the muons are shown as blue points, whilst the cryostat is a single black box and each TPC is a single red box.

It is found that the muon rate through the box upon which the muons are sampled is 0.1579 Hz, this rate is later used to normalise the background event rate in Section 7.3. Of the muons that are sampled, roughly a third pass through the active volume, to give a muon

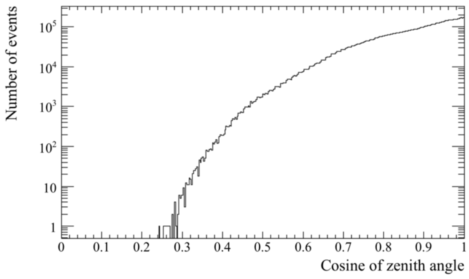

(a) Distribution of zenith angles.

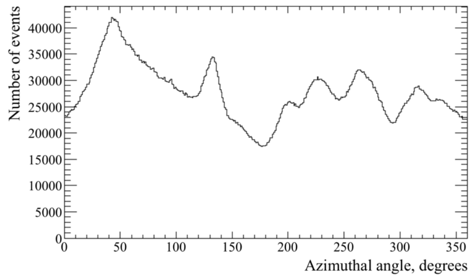

(b) Distribution of azimuthal angles.

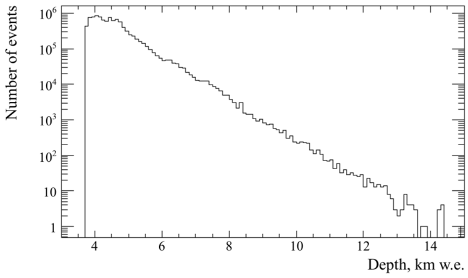

(c) Distribution of slant depths.

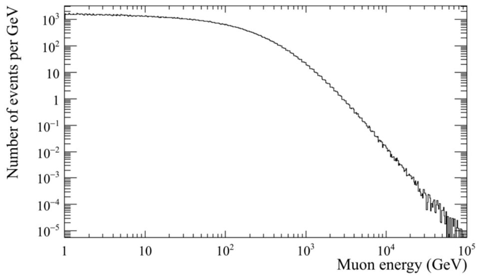

(d) The energy spectrum of muon energies.

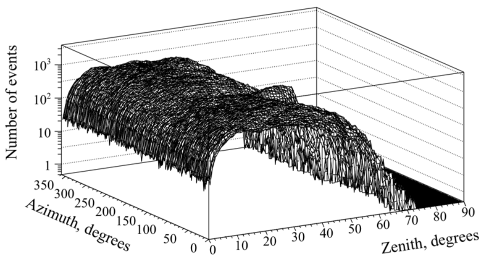

(e) The distribution of zenith and azimuthal angles.

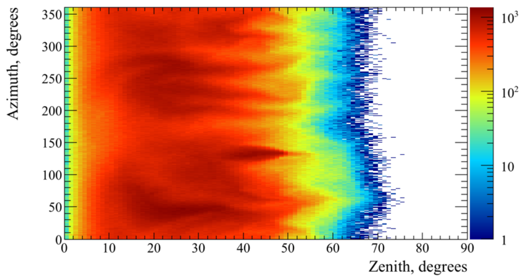

(f) The distribution of zenith and azimuthal angles, shown with a colour z scale.

Fig. 7.2 The distributions of some of the important quantities for muons generated by MUSUN in LArSoft.

rate through the active volume of 0.053 Hz.

7.3 Nucleon decay channels in DUNE

When searching for rare processes where an experiment is unlikely to see more than a few real signatures, an exhaustive study of the potential backgrounds is required so as to establish that if a signal is observed, it could provide overwhelming evidence for the process. The search for nucleon decay in DUNE is one such process, and so an exhaustive study of the

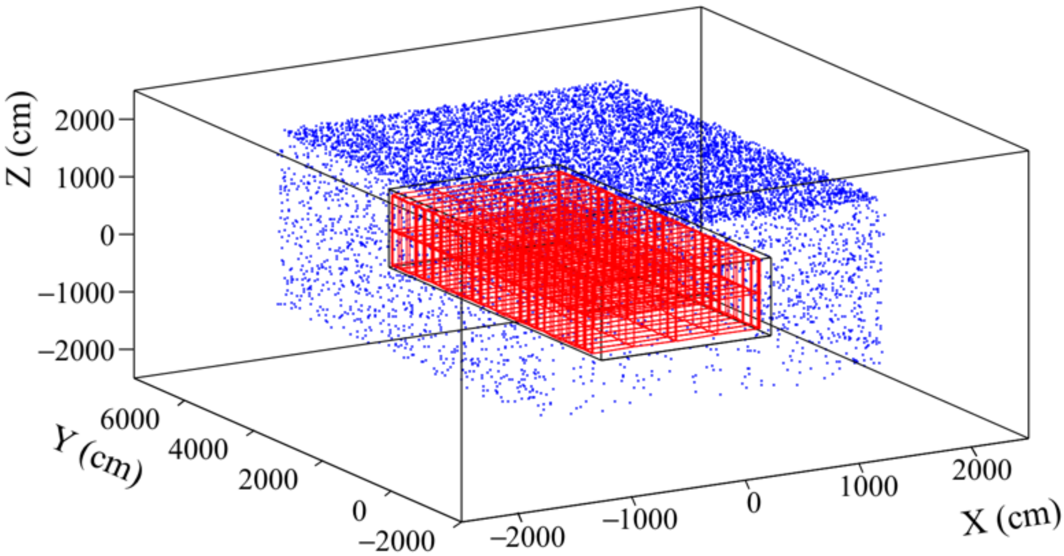

Fig. 7.3 The initial positions of muons generated by MUSUN around a DUNE 10 kt module. The initial positions of the muons are shown as blue points, whilst the cryostat is a single black box and each TPC is a single red box.

background to nucleon decay is required. As discussed in Section 3.3.3 cosmogenic muons cause background to nucleon decay signatures by creating secondary particles which are able to mimic the nucleon decay signatures. For this reason it is necessary to simulate this background, and to develop a series of cuts that can be applied to the cosmogenic background to establish that the energy depositions which they cause, are not due to nucleon decays. When doing this it is important to use a simulation that is as accurate as possible to the DUNE far detector. It is for this reason that the MUSUN was incorporated into LArSoft, as the muons which it generates are well matched to the observed muon flux, as described in Section 7.2.

To ensure that the background has been properly simulated it is advantageous to simulate many more background events than will be collected by the experiment. As the DUNE detector will run for roughly 20 years, it was decided that an initial sample representing 200 years of detector live time would be simulated. Given that the muon rate through the cavern is 0.1579 Hz, 200 years of detector live time corresponds to roughly 10^9 muons. This only represents one of the DUNE 10 kt modules, and so an even larger dataset will be required to represent the full live time of the 4 10 kt modules. For this reason, muons will continue to be generated even though the initial sample size has been reached.

Producing samples of this size requires significant computer power, both in terms of running time, and storage space. As such, many of the simulated events are discarded before being saved to disk, through the application of a filter after GEANT4. It is essential that the events which are discarded could not have been mistaken for signal events, and so only very generous cuts are applied. Only events satisfying one of the following cuts are discarded;

- Contain a muon track of more than 1 m.
- There are no energy depositions in the entire detector volume.

It is envisioned that a muon track of more than a metre would not be misreconstructed. It is also assumed that any signatures observed within one drift window of such a track would not be studied in a nucleon decay search, as there would be doubt as to the authenticity of the signal. Given that the total rate of muons through the active volume is 0.053 Hz, and that the drift time is a few ms, ignoring all times where any track from a cosmogenic muon is present results in less than 0.1% dead time. The dead time associated with ignoring events with muon tracks of more than 1 m is clearly less than this. This amount of dead time is assumed to be acceptable.

After applying this series of cuts, the initial sample of 10^9 muons is reduced to XXXX$\times 10^{XXXX}$ muons which is a much more reasonable sample size to store on tape, and to perform analyses on. It is upon this reduced sample of muons that the cosmogenic background analyses are performed. As discussed in Section 3.3.2, the proton decay channel of $p \rightarrow K^+ + \nu^e$ is referred to as the 'Golden Channel' in LAr, this analysis is discussed in [41]. The related decay of channel of $n \rightarrow K^+ + e^-$ is discussed here.

7.3.1 Cosmogenic background to the $n \rightarrow K^+ + e^-$ decay channel

As shown in Table 3.1, the predicted sensitivity that DUNE will have to this channel is much larger than that of Super-K and so it is an interesting decay mode to study as DUNE could easily have the best limit for this decay channel. As discussed in Section 3.3.3, the cosmogenic background to nucleon decay is predominantly caused by neutral particles such as K^0 entering the detector volume and interacting far away from the detector edges. This is particularly true for the 'Golden Channel,' as shown in Figure **??**, but it also holds for other channels. This means that it is events such as this which are the main cause for concern when trying to eliminate all cosmogenic backgrounds.

As is the case with the 'Golden Channel,' the final state of the decay contains a single charged Kaon and so energy constraints can be applied to the Kaon that is produced. However, there is also a single electron in the final state, and so this provides further constraints upon the final state. This extra constraint should make it more difficult for a background event to mimic a signal event, as one would expect that in a signal event the charged Kaon and electron would have a common vertex. This is discussed in Section 7.3.2. Other constraints that are applied to eliminate background events are; a cut on muon length, a cut on depositions near the detector edges, and a cut on the energy deposited in the detector that is not due to either the Kaon or electron. These cuts, which are applied sequentially, are outlined below:

- The event contains energy depositions due to Kaons and due to electrons.
- The event contains at least one Kaon track, and at least one electron track.
- The event contains a single Kaon track, and a single electron track.
- No muon travels more than 20 cm in the detector volume.
- The event has no energy depositions within 2 cm of the detector edges.
- The Kaon and electron share a common vertex.
- The energy depositions are within the range which are expected from a nucleon decay event.

A discussion on the expected energy ranges for the Kaon, electron, and other energy depositions are contained in Section 7.3.2, where they are determined using a study of simulated signal events.

7.3.2 Signal events in the $n \to K^{+} + e^{-}$ decay channel

7.3.3 Future improvements to nucleon decay studies

Thus far the nucleon decay studies have been performed on the Monte Carlo truth information, and so have not used reconstructed objects such as tracks. The extension of the analyses to include work on tracks is an important next step as then the full analysis which would be applied on real data can be tested. Preliminary studies have begun on hit reconstruction, and involve running a filter on the muons used in the earlier analyses. This is because the number of events which are saved to disk would be prohibitive to running the full reconstruction process. As such, only events which meet the following criteria will be reconstructed!!! citepProbsCollabMeetingPres!!!;

- A minimum of 10 MeV deposited in the detector volume.
- A maximum of 3,000 MeV deposited in the detector volume.
- A maximum of 5 MeV deposited within 10 cm of the detector edge.

These criteria are designed to be broad enough that the full range of nucleon decay modes can be studied, including di-nucleon decay modes, hence the maximum deposited energy greatly exceeding the rest mass of a single nucleon.

References

[1] E. D. Church, "LArSoft: A Software Package for Liquid Argon Time Projection Drift Chambers," 2013.

[2] "Larsoft," 2017. [online] http://larsoft.org.

[3] R. Brun and F. Rademakers, "ROOT: An object oriented data analysis framework," *Nucl. Instrum. Meth.*, vol. A389, pp. 81–86, 1997.

[4] S. Agostinelli *et al.*, "Geant4—a simulation toolkit," *Nuclear Instruments and Methods in Physics Research Section A: Accelerators, Spectrometers, Detectors and Associated Equipment*, vol. 506, no. 3, pp. 250 – 303, 2003.

[5] C. Andreopoulos *et al.*, "The {GENIE} neutrino monte carlo generator," *Nuclear Instruments and Methods in Physics Research Section A: Accelerators, Spectrometers, Detectors and Associated Equipment*, vol. 614, no. 1, pp. 87 – 104, 2010.

[6] D. Casper, "The Nuance neutrino physics simulation, and the future," *Nucl. Phys. Proc. Suppl.*, vol. 112, pp. 161–170, 2002. [,161(2002)].

[7] "Cosmic-ray shower library {CRY}," 2012. [online] http://nuclear.llnl.gov/simulation/doc_cry_v1.7/cry.pdf.

[8] V. Kudryavtsev, "Muon simulation codes {MUSIC} and {MUSUN} for underground physics," *Computer Physics Communications*, vol. 180, no. 3, pp. 339 – 346, 2009.

[9] V. A. Kudryavtsev, N. J. C. Spooner, and J. E. McMillan, "Simulations of muon induced neutron flux at large depths underground," *Nucl. Instrum. Meth.*, vol. A505, pp. 688–698, 2003.

[10] P. Antonioli, C. Ghetti, E. V. Korolkova, V. A. Kudryavtsev, and G. Sartorelli, "A Three-dimensional code for muon propagation through the rock: Music," *Astropart. Phys.*, vol. 7, pp. 357–368, 1997.

[11] V. A. Kudryavtsev, E. V. Korolkova, and N. J. C. Spooner, "Narrow muon bundles from muon pair production in rock," *Phys. Lett.*, vol. B471, pp. 251–256, 1999.

[12] "The current status of simulation and reconstruction for the dune far detector," 2016. [online] http://docs.dunescience.org:8080/cgi-bin/ShowDocument?docid=1689.

[13] C. Harris and M. Stephens, "A combined corner and edge detector.," Citeseer, 1988.

[14] P. V. C. Hough, "Machine Analysis Of Bubble Chamber Pictures," in *Proceedings, 2nd International Conference on High-Energy Accelerators and Instrumentation, HEACC 1959: CERN, Geneva, Switzerland, September 14-19, 1959*, vol. C590914, pp. 554–558, 1959.

[15] M. Antonello *et al.*, "Precise 3D track reconstruction algorithm for the ICARUS T600 liquid argon time projection chamber detector," *Adv. High Energy Phys.*, vol. 2013, p. 260820, 2013.

[16] J. S. Marshall and M. A. Thomson, "The Pandora Software Development Kit for Pattern Recognition," *Eur. Phys. J.*, vol. C75, no. 9, p. 439, 2015.

[17] "Emshower reconstruction," 2016. [online] http://docs.dunescience.org:8080/cgi-bin/ShowDocument?docid=1369.

[18] J. Birks, "The efficiency of organic scintillatois," *ORGANIC*, p. 12, 1960.

[19] R. Acciarri *et al.*, "A study of electron recombination using highly ionizing particles in the ArgoNeuT Liquid Argon TPC," *JINST*, vol. 8, p. P08005, 2013.

[20] J. Thomas and D. A. Imel, "Recombination of electron-ion pairs in liquid argon and liquid xenon," *Phys. Rev. A*, vol. 36, pp. 614–616, Jul 1987.

[21] H. Bethe, "Zur theorie des durchgangs schneller korpuskularstrahlen durch materie," *Annalen der Physik*, vol. 397, no. 3, pp. 325–400, 1930.

[22] F. Bloch, "Zur bremsung rasch bewegter teilchen beim durchgang durch materie," *Annalen der Physik*, vol. 408, no. 3, pp. 285–320, 1933.

[23] C. Patrignani *et al.*, "Review of Particle Physics," *Chin. Phys.*, vol. C40, no. 10, p. 100001, 2016.

[24] "Module to unstick adc codes," 2016. [online] https://indico.fnal.gov/getFile.py/access?contribId=2&resId=0&materialId=slides&confId=11627.

[25] "Noise characterization and filtering in the microboone tpc," 2016. [online] http://www-microboone.fnal.gov/publications/publicnotes/MICROBOONE-NOTE-1016-PUB.pdf.

[26] J. Cooley and J. Turkey, "An algorithm for the machine calculation of complex fourier series," *Math. Comp.*, vol. 19, pp. 297–301, 1965.

[27] N. Wiener, *Extrapolation, Interpolation, and Smoothing of Stationary Time Series*. [Cambridge]: Technology Press of the Massachusetts Institute of Technology., 1942.

[28] "35t observations and measurements," 2016. [online] http://docs.dunescience.org:8080/cgi-bin/ShowDocument?docid=1704.

[29] "35t noise studies summary - apa wire readout noise," 2016. [online] http://docs.dunescience.org:8080/cgi-bin/ShowDocument.

[30] "Update on reconstruction of 35t data," 2016. [online] https://indico.fnal.gov/getFile.py/access?contribId=1&resId=0&materialId=slides&confId=12349.

[31] P. Torr and A. Zisserman, “Mlesac: A new robust estimator with application to estimating image geometry,” *Computer Vision and Image Understanding*, vol. 78, no. 1, pp. 138–156, 2000.

[32] “Something,” 2016. [online] /urlSOMETHING.

[33] C. Anderson *et al.*, “The ArgoNeuT Detector in the NuMI Low-Energy beam line at Fermilab,” *JINST*, vol. 7, p. P10019, 2012.

[34] “Update on 35 ton analysis,” 2016. [online] https://indico.fnal.gov/getFile.py/access?contribId=1&resId=0&materialId=slides&confId=12396.

[35] V. M. Atrazhev and I. V. Timoshkin, “Trasport of electrons in atomic liquids in high electric fields,” *IEEE Trans. Dielectrics and Electrical Insulation*, vol. 5, pp. 450–457, 1998.

[36] Y. Li *et al.*, “Measurement of Longitudinal Electron Diffusion in Liquid Argon,” *Nucl. Instrum. Meth.*, vol. A816, pp. 160–170, 2016.

[37] “Looking at electron diffusion in 35t data and mc,” 2016. [online] https://indico.fnal.gov/getFile.py/access?contribId=43&sessionId=19&resId=0&materialId=slides&confId=10613.

[38] C. Bromberg *et al.*, “Design and operation of longbo: a 2 m long drift liquid argon tpc,” *Journal of Instrumentation*, vol. 10, no. 07, p. P07015, 2015.

[39] D. M. Mei, C. Zhang, K. Thomas, and F. Gray, “Early Results on Radioactive Background Characterization for Sanford Laboratory and DUSEL Experiments,” *Astropart. Phys.*, vol. 34, pp. 33–39, 2010.

[40] M. L. Cherry, M. Deakyne, K. Lande, C. K. Lee, R. I. Steinberg, B. Cleveland, and E. J. Fenyves, “Multiple muons in the homestake underground detector,” *Phys. Rev. D*, vol. 27, pp. 1444–1447, Apr 1983.

[41] “September 2016 progress report from the atmospheric neutrinos, nucleon decay, and cosmogenics working groups,” 2016. [online] http://docs.dunescience.org:8080/cgi-bin/ShowDocument?docid=1644.

[42] “Muon simulations for lbne using music and musun,” 2014. [online] http://lbne2-docdb.fnal.gov/cgi-bin/ShowDocument?docid=9673.

Appendix A

Supporting figures to Monte Carlo studies concerning determining interaction times using the effects of diffusion

Figure A.1, shows how the most probable values of the hit RMS and hit $RMS/Charge$ change as the electronics noise increases, for hits between 20 and 30 cm from the APAs. Figure A.2, shows how the most probable values of hit RMS changes as drift distance increases for track associated with counter differences of 4, for different values of the electronics noise. Figure A.3, shows how the most probable value of hit RMS next to the APAs changes for increasing counter differece.

Figure A.4, shows how the most probable values of the hit RMS and hit $RMS/Charge$ change as the electron lifetime increases, for hits between 20 and 30 cm from the APAs. Figure A.5, shows how the most probable values of hit RMS changes as drift distance increases for track associated with counter differences of 4, for different values of the electron lifetime. Figure A.6, shows how the most probable value of hit RMS next to the APAs changes for increasing counter differece.

Figure A.7, shows how the most probable values of the hit RMS and hit $RMS/Charge$ change as the electric field increases, for hits between 20 and 30 cm from the APAs. Figure A.8, shows how the most probable values of hit RMS changes as drift distance increases for track associated with counter differences of 4, for different values of the electric field.

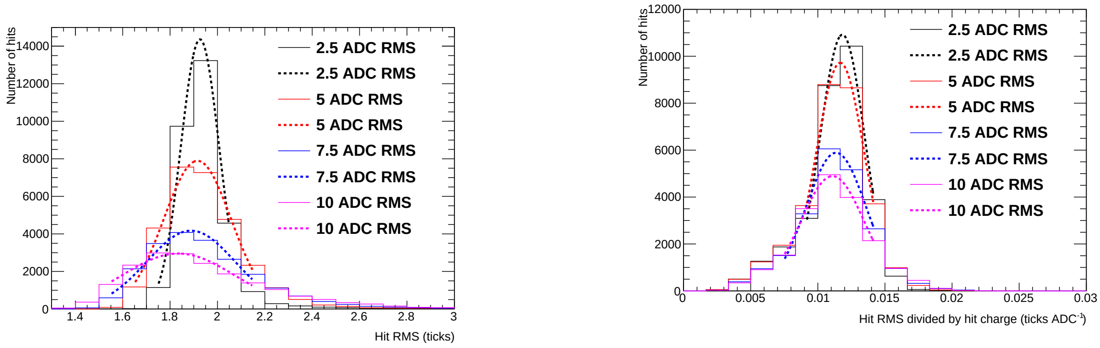

(a) The most probable hit RMS values for hits between $x = 20$ cm and $x = 30$ cm.

(b) The most probably hit $RMS/Charge$ values for hits between $x = 20$ cm and $x = 30$ cm.

Fig. A.1 The most probable values of the hit RMS and hit $RMS/Charge$ distributions for hits between $x = 20$ cm and $x = 30$ cm, for tracks with a counter difference of 4, as the electronics noise changes.

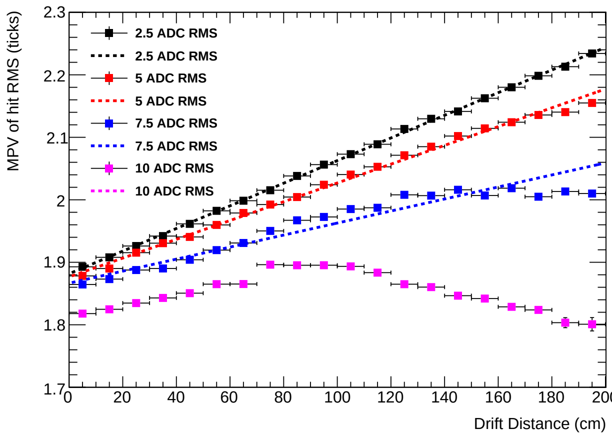

Fig. A.2 The most probable values of hit RMS as a function of drift distance, for tracks associated with a coincidence that had a counter difference of 4, as the electronics noise changes.

Figure A.9, shows how the most probable value of hit RMS next to the APAs changes for increasing counter differece.

Figure A.10, shows how the most probable values of the hit RMS and hit $RMS/Charge$ change as the constant of longitudinal diffusion increases, for hits between 20 and 30 cm from the APAs. Figure A.11, shows how the most probable values of hit RMS changes as drift distance increases for track associated with counter differences of 4, for different values of the constant of longitudinal diffusion. Figure A.12, shows how the most probable value of

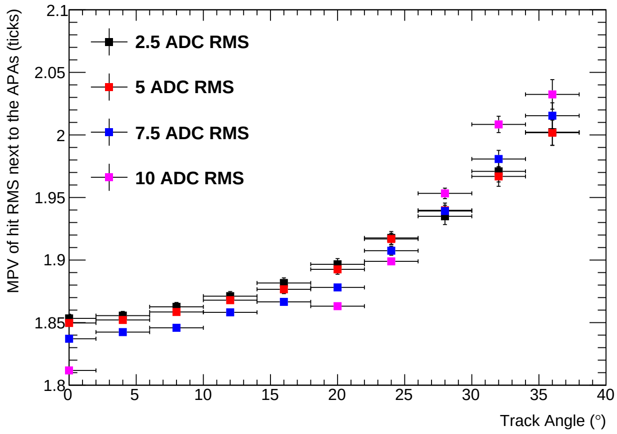

Fig. A.3 The most probable values of hit RMS within 10 cm of the APAs, as a function of the counter difference of the coincidence, that the track was associated with, as the electronics noise changes.

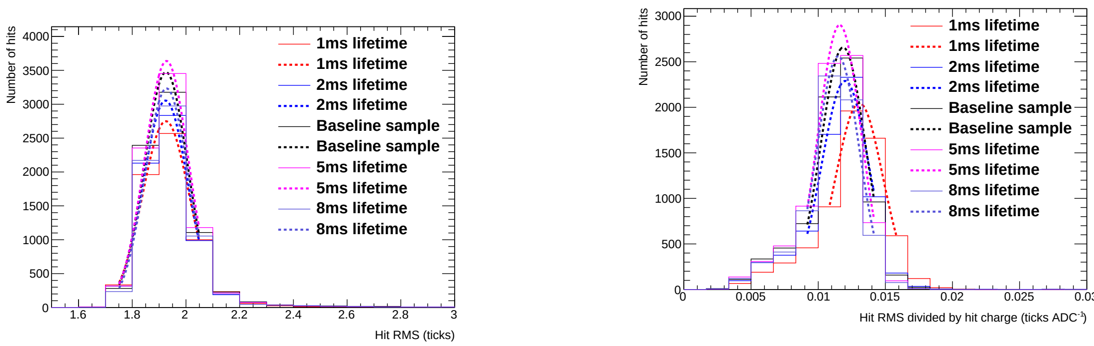

(a) The most probable hit RMS values for hits between $x = 20$ cm and $x = 30$ cm.

(b) The most probably hit $RMS/Charge$ values for hits between $x = 20$ cm and $x = 30$ cm.

Fig. A.4 The most probable values of the hit RMS and hit $RMS/Charge$ distributions for hits between $x = 20$ cm and $x = 30$ cm, for tracks with a counter difference of 4, as the electron lifetime changes.

hit RMS next to the APAs changes for increasing counter differece.

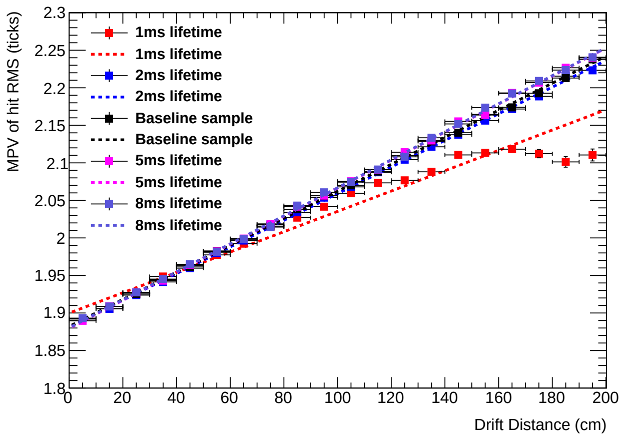

Fig. A.5 The most probable values of hit *RMS* as a function of drift distance, for tracks associated with a coincidence that had a counter difference of 4, as the electron lifetime changes.

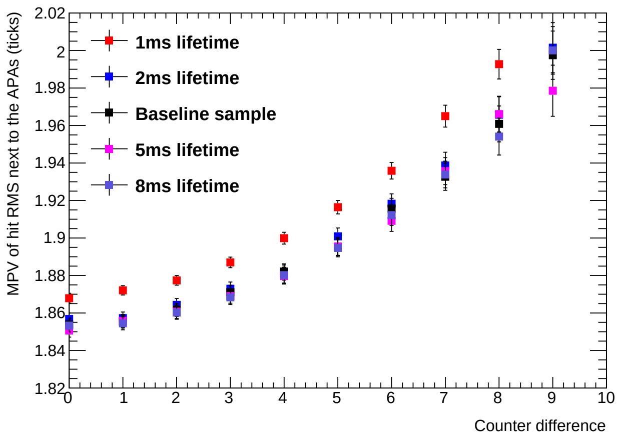

Fig. A.6 The most probable values of hit *RMS* within 10 cm of the APAs, as a function of the counter difference of the coincidence, that the track was associated with, as the electron lifetime changes.

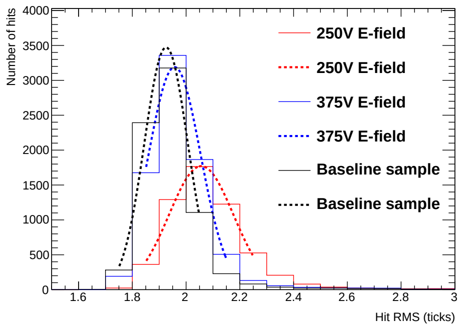

(a) The most probable hit *RMS* values for hits between $x = 20$ cm and $x = 30$ cm.

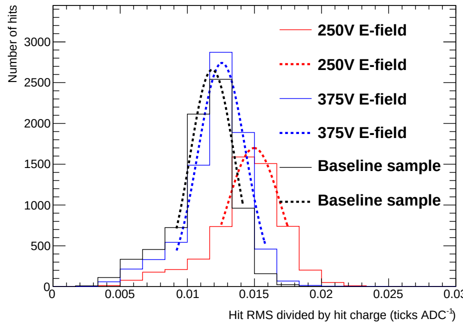

(b) The most probably hit $RMS/Charge$ values for hits between $x = 20$ cm and $x = 30$ cm.

Fig. A.7 The most probable values of the hit *RMS* and hit $RMS/Charge$ distributions for hits between $x = 20$ cm and $x = 30$ cm, for tracks with a counter difference of 4, as the electric field changes.

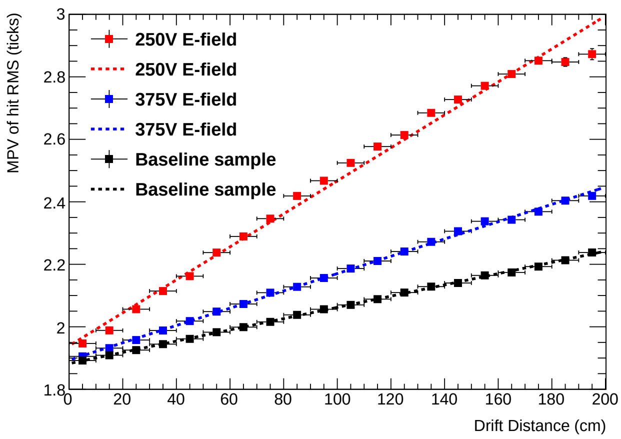

Fig. A.8 The most probable values of hit *RMS* as a function of drift distance, for tracks associated with a coincidence that had a counter difference of 4, as the electric field changes.

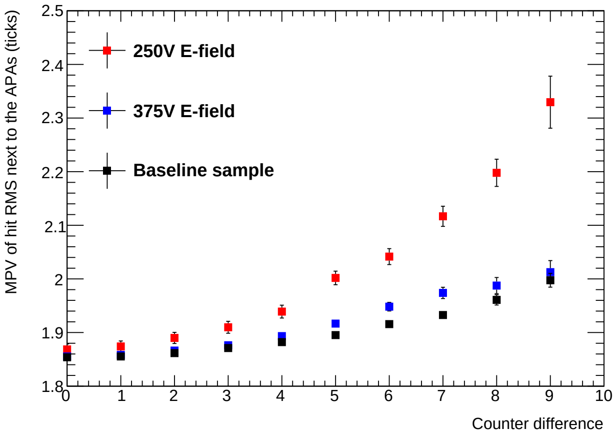

Fig. A.9 The most probable values of hit *RMS* within 10 cm of the APAs, as a function of the counter difference of the coincidence, that the track was associated with, as the electric field changes.

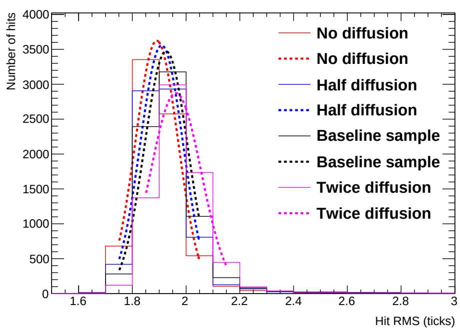

(a) The most probable hit *RMS* values for hits between $x = 20$ cm and $x = 30$ cm.

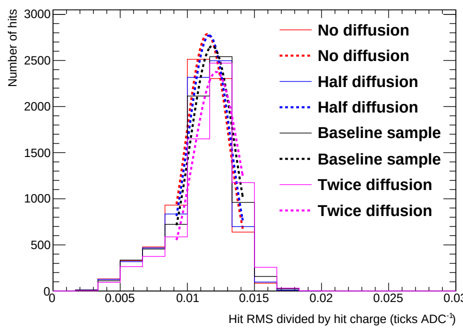

(b) The most probably hit $RMS/Charge$ values for hits between $x = 20$ cm and $x = 30$ cm.

Fig. A.10 The most probable values of the hit *RMS* and hit $RMS/Charge$ distributions for hits between $x = 20$ cm and $x = 30$ cm, for tracks with a counter difference of 4, as the constant of longitudinal diffusion changes.

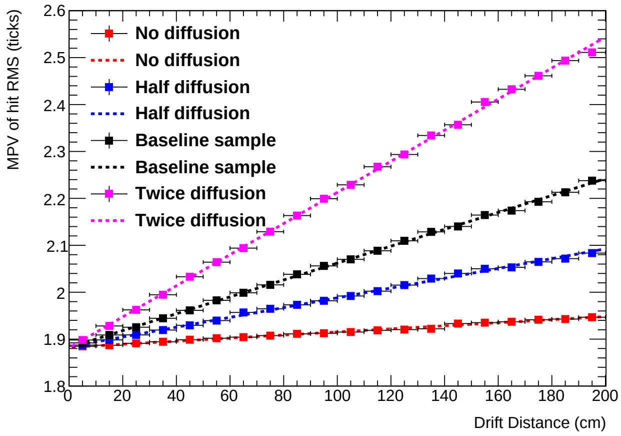

Fig. A.11 The most probable values of hit *RMS* as a function of drift distance, for tracks associated with a coincidence that had a counter difference of 4, as the constant of longitudinal diffusion changes.

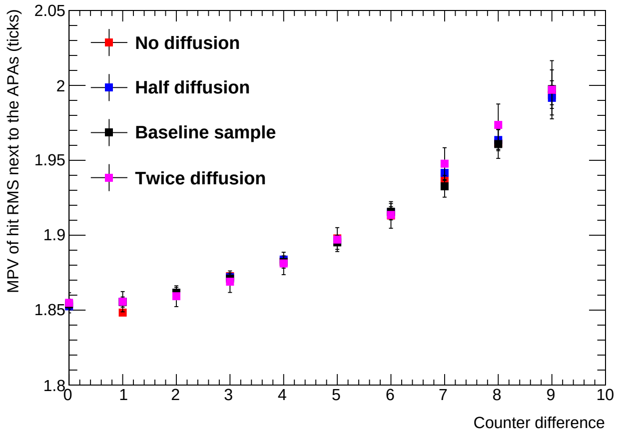

Fig. A.12 The most probable values of hit *RMS* within 10 cm of the APAs, as a function of the counter difference of the coincidence, that the track was associated with, as the constant of longitudinal diffusion changes.

Appendix B

Something else mildly interesting